# The Design of Perovskites for Light-Emitting Applications

by

Petar Todorović

A thesis submitted in conformity with the requirements
for the degree of Doctor of Philosophy

The Edward S. Rogers Sr. Department of Electrical & Computer Engineering
University of Toronto

© Copyright by Petar Todorović 2021

# The Design of Perovskites for Light-Emitting Applications

Petar Todorović

Doctor of Philosophy

The Edward S. Rogers Sr. Department of Electrical & Computer Engineering
University of Toronto

2021

## Abstract

In the last decade, perovskite quantum dots have emerged as next-generation active materials for optoelectronics. They have tunable bandgaps, good charge carrier mobility and low defect density, and are readily synthesized. They exhibit high photoluminescence quantum yields and bandgaps tuned throughout the visible range via compositional engineering and nanostructure modulation. This positions perovskites for applications in red, green and blue light-emitting diodes. They must achieve narrow emission linewidths, as well as increased stability and efficiencies under operating conditions, to realize their potential in displays.

In this thesis, I explore the design and prediction of novel perovskite materials through experimental and computational methods; and I find new optoelectronic materials with promise as narrowband light-emitters.

Mixed anion approaches used by prior researchers to tune bandgap suffer from halide segregation and resultant spectral instability. I designed a mixed *cation* strategy whereby $Rb^+$ is directly incorporated during synthesis into $CsPbBr_3$ nanocrystals, forming the alloyed $Rb_xCs_{1-x}PbBr_3$. This resulted in tunable blue-emitting perovskite quantum dots and devices with stable photoluminescence and electroluminescence ranging from 460 – 500 nm and narrow emission linewidths (< 25 nm).

I then investigated how a materials processing strategy involving dynamic post-synthesis organic phosphoryl treatment enables precise control of the distribution of nanostructured morphologies. I found that devices fabricated using the treatment exhibited improved spectral stabilities during operation, as well as record high efficiencies in blue.

Finally, I investigate the application of machine learning to accelerate materials discovery, focusing in particular on ternary perovskite systems. I design deep neural network models that predict the bandgap accurately, and then use these for a rapid materials search aided by an evolutionary algorithm. Through feature analysis, I develop interpretable design rules from the resulting candidates, finding these to be predictive of the structural and optical properties. This enables the experimental realization of a set of novel perovskite UV-semiconductors with narrow emission linewidths and small Stokes shift.

# Acknowledgments

Herein, I present a thesis that was the result of many years of research, none of which would have been brought to completion without the essential collaborations, discussions, and relationships I built throughout. A famous quote summarizes my journey and I owe much to all those who shared their time with me during my doctoral studies, for you have all been a giant at one point in time:

***If I have seen further than others, it is by standing on the shoulders of giants.***
***– Sir Isaac Newton***

First and foremost, I would like to thank my advisor, Professor Edward H. Sargent for his utmost care, guidance, passion, mentorship, and ability to join a truly world-class research group. Ted, your support is unparalleled and I am forever grateful for the opportunity to engage in advancing materials research in the areas of photonics and optoelectronics. Your ability to solve complex problems through an interdisciplinary nature and your time-management skills have had a direct influence on me and have allowed me to grow professionally and academically. Your everlasting support and trust, have let me explore my passions in finance through internships and conferences, which I truly appreciate and thank you for.

Professor Vladimir Bulović, it was your invited research talk at the Xerox Research Centre of Canada which fueled and ignited my passion for research and my pursuit towards a graduate degree. It was your vision and exuberant enthusiasm about nanotechnology and its implications that led me to foresee and want to join academia to advance materials development with the hopes of revolutionizing the world in the area of optoelectronics.

I would also like to acknowledge all of the Sargent group staff members and administrators who have helped me over the years: Jeannie, Stacy, Jennifer, Ana, Damir, Remi, Leny, and Larissa – thank you. I thank the group leaders and senior members who helped shape many of the projects and exposed me to the industrial-research collaborations and think of research through a practical lens: Sjoerd, Zhenyu, and Oleksandr.

Through the last 4 years, I have had the pleasure and opportunity to work with the brightest, creative minds and have developed friendships that I will remember eternally. Thank you to James and Olivier (whom I met at graduate research days), Andrew K., Marc L., Mingyang, Grant, Andrew P., Andrew J., Kris, Marghe, Kishore, Hitarth, Misha, Dongxin, Surath, and everyone else in the Sargent group. In addition, I would like to thank all of the federal and university-wide research grants and awards that I have had the privilege to receive and have helped support me financially (Natural Sciences and Research Council of Canada – PGS, Ontario Graduate Scholarship, and the Ted Rogers Graduate Scholarship).

I will forever be indebted to my best friends Milan Tepić and Bryan Yates who have been there for me through every trial and tribulation; your words, compassion, and advice will never be forgotten. I can only hope that one day our paths cross professionally and that our aspirations come to fruition. Marko Agatonović, Tseno Tselkov, Tong Zhan, and Shamsudeen Mustafa – thank you for all of our conversations and discussions, they have truly shaped my view of life and your mentorship has profoundly generated a positive impact.

Finally, I would like to thank my family to whom I dedicate this thesis. They have sacrificed far more than one can imagine. We arrived from a war-torn country, and my parents devoted their life to fostering better opportunities for my sister and I. Their never-ending love and support have motivated me to pursue my passions and aspirations. Zahvaljujem vam se za sve, vi ste izuzetno moj ponos i verovali ste da cu moci postici sve samo da “zagrejem stolicu” i da radim. Nadam se da ste ponosni na vaseg sina, vi ste mi ceo svet. Od srca vas ljubim i volim.

To all, you are giants in my eyes and although the future is nearly impossible to predict outside the scope of the physical fundamental laws governing the world – I can only wish success and hope that our paths will cross yet again.

# Contributions and Collaborations

Certain text and figures presented herein have been adapted from previously published literature, in articles or in books with approval from the authors and permissions granted by the corresponding organizations. In these instances, appropriate references were included as indicated by journal convention. Permissions are listed in **Appendix C: Copyright and Permissions**. I only included materials from publications on which I was first or co-first author (unless stated otherwise). At the beginning of each chapter, I describe explicitly the collaboration and roles of the authors which contributed to the work.

In this thesis, I use the word "I" when I independently carried out the specific measurements, experimental characterization, writing, analysis, modeling. I use the convention "we" when research work was completed jointly with at least one colleague. When the underlying work was carried out chiefly by a colleague (some examples herein include DFT modelling and certain experimental measurements), I use the passive voice: DFT calculations were performed, TEM measurements were carried out.

# Table of Contents

# List of Tables

# List of Figures

# List of Acronyms

| | |
|---|---|
| CIE | Commission Internationale de l'Eclairage |
| CQD | colloidal quantum dot |
| DNN | deep neural network |
| DFT | Density Functional Theory |
| DOS | density of states |
| DPPOCl | diphenylphosphinic chloride |
| EA | electron affinity |
| EDS/EDX | energy dispersive x-ray spectroscopy |
| EL | electroluminescence |
| EN | electronegativity |
| EQE | external quantum efficiency |
| ETL | electron transport layer |
| FWHM | full-width at half-maximum |
| GNN | graph neural networks |
| GCNN | graph convolutional neural network |
| HSE | Heyd–Scuseria–Ernzerhof exchange-correlation functional |
| HTL | hole transport layer |
| IE | ionization energy |
| ITO | indium tin oxide |
| LCD | liquid crystal display |
| LED | light-emitting diode |
| MA | methylammonium |
| OA | oleic acid |
| OEDW | optimal electronegativity difference window |
| OLA | oleylamine |
| OLED | organic light-emitting diode |
| MAE | mean absolute error |
| MHP | metal halide perovskites |
| ML | machine learning |
| PCE | power conversion efficiency |

| | |
|---|---|
| PCOCl | benzoyl chloride |
| $PPOCl_2$ | phenylphosphonic dichloride |
| $PSO_2Cl$ | benzenesulfonyl chloride |
| PEA | phenylethyl ammonium |
| PeLED | perovskite quantum dot light-emitting diode |
| PQD | perovskite quantum dot |
| PL | photoluminescence |
| PLQY | photoluminescence quantum yield |
| QD | quantum dot |
| QLED | quantum dot light-emitting diode |
| QW | quantum well |
| SAED | selected area electron diffraction |
| SEM | scanning electron microscopy |
| TA | transient absorption |
| TCO | transparent conductive oxide |
| TEM | transmission electron microscopy |
| UPS | ultraviolet photoelectron spectroscopy |
| XPS | x-ray photoelectron spectroscopy |
| XRD | x-ray diffraction |

# List of Appendices

# 1 Introduction

Global energy demand is projected to increase by an overall 24% from 2019 to 2040, largely driven by population growth and economic development.[1] Lighting comprises roughly 15% of global electricity consumption, resulting in 5% of global greenhouse gas emissions in light of the average carbon footprint associated with electricity generation.[2] The lighting component of energy consumption will only increase as countries develop.

As affluence and consumption grow, it is imperative to meet expanding energy demand with cleaner energy sources. Energy efficient and low-cost light-emitting materials can contribute to meeting growing demand for lighting but at lower energy-growth cost.

Conventional lighting technologies comprising incandescent and compact fluorescent lamps exhibit limited luminous efficiencies of 10% and 50% that of current light-emitting diodes (LEDs), respectively as shown in **Figure 1.1**.[3,4] LEDs also offer further improvements via low-cost manufacturing and technological developments. Advances in materials design of the active layer, and in LED architecture, offer strategies to overcome present-day limitations such as non-radiative losses, efficiency drop-off at high voltage bias and light extraction.[5,6]

Applications of light-emitting materials are not exclusive to residential and commercial lighting, but also present in consumer electronics. Display technologies have become prevalent with the advent of smart devices and are expected to continue their rapid growth. As of 2019, 67% of the global population is subscribed to a mobile service, translating to 5.2 billion people globally and expected to continue growth in the coming years.[7] The mobile industry is a $4.1US trillion dollar per year sector, representing 4.7% of the global gross domestic product, which includes the 1.5 billion smartphones sold worldwide in 2019 alone.[8,9] These statistics highlight the size of the market of display technologies and the relative economic importance globally.

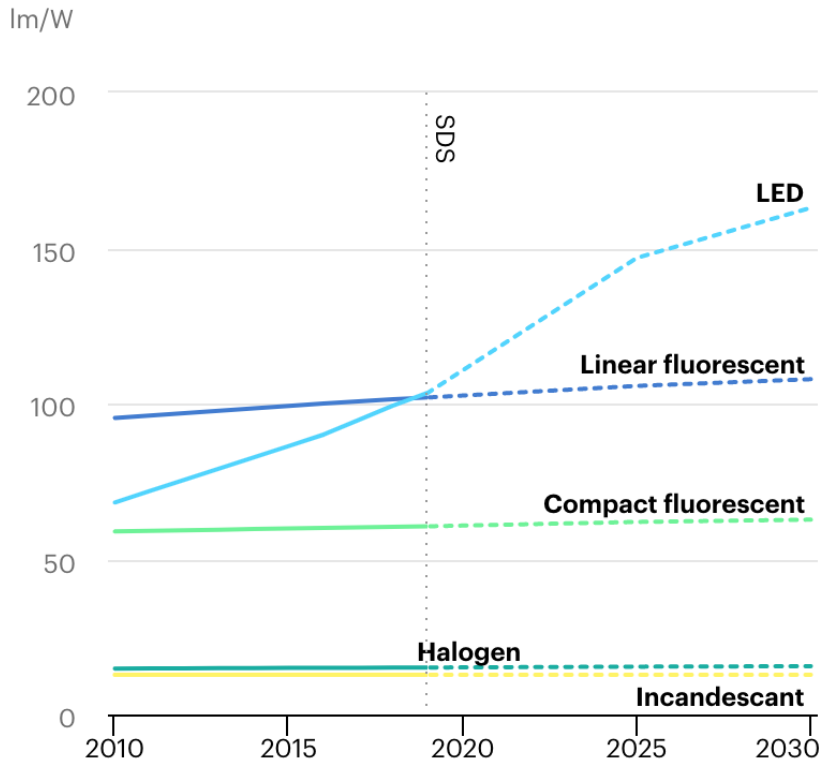


**Figure 1.1**: Luminous efficiency of currently available lighting technologies, and projected future outlook[1,3]

Advances which miniaturize smartphone display form factor, improve their stability, narrow the emission linewidths, and increase their efficiency have potential to improve user experience. This will rely on rapid materials development.[10–12] To realize this technology and capture this increasing revenue, companies such as Samsung and Nanosys have directed their research efforts towards novel materials design.[13]

Recently, colloidal quantum dots (CQDs) have emerged for solid-state light-emitting technologies owing much to their distinctive optoelectronic properties. Chalcogenide based CQD displays have already seen success in consumer electronics. They use the CQDs as colour converters in light of their narrow emission linewidths, positioning them as candidates replace organic molecules as an active material in future high-quality display technology.[11] However, limitations in the operating efficiency and colour-purity remain a challenge for chalcogenide based CQDs to reach fully electroluminescent displays. Metal halide perovskites (MHPs) are one type of CQD nanomaterial where the underlying bulk crystal takes the form $ABX_3$. Here, A and B

represent two cations bonded to a halide X, and the versatile elemental compositions possible, enables a wide set of materials with varying optical and structural properties.

**In this thesis, I seek to design and predict novel perovskite materials both experimentally and computationally with improved optoelectronic properties to realize their potential in light-emitting applications.**

In Chapter 2, I introduce the operating characteristics of light-emitting diodes such as various measures of efficiency and brightness; and I describe the measure of colour purity in light-emitting materials via their CIE coordinates. In Chapter 3, I review quantum dots and their composition and chemical synthesis, introducing the perovskite subclass, and discussing how quantum confinement in these nanoscale morphologies respectfully defines their optoelectronic properties. Chapters 4-5 focus on experimental studies which addressed the need for improved colour purity and increased stability among efficient blue-emitters. My approach toward this goal utilizes Rb-doping of perovskite QDs and tailored post-synthetic ligand treatment in reduced dimensional perovskites. In Chapter 6, I discuss how experimental efforts, when combined with new computational models, enable accelerated semiconductor discovery – the studies I report in this chapter include the experimental realization of materials informed by the accelerated computational screening. I delve into how I was able to apply deep learning models and design graph-based neural networks coupled with an evolutionary search algorithm in order to increase throughput in exploring large materials spaces. I end Chapter 6 by discussing how the combined approach also enables the uncovering of novel chemical-physical principles and heuristic rules which aid in guided and efficient materials design. Finally, I present a summary of my findings in Chapter 7, and discuss future work that could offer the next step towards improved materials design. I also consider the future role of machine learning and big data in conjunction with experimental input to further advance materials innovation.

# 2 Semiconductor Physics and Light-Emitting Diodes

In this chapter I provide a brief overview of the semiconductor physics in LEDs. I start with the pn-junction, the building block of a light-emitting diode. I then proceed to discuss the current-voltage characteristics of an LED and conclude with the metrics used to measure the relative performance of LEDs and light-emitters.

## 2.1 Semiconductors and the pn-Junction

Semiconductors exhibit conductive behaviour that falls between that of a metal and an insulator. Semiconductors also exhibit a bandgap ($E_g$), which is the difference between the conduction band and the valence band. An intrinsic semiconductor is defined as an undoped semiconductor, exhibiting equal concentrations of (thermally) excited electrons and holes, in the conduction band and valence band respectively. However, the conductive properties of the intrinsic semiconductor can be precisely tuned by intentionally introducing impurities through techniques such as doping. This strategy inserts impurities in the form of acceptor ions or donor ions, giving rise to the p-type and n-type semiconductor, respectively. The p-type is described with an excess of holes in the form of acceptors, whereas the n-type is doped with excess electrons in the form of donors.

In a junction between p and n materials, a space charge region forms. When no bias is applied and under thermal equilibrium, a built-in potential difference forms across the junction. Excess holes from the p-type diffuse into the n-type semiconductor, and excess electrons from n-type diffuse into the p-type. At the junction, this leaves a positively charged region in the n-type semiconductor and a negatively charged region in the p-type. The built-in field maintains the relative concentrations of the majority and minority charge carriers in both n-type and p-type semiconductors – corresponding to a net current of zero.

When a voltage is applied to the pn-junction in the direction shown in **Figure 2.1**, a net flow of current is observed in the event that the applied voltage overcomes the built-in potential. This reduces the energetic barrier in the space charge region, and the flow of charge carriers enables radiative recombination to occur. Radiative recombination is the process by which an electron from the conduction band combines with a hole in the valence band producing a photon of energy equivalent to this difference – the bandgap. This process is facilitated with increasing

applied voltage, as it further lowers the built-in potential charge carriers need to overcome and participate in recombination. The Shockley diode equation (**Equation 2.1**) describes the current-voltage (I-V) behaviour of the pn-junction when connected to an external power source in either forward or reverse bias as depicted **Figure 2.1**.

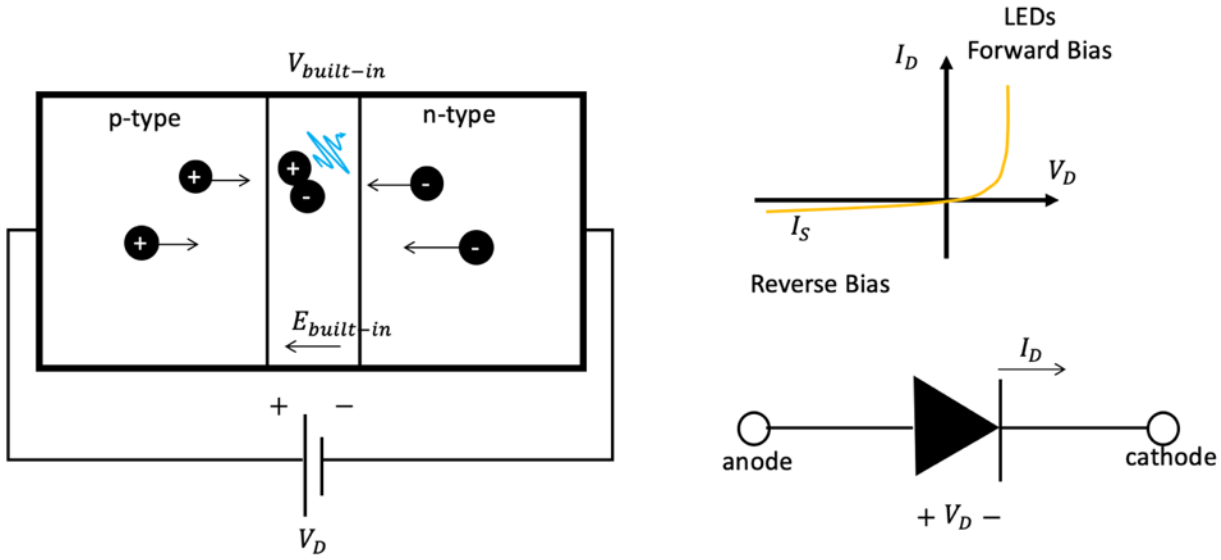


**Figure 2.1**: Architecture of a pn-junction, the I-V characteristics of a diode showing the forward and reverse bias portions when operating at different voltages, circuit device representation.

$$I = I_s\left(e^{\frac{V_D}{nV_T}} - 1\right) \tag{2.1}$$

- $I\ [A]$: diode current in amperes, or current density $\left(J, \left[\frac{A}{unit\ area}\right]\right)$;
- $I_s\ [A]$: reverse bias saturation current in amperes;
- $V_D\ [V]$: Applied voltage across the diode in volts;
- $V_T\ [V]$: Thermal voltage in volts, $V_T = \frac{k_B T}{q}, k_B = Boltzman\ Constant$;
- $n$: Diode ideality factor which falls within the range of [1,2] (ideal case = 1)

## 2.2 LED Current-Voltage Characteristics

In the context of LEDs, when a positive voltage is applied the built-in potential is reduced. At the threshold when the applied voltage overcomes the built-in potential, a net flow of current is observed. Ideally, the net current will increase linearly with increased voltage-bias and therefore

lead to higher recombination rates, generating light in the process. The output light intensity of the LED in the active region/layer will also approximately follow a linear relationship; however, a plateau is exhibited in many instances due to non-radiative losses and degradation mechanisms. This occurs at high applied voltages and has been a limiting factor in device performance. Below are examples of three different LED measurements which evaluate the device under operation. Specifically, in **Figure 2.2**, a) normalized emission spectra is shown, b) ideal output light intensity as a function of input current illustrates a linear relationship between the light intensity and current and c) applied voltage vs. current in the LED after the built-in potential is overcome showing the positive relationship.

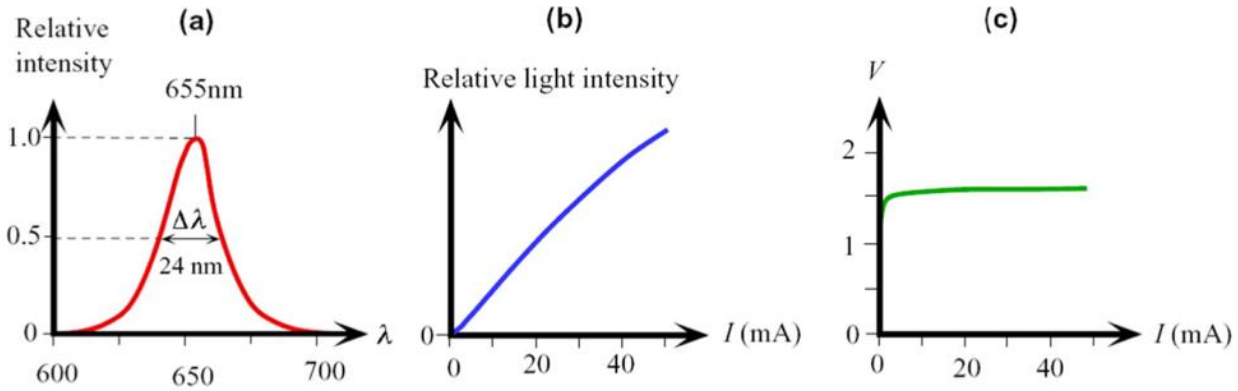


**Figure 2.2**: Characteristics of an LED in operation (when applied voltage overcomes the built-in potential, and is said to be turned on). (a) The emission spectra of a red LED centered at 655 nm with a linewidth of 24 nm; (b) Linear relationship of output light intensity as a function of the input current; (c) relationship between the applied voltage and current.[14]

## 2.3 Evaluation Metrics of Light Emitters

### 2.3.1 Luminance

Luminance is the quantity of luminous intensity per unit area of light which is travelling in a specific direction reported in units of cd $m^{-2}$. It is used to characterize the emission from a given object and represents the luminous flux per unit of projected source area. It is the photometric measure of the brightness of a display – "photometric" entails that it considers the relative sensitivity of the eye as a function of wavelength due to the rods and cones which sense the light. The displays found in computers and smartphones today have reached operating steady state luminance values in the ranges of 100 to 500 cd $m^{-2}$.[11]

### 2.3.2 External Quantum Efficiency - EQE

The external quantum efficiency is a measure of output optical quanta per input of electrical quanta that flow into the device. It takes account of photon reabsorption, Fresnel loss and critical angle loss of the device and represents the ratio of the rate of photons emitted to the rate of total carriers lost. The metric accounts for the internal quantum efficiency of the active luminescent material, responsible for producing the photons (and defined as the number of photons emitted per second over the total number of carriers lost per second, under electron-hole recombination with a value ranging from 0 to 1).

$$\eta_{external} = EQE = \frac{Total\ Number\ of\ Photons\ Emitted}{Total\ Number\ of\ Carriers\ in\ Device} = \frac{P_{out}/hv}{I/e} \qquad (2.2)$$

### 2.3.3 Photoluminescence Quantum Yield – PLQY

The photoluminescence quantum yield (PLQY) is metric that explains how efficient the light-emission process is of a luminescent material and measured as the fraction of total photons emitted per photon absorbed. It is defined as the ratio of the rate of radiative recombination to the rate of all other processes including non-radiative transitions in photoluminescence. In LEDs, the efficiency is directly impacted by the efficiency of the active material used for generating the electroluminescence. Therefore, a direct positive correlation exists between device performance and PLQY, and maximizing this quantity leads to improved efficiencies of the resulting solid-state devices.

$$PLQY = \frac{r_r}{r_{nr} + r_r} = \frac{\tau_r^{-1}}{\tau_{nr}^{-1} + \tau_r^{-1}} \qquad (2.3)$$

### 2.3.4 Colour Purity

The human eye is constructed from a set of cones which can distinguish the wavelength of light. Three cones exist and each one exhibits a corresponding sensitivity which peak at three different wavelengths, leading to the definition of the primary colours (red, green, blue). In 1930, experiments were performed to determine the link between the wavelengths of light and the perceived colours of the human eye.[15,16] This led to the development of a the colour matching functions and the CIE1931 colour space (defined by terms of *X*, *Y*, and *Z* Tristimulus values) by the Commission Internationale de l'éclairage (CIE).[17]

The International Telecommunications Union Radiocommunication (ITU-R) which governs the information and communications technology sector (in the United Nations) sets recommendation standards for a variety of applications in consumer electronics.[18–20] In the area of high-quality displays and a measure of colourimetry, the ITU-R developed a Rec. 2020 specifications set of monochromatic wavelengths for the three colour pixels comprising ultra-high-definition televisions and displays. The monochromatic wavelengths are also reported in CIE colour coordinates which are an ideal two-valued tuple used to compare various light sources for colour purity. **Table 2.1** tabulates the standards below[21]:

**Table 2.1**: Rec.2020 Standards for colour recommendations for ultra-high definition displays

| **Colour** | **Wavelength (nm)** | **$CIE_x$** | **$CIE_y$** |
|---|---|---|---|
| Red | 630 | 0.708 | 0.292 |
| Green | 532 | 0.170 | 0.797 |
| Blue | 467 | 0.131 | 0.046 |

ITU-R recommendations seek to maximize the complete set of colours visible to the human eye by expanding the overall list of possible combinations comprised of these three "primary" colours. Tristimulus values can then be used to calculate the CIE coordinates and mapped to the corresponding wavelength on the 1931 Chromaticity Chart. Reversibly, the measured photoluminescence or electroluminescence spectra can be converted into the CIE1931 coordinates by first computing the Tristimulus values $(X, Y, Z)$.[22]

These are calculated as the product of $\phi(\lambda)$ (a spectral power distribution) and each corresponding colour matching function, and integrated over the wavelength range of [390, 780] nm. The colour matching functions model the chromatic response of a human observer for the various wavelengths and account for a particular viewing angle.

$$X = \int_{\lambda} \bar{x}(\lambda)\phi(\lambda)d\lambda \tag{2.4}$$

$$Y = \int_{\lambda} \bar{y}(\lambda)\phi(\lambda)d\lambda \tag{2.5}$$

$$Z = \int_{\lambda} \bar{z}(\lambda)\phi(\lambda)d\lambda \tag{2.6}$$

- $\phi(\lambda)$: the luminescence profile as measured by the light intensity (number of photons emitted) as a function of wavelength
- $\bar{x}(\lambda), \bar{y}(\lambda)$ and $\bar{z}(\lambda)$: individual CIE colour matching functions, representing the red, green and blue components of the optical response functions of the eye respectively

Once the tristimulus values have been calculated, the CIE coordinates are computed which then enable an additional set of parameters to compare emission spectra and determine colour purity of differing luminescence spectra.

$$CIE_x = \frac{X}{X+Y+Z} \tag{2.7}$$

$$CIE_y = \frac{Y}{X+Y+Z} \tag{2.8}$$

$$CIE_z = 1 - x - y \tag{2.9}$$

However, in practice colour purity of light-emitters is often reported using the full-width at half-maximum value (FWHM) calculated from an emission spectrum (photoluminescence, electroluminescence, etc.). Often a Gaussian distribution is used to model the emission and hence allow for an approximate estimation of this dispersion measure. If a normal distribution is assumed (**Equation 2.10**), the FWHM is the width of the spectra when the amplitude is at half the peak value and can be calculated as follows:

$$f(x) = \frac{1}{\sqrt{2\pi}\sigma} e^{-\frac{1}{2}\left(\frac{x-x_0}{\sigma}\right)^2} \tag{2.10}$$

$$FWHM = 2\sqrt{2ln2}\sigma \tag{2.11}$$

Here it follows that $\sigma$ is the standard deviation, and $x_0$ is the central peak wavelength, ideally from one emission profile. This is illustrated in **Figure 2.3** as a sample example, illustrating the FWHM of a normalized and ideal Gaussian profile.

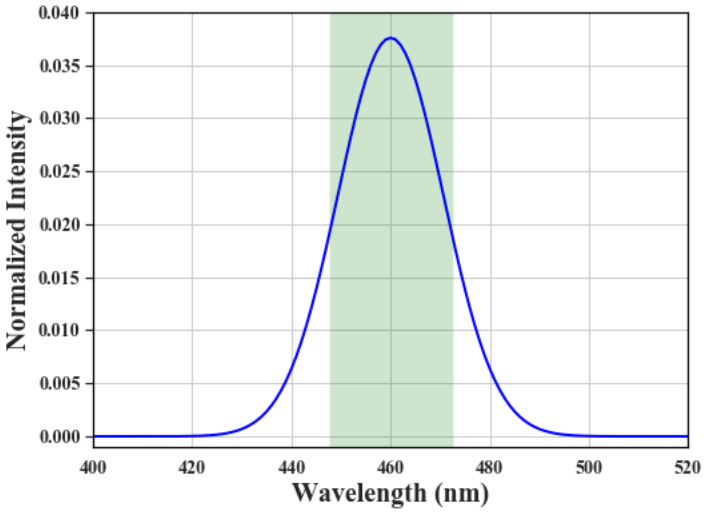


**Figure 2.3**: Example of a simulated Gaussian emission spectra, centered at 460 nm with a FWHM of 25 nm.

In the context of blue emitters (**Table 2.2**), the target emission should ideally be centered at 467 nm and, and by achieving a narrow full-width at half-maximum (FWHM< 25 nm) and minimal red tail, meet the CIE colour coordinate: [($x_{blue}$ = 0.131, $y_{blue}$ = 0.046)]. Red tails, which lie above the Gaussian profile in the emission spectra are detrimental as they limit the ability to produce colour pure devices.

**Table 2.2**: Test case and comparison of simulated Gaussian profiles relative to the ITU-R Rec.2020 blue coordinate.

| | **Wavelength (nm)** | **FWHM (nm)** | **Standard Deviation (nm)** $\boldsymbol{\sigma = \frac{FWHM}{2\sqrt{2ln2}}}$ | **CIE (x,y)** |
|---|---|---|---|---|
| Target Blue (Rec.2020) | 467 | - | - | (0.131, 0.046) |
| Gaussian 1 | 467 | 25 | 10.62 | (0.122, 0.076) |
| Gaussian 2 | 460 | 25 | 10.62 | (0.133, 0.051) |

Modelling the emission with a high degree of accuracy in physical systems such as quantum dots is poor due to the non-ideal conditions of synthesis resulting in inhomogeneous broadening and non-Gaussian distributions. To add complexity, emission profiles are not a stationary process and evolve over time. Therefore, improvements in developing a standard metric

to measure device performance in terms of colorimetry were established by the scientific community and industry and are continuously updated by organizations such as the ITU-R.

### CIE Chromaticity Chart

To demonstrate this method of colour-purity, I computed the CIE coordinates of three PQD solutions from their corresponding PL spectra. I plot these and compare them to the standardized Rec.2020 as a reference (black lines and triangles, **Figure 2.4**). Ideally, to maximize the colour gamut of a display, the LED spectra should approach the vertices of the colour space and be as close as possible to the Rec.2020 standards. For blue-emitters this is achieved by extremely narrow linewidths and emissions centered at 467 nm,

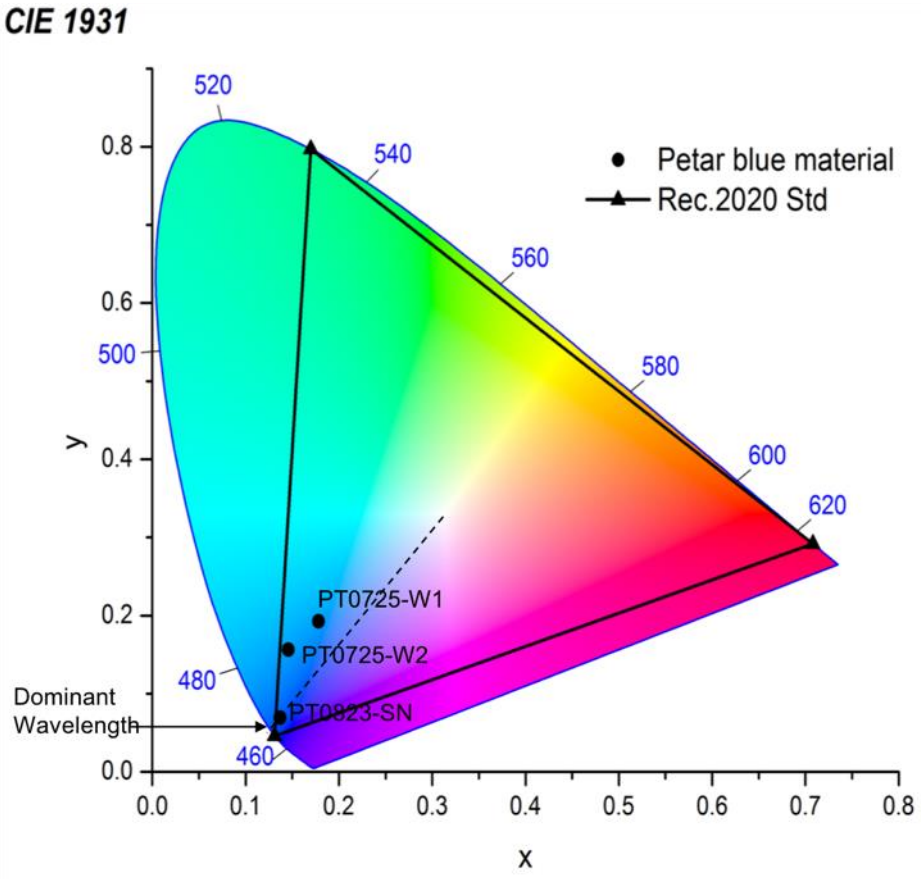


**Figure 2.4**: CIE plot of three colloidal quantum dot solutions, and the recommended standard for ultra-high-quality displays as suggested by ITU-R.

## 2.4 Summary

In this chapter, I introduced the pn-junction – the foundation for LEDs, and the various metrics used to characterize the performance of these devices. In the following chapter, I introduce colloidal quantum dots and perovskites. I present the structural and optical properties of these systems and their application in solution-processed devices. The concepts presented in chapter 2 and 3 will be the basis for the further advances of the findings throughout the rest of the thesis.

# 3 Colloidal Quantum Dots and Perovskites

## 3.1 Colloidal Quantum Dots

Colloidal quantum dots (CQDs) are semiconductor nanoparticles which have attracted interest in the last decade owing much to their distinctive optoelectronic properties. These particles typically exhibit length scales of 1 nm – 10 nm and are smaller than the exciton Bohr radius of their bulk counterpart, leading to quantum confinement. The consequence of this is that CQDs exhibit size- and composition-dependent optoelectronic properties, offering tailored applications in lasing, light-emission and harvesting and photodetection. An inverse relationship exists between the quantum dot size and bandgap as shown in **Figure 3.1**. As the quantum dot size decreases, the bandgap increases, shifting to higher energies and shorter wavelengths. The bandgap is also a function of the elemental composition which can exist as a binary, ternary or quaternary system. Chalcogenide quantum dots (CdSe, ZnSe and In(Ga)P, and InP) are one of the most widely studied set of materials, recently paving the way for companies such as Samsung to adopt their use as colour converters for displays in consumer electronics.[10] Tunability of bandgap enables in precise tailoring of the photoluminescence and absorption peaks throughout the entire electromagnetic spectrum.

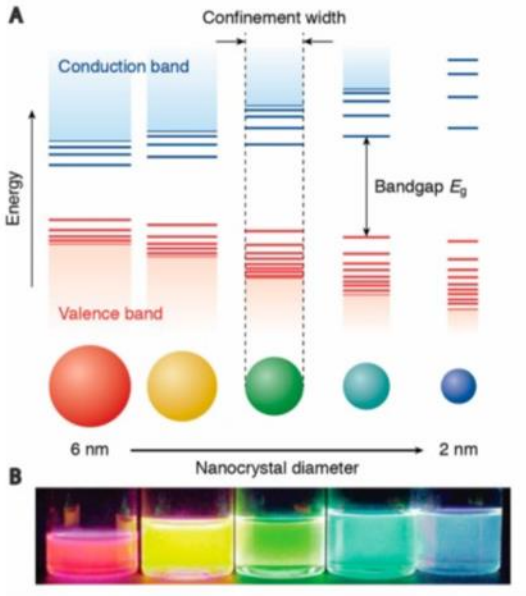


**Figure 3.1**: Energy band diagrams of semiconductor quantum dots highlighting the bandgap as a function of size. Reprinted with permission from Reference[23] , *The Journal of Physical Chemistry Letters* 2017 8 (17), 4077-4090)

Facile solution-processing techniques positions CQDs as alternatives to high-temperature processed conventional epitaxial materials for display technologies in light of their low-cost manufacturability and compatibility with flexible substrates.[24] In this Chapter, I review the synthesis of CQDs and their various geometries and introduce a special class of CQD materials which will be the main system studied throughout the thesis – perovskites.

## 3.2 Synthesis and Film Fabrication

One of the most prevalent methods to synthesize quantum dots include the hot-injection method pioneered by C. Murray, D. Norris and M. Bawendi in 1993.[25] Hot-injection synthesis has become the mainstay of synthesizing colloidal dispersions of quantum dots, applicable in chalcogenide and perovskite systems. Hot-injection produces semiconductor quantum dots via a two-stage process: rapid nucleation and controlled particle growth. This begins by dissolving the constituent starting precursors of desired material in a coordinating solvent at elevated temperatures with the addition of organic ligands. The role of the organic molecule is to produce a reactive organometallic species enabling aggregation and initiation of the starting nuclei. In the nucleation stage, these organometallic precursor solutions are rapidly injected into a coordinating solvent at elevated temperatures to initiate particle growth. The organic molecules are also responsible for stabilizing the semiconductor nanoparticles during growth as they attach to the quantum dot surface producing a colloidal dispersion. Following injection and after nucleation, particle growth proceeds through a homogeneous diffusion-controlled process, whereby smaller QDs grow at a faster rate relative to their larger counterparts, narrowing the size distribution of the resulting species.[26] Over time as the precursor concentration decreases, particle growth plateaus and the resulting solution contains a relatively monodisperse set of nanoparticles. One main advantage of hot-injection synthesis is the versatility and tunability it provides as a function of the reaction conditions. Adjusting the reaction temperatures, reaction time, concentrations of the precursors and surfactants leads to various nanostructured quantum dots with tailored optoelectronic properties.[27,28] For this reason, hot-injection synthesis has been employed to synthesize chalcogenide II-VI, III-V and perovskite quantum dots.

After the synthesis, thin films of CQDs can be fabricated to form uniform layers of the semiconducting material for applied use in devices. Examples of thin-film deposition techniques include chemical bath, spin-coating, dip-coating, doctor blade, metering rod, spray-coating, screen-printing, inkjet printing and aerosol jet spraying to name a few.[29] In the laboratory setting,

spin-coating has widely been adapted as the typical method for high through-put device fabrication.

## 3.3 Solution-Processed LEDs

The architecture of a typical thin-film LED is shown in **Figure 3.2**. The device is comprised of a transparent conductive electrode – TCO, (ITO, indium tin oxide), an electron transport layer/hole blocking layer (ETL, TBPi), the active luminescent (semiconductor, quantum dot, organic molecule) material responsible for producing light, a hole transport layer/electron blocking layer (HTL, PEDOT:PSS/Poly-TPD), and a top metal contact (LiF/Al). The transparent electrode provides the conductivity and transparency required for efficient charge injection and photon extraction. Charge carriers are injected from electrodes into the active material, which undergo a radiative transition, resulting in the emission of a photon with an energy equal to the material bandgap. Efficient LEDs are obtained by an improvement in the charge carrier injection, facilitated by two additional layers that sandwich the active material and act as electron blocking and hole blocking barriers. This allows electrons to be injected from one side, and not overflow past the active layer (blocking function of the HTL); symmetrically for holes.

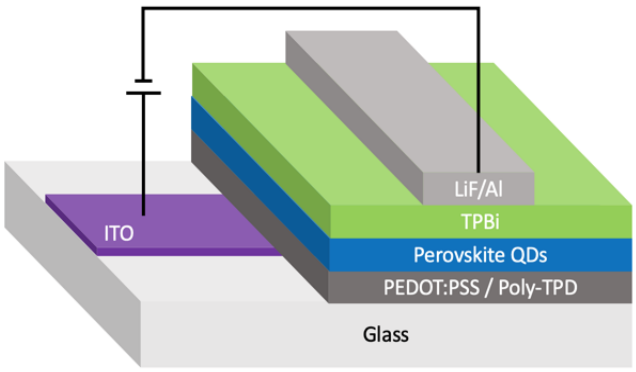


**Figure 3.2**: Schematic of a typical thin-film LED, showing the various components.

## 3.4 Industrial Relevance of Solution Processed LEDs:

Solution-processed LEDs offer lighting and display technologies at lower costs.[29,30] Examples of such technologies include organic LEDs (OLEDs), quantum dot LEDs (QLEDs), and more recently perovskite LEDs (PeLEDs). Though, performance of these devices is inferior to that of the LCD technologies currently dominating the display industry. OLEDs have recently become

widespread in modern-day smartphone and television displays, leading to thinner displays. One limitation of organic molecules is the broad emission linewidths which exceed 40 nm[31], limiting their applicability as colour pure devices. Blue-emitting organics have lagged in operational stability, displaying lifetimes one order of magnitude shorter than their green and red counterparts.[32]

Colloidal quantum dots offer an alternative to organic molecules, displaying narrower emission linewidths due to quantized energy levels, leading to more purer colours as shown in **Figure 3.3**.[33] However, CQDs require surface passivation by an organic ligand or inorganic shell to reduce these defect states. Defects are detrimental to the optoelectronic efficiency of the material, reducing charge injection and hence limiting efficient recombination of the charge carriers– an essential for light-emission. The stability of QLEDs is lower than that of OLEDs making current QLEDs unfit for commercial implementation. The blue QLED exhibits operating lifetimes of 30 minutes before degrading to 50% of its initial luminance.[34] Relative to organics, QLEDs are a nascent technology, and as such, much remains to be investigated to improve their performance and stability.

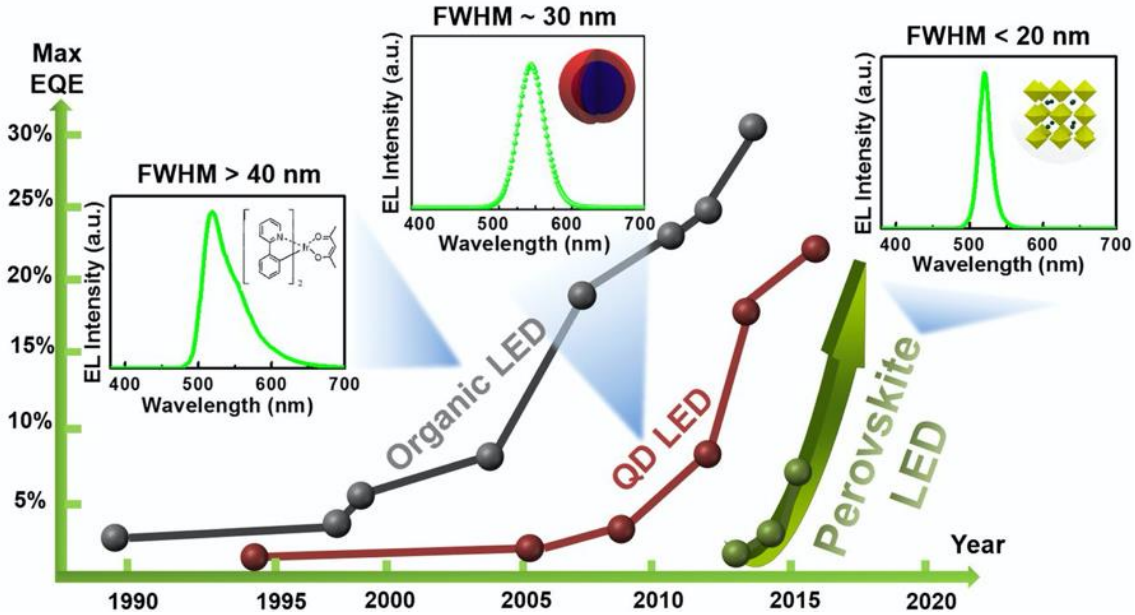


**Figure 3.3:** Figure is reprinted with permission (Reference [33], Copyright (2016) National Academy of Sciences)

## 3.5 Perovskites – An Emerging Semiconductor

Metal halide perovskites (MHPs) are an emerging class of CQD nanomaterials of the typical form $ABX_3$ (ternary composition, although quaternary and higher exist) as illustrated in **Figure 3.4**. In the ternary case, $A^+$ and $B^{2+}$ represent two metal cations bonded to an anion $X^-$, forming a variety of crystals structures (two of the most common shown below). Perovskites possess three main characteristics for optoelectronics:

1. Facile solution processing, resulting from low chemical activation barriers[35];
2. Defect tolerance, a consequence of low probability of existing mid-gap trap states and efficient charge carrier mobilities[36];
3. Tunability of their optical properties, achieved by quantum confinement or by compositional engineering (substituting and alloying the A, B, X constituents in the crystal)[35,37].

It is this combination of multiple properties that has led to their application in light-emitting devices[30,38], lasers[39,40], photovoltaics[41–43] and photodetectors[44]. Perovskites have been investigated for photovoltaic applications over the past 10 years, leading to the most rapid progress in photovoltaic performance ever observed and have no sight of subsiding in the field of optoelectronics.[45]

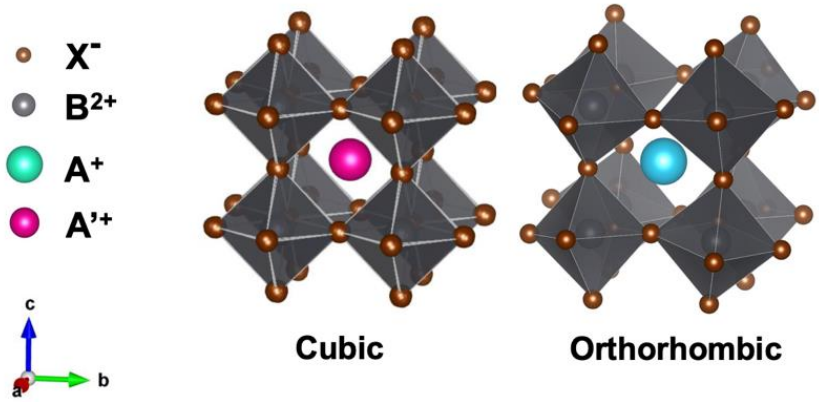


**Figure 3.4**: Typical inorganic perovskite crystal structures take the form of an ideal cubic ($A'BX_3$) and orthorhombic ($ABX_3$) configuration. In both cases, $A'^+$, $A^+$, and $B^{2+}$ represent three different cations, which are bound an anion element $X^-$. In the common $ABX_3$ formula, the A/A' cation is surrounded by $BX_6$ octahedra. The orthorhombic crystal structure displays tilting of the $BX_6$ octahedra as a result of the ionic radii of the A-site radii, influencing the bonding within the overall structure and deviation from the ideal cubic structure.

## 3.6 Nanostructured Geometries of Perovskites

Perovskite quantum dots exist in the 3D crystal lattice of the typical form $ABX_3$ and crystallize in a multitude of structures, offering spatial confinement in all three principal directions. Recent studies have shown that reducing the dimensionality of the perovskite towards 2D, commonly referred to as nanoplates, opens up new avenues to apply nanostructured geometries.[46] This is achieved when the typical perovskite structure incorporates organic molecules leading to the formation of hybrid perovskite materials which exhibit quantum tunable optical properties, just as in the case of QDs.[43] They have shown to exhibit the superior optoelectronic properties of their inorganic PQD counterparts – namely facile solution-processing at room-temperatures.

In the case of these 2D nanostructures, quantum confinement is achieved in one direction, where a molecular spacer acts as an intercalating ligand separating the distinct perovskite layers. The building block of these structures take the form of $A'_mA_{n-1}B_nX_{3n+1}$, whereby $A'_m$ represents an organic divalent ligand (m = 1) or a monovalent (m = 2) cation species, A represents a mono valent organic or inorganic cation, B a divalent metal cation and X an anionic species such as the set of halides. The value *n* in this formula represents the number of perovskite layers within a given quantum well – and thereby leads to the observed bandgap of the material. The edge cases of $n = 1$ and $n \rightarrow \infty$ are classified as the 2D and 3D system as demonstrated in **Figure 3.5**. A special case exists which includes $n > 1$, whereby finetuning the constituent elements comprising of the system allow for quasi-2D geometries to be designed. Choice of ligand, solution temperatures, annealing protocols and precursor ratios are examples of variables which can be controlled to produce novel nanostructures of perovskites.

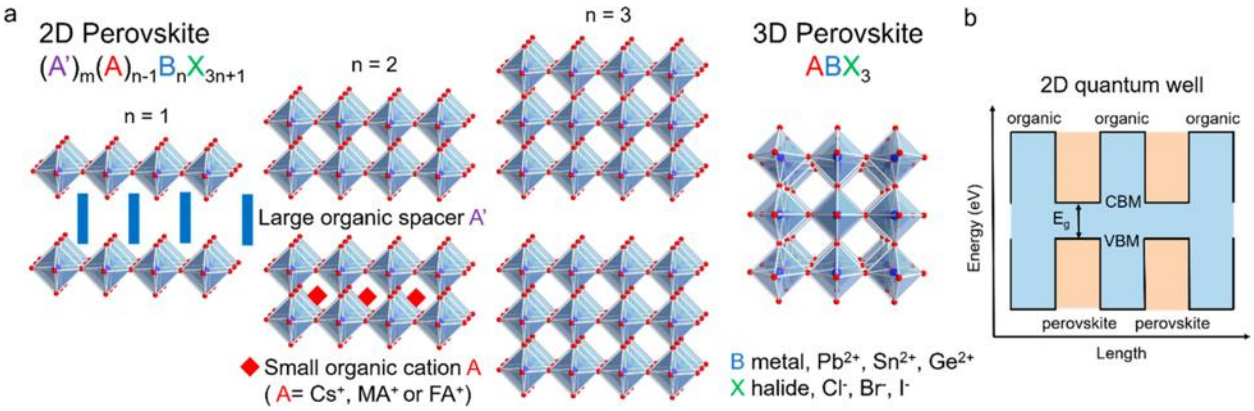


**Figure 3.5**: Crystal structures of 2D perovskites and 3D perovskites, as increasing organic ligands finetune the quantum confinement. 2D Quantum wells are formed when the intercalating organic ligand species acts as a spacer, creating well-defined sheets, enabling various geometries to be formed via the functional groups of the organic compound. Reprinted with permission from (*J. Am. Chem. Soc.* 2019, 141, 3, 1171-1190, Reference [46]). Copyright (2019) American Chemical Society.

## 3.7 Limitations in Blue Perovskite LEDs

### 3.7.1 Spectral Stability

PeLEDs offer narrow linewidths, high PLQYs, and tunable material systems which could potentially surpass the obstacles that have prevented the advance of OLEDs and QLEDs. However, PeLEDs still require significant progress in efficiency and operating stability. EQEs have exceeded 20% in the green[47], and red[48]; however, remain below 3% in blue.[49] Although immense progress has been made in improving the EQEs, operating stability has also presented a major challenge. Green and red PeLEDs exhibit operating lifetimes tens of hours before degrading.[48,50] However, there has been early success in improving stability by the means of surface passivation.[51,52] Specific organic ligands such as phosphine oxides have been shown to inhibit degradation and result in improved stability with high efficiency of green PeLEDs (up to 33 hrs with over 15% EQE)[50]. In the case of blue, two-dimensional nanostructures have been utilized to obtain highly luminescent films with PLQYs over 80%, leading to bright PeLEDs with EQEs of 1.3%.[53] Despite these shortcomings, perovskites, a relatively new class of materials in the field of light-emission have shown great promise and rapid improvement.

### 3.7.2 Colour Purity and Deep-blue Emission

The two widely-used approaches to achieve deep-blue emission include: (1) a mixed-anion perovskite quantum dot of both Br/Cl; and (2) reduce the dimensionality of the 3D bulk perovskites to form well-defined and emitting quantum wells. Unfortunately, the former strategy suffers from halide segregation yielding spectral instability in colloidal solutions, films and in operando as active materials in LEDs.[54,55] The latter is limited by a lack of precise control of the nanoscale morphology and the molecular ligands available to synthesize the desired perovskite quantum wells. In light of these limitations, there remain opportunities to develop materials for practical, stable and efficient light-emitting devices. Below I summarize a set of $CsPbX_3$ nanocrystal-based materials and devices which employed the aforementioned strategies to attain blue emission (**Table 3.1)**. Limited progress in exploring novel compositions and designing alloys of spectrally stable perovskite blue emitters has hindered their application in the next-generation display technologies.

**Table 3.1**: Blue perovskite colloidal quantum dots and respective performance metrics

| System | PLQY [%] | FWHM [nm] | $\lambda_{EL/PL}$ [nm] | Peak EQE [%] | Peak Luminance [cd $m^{-2}$] | Luminance @ Peak EQE [cd $m^{-2}$] | Spectral Stability |
|---|---|---|---|---|---|---|---|
| *Treated $CsPbBr_3$*[56] | 70 | 22 | 490 | 1.9 | 35 | ~ 5 @ 1.9% | × |
| *$CsPbBr_xCl_{3-x}$ QDs*[57] | - | 19 | 480 | 0.007 | 8.5 | < 1 | × |
| *$CsPbBr_xCl_{3-x}$ QDs*[58] | 60 | 30 | 455 | 0.07 | 742 | N.R | × |
| *$CsPbBr_3$ QDs*[59] | 35-50 | 40 | 475 | 0.0003 | 2 | ~1 | N.R |

*Note: × refers to spectrally unstable, whereas N.R refers to not reported*

## 3.8 Summary

In 2016, at the beginning of my graduate studies, the set of deep-blue perovskite materials suffered from poor device performance as seen in low EQE values and spectral shifts (**Table 3.1)**. I focused my studies on investigating and developing perovskite materials that would overcome the problem of spectral and operating instability. In Chapter 4 and 5, I focus on experimental strategies to tune optoelectronic properties via compositional engineering and nanostructure-based bandgap modulation towards the goal of deep-blue devices and stable electroluminescence. In Chapter 6, I carry out computational studies and incorporate machine learning methods to explore materials space rapidly and discover a new set of perovskites with targeted bandgaps. Post-predictive analysis led to chemical interpretability, enabling me to propose candidate materials which were then experimentally realized and verified.

# 4 Enabling Deep-Blue Emission in Perovskite Quantum Dots

Based on: **Todorović, P.**[†], Ma, D.[†], Chen, B., Quintero-Bermudez, R., Saidaminov, M.I., Dong, Y., Lu, Z.H. and Sargent, E.H., 2019. Spectrally Tunable and Stable Electroluminescence Enabled by Rubidium Doping of CsPbBr3 Nanocrystals. *Advanced Optical Materials*, *7*(24), p.1901440.

Blue-emitting perovskite materials represent a vast and unexplored space. Their possibilities emerge from the wide available range of chemical compositions and nanoscale geometries.

In this chapter, I explore perovskite quantum dot composition, as well as the nanoscale morphology, that can be achieved using chemical synthesis. I show that a mixed cation approach (A-site of the $ABX_3$) in the typical orthorhombic perovskite systems led to spectral tunability with emission across the blue. I then examined the importance of ligand interactions and quantum dots during synthesis and achieve narrow-linewidth deep-blue emitting materials. I then lever this strategy to fabricate solid-state devices. The resulting LEDs exhibited the highest luminance values at the maximum external quantum efficiencies in both deep-blue and blue spectra compared to the best previously reported perovskite QD LEDs.

This work was conducted in collaboration with postdoctoral fellow Dr. Dongxin Ma, whom I share first co-authorship. Dr. Ma carried out fabrication and thermal evaporation of the light-emitting devices in Professor Zheng-Hong Lu's Lab. I led the materials synthesis, data collection, characterization, and data analysis and writing of the manuscript. Other co-authors contributed in experimental guidance, UPS, TEM and EDX measurements.

## 4.1 Introduction

In the previous chapter I reviewed the progress made in perovskite QDs for use as efficient LEDs and presented an overview of the limitations in blue-emitting materials. Pure QDs of $CsPbCl_3$ or $CsPbBr_3$ are not able to achieve the desired blue wavelengths as recommended by the ITU-R Rec.2020 standards.[18] Therefore, in order to achieve blue emission in these systems, a mixed-anion approach is employed which relies on mixtures of both Br and Cl in the archetypical $APbX_3$ perovskite crystal. Despite reasonably high-quality solution PLQYs, films fabricated from these materials exhibit large spectral shifts under operating conditions preventing their function as stable and efficient light-emitting devices.[56–58] This spectral shift is attributed to halide segregation that occurs under applied voltage bias. In addition to the composition modulation, size-tuning and varied nanoscale geometries have enabled tunable systems throughout the blue.

I set out to reduce spectral instability in blue-emitting PQDs by utilizing a mixed-cation approach within a pure bromine perovskite crystal phase. Specifically, I investigated the incorporation of $Rb^+$ into $CsPbBr_3$ QDs during chemical synthesis to enlarge the bandgap while prohibiting the voltage-induced phase segregation. I sought to understand how, and to what degree, $Rb^+$ incorporation led to tunable optoelectronic properties; and hence the resulting stability in solution and film under operating conditions. I studied how the reaction conditions and kinetics influenced the formation of various nanoscale geometries enabling a wide spectrum of blue-emitting materials.

I then fabricated tunable light-emitting diodes which levered the photophysical properties of the novel $Rb_xCs_{1-x}PbBr_3$ nanocrystals. Devices exhibited stable and narrow electroluminescence emissions, while simultaneously demonstrating record high luminance values at peak operating external quantum efficiencies: 93 cd $m^{-2}$ at 0.75% and 29 cd $m^{-2}$ at 0.11% for sky-blue (490 nm) and deep-blue (464 nm) emission, respectively.

## 4.2 Synthesis

Blue perovskite QDs have been shown to achieve high solution PLQYs.[37] However, translating this into film and ultimately practical solid-state devices remains a challenge. The mixed anion perovskite systems used today suffer from spectral instabilities in solution; and even more acutely in devices under voltage bias. The instability is attributed mainly to electric field

induced ion migration during device operation of the halide species.[60] This broadens the emission profile, limiting application in high-efficiency LEDs. It is of interest to mitigate the spectral shift by developing new sets of candidate materials.

I hypothesized that the higher concentration of anions within the ionic crystal (3 times more prevalent in the $ABX_3$ structure) was one of the main factors contributing to spectral instability. I focused therefore on the $CsPbBr_3$ set of perovskites as the control materials to implement the mixed cation strategy. I posited that Rb could sit at the A-site due to its identical (+1) oxidation state relative to Cs and similarity in terms of chemical and physical properties. I did note the difference in the ionic radii, a factor accounted via the tolerance factor (**Equation 4.1**) of the proposed $Rb_xCs_{1-x}PbBr_3$ system. Stable perovskites generally exhibit a factor greater than 0.85 and a pure $CsPbBr_3$ crystal structure is estimated to be 0.92.

$$t = \frac{r_A + r_X}{\sqrt{2}(r_B + r_x)} \tag{4.1}$$

I used the Goldschmidt formula (**Equation 4.1**) to estimate an absolute maximum threshold value of roughly 70% for a stable mixed Rb-Cs blend, which agreed with literature reports (pure $RbPbBr_3$ does not exist under ambient conditions).[61] At higher Rb concentrations, a large structural distortion within the crystal occurs and prohibits the formation of the emissive orthorhombic phase, which is necessary for optoelectronic applications. Rb incorporation causes tilting of the $PbX_6$ octahedra, while decreasing the overall orbital overlap (between the Pb 4f and X 3d) and hence enlarges the bandgap relative to a pure $CsPbBr_3$ crystal.[62–66] These initial calculations helped guide my colloidal synthesis.

I proceed with the hot-injection synthesis method[37] to achieve the doped $Rb_xCs_{1-x}PbBr_3$ QDs. In these syntheses, reactive metalloorganic precursors such as Cs-oleate are injected into a solution of dissolved $PbX_2$ precursors capped with molecular ligands at elevated temperatures. In this case, I found that when I introduced a mixture of Rb-oleate and Cs-oleate (equal volumes) and adapted the procedure of Protescu et al. (**Appendix A.1**), I was able to obtain blue emissive nanocrystals.[37] I observed, following injection, a colour change indicative of PQD formation. UV lamp excitation of the reaction flask would confirm that this dual cation strategy exhibited a blue emission profile. However, under identical reaction conditions when I used Cs-oleate as the sole precursor, I witnessed a green emission profile under UV excitation. I followed typical protocols to purify the

solutions[37,67,68], removing any unreacted by-products, and finally stabilize the colloidal solutions in nonpolar solvents such as hexane, octane or toluene to use for further studies and characterizations as shown in **Figure 4.1**.


**Figure 4.1**: Solutions of synthesized and purified PQDs under UV excitation, dispersed in hexane (left: $Rb_xCs_{1-x}PbBr_3$ – blue, right: $CsPbBr_3$ – green)

### 4.3 Photophysical Studies and Light-Emitting Properties

To verify the doping mechanism, I measured the photoluminescence and absorption spectra of the resulting of solutions. The photoluminescence profiles (**Figure 4.2**) exhibited a blue shift in the emission profile (to higher energies) as indicated by the peak shifting towards shorter wavelengths. These initial observations led me to investigate the reaction temperature and stabilizing ligand ratio (OA:OLA) as a path towards controlling the nanocrystal size. First, I found that at a fixed ratio of ligands and Rb:Cs, reduction in the synthesis reaction temperature led to the formation of smaller particles, and therefore an even larger shift in the PL peak to shorter wavelengths as seen in **Figure 4.2**. The symmetric PL profiles indicated that the PQDs retained their isotropic cubic structure even at reduced temperatures. However, when the ligand concentration of OA:OLA was changed from 1:1 to 2:1, deep-blue emitting colloidal nanoplates were synthesized as attributed by the asymmetric profile and a stronger quantum confinement effect.

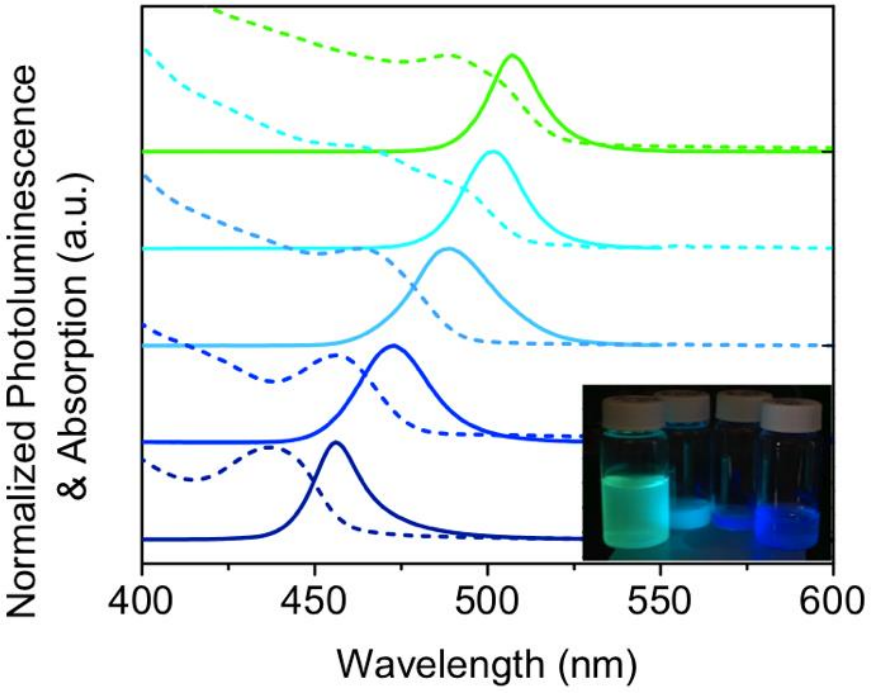


**Figure 4.2:** Optoelectronic and structural characterization of $Rb_xCs_{1-x}PbBr_3$ PQDs. a) Photoluminescence and absorption spectra of synthesized solutions. A reference of $CsPbBr_3$ QDs (green with an emission peak of 510 nm) and $Rb_xCs_{1-x}PbBr_3$ PQDs at various reaction temperatures showing spectral tunability.

The PL spectra of the nanoplates peaks within the ranges of 450 – 470 nm with narrow emission linewidths of less than 20 nm, positioning them as promising candidates to meet the Rec.2020 specifications (**Figure 4.3**). In addition, I measured the PLQY of the resulting solutions, which varied from an absolute of 60% for the deep-blue to 90% for the sky-blue emitting species, comparable to that of the control $CsPbBr_3$ QDs (**Table 4.1**).[37,68] I then studied the PL lifetime decay and discovered that the radiative lifetimes of the $Rb_xCs_{1-x}PbBr_3$ was slightly shorter than that of pure $CsPbBr_3$ PQDs when synthesized under identical reaction conditions (**Appendix B1 – Figure 1 and B1 Table 1**). In these experiments, I found that lower reaction temperatures led to decreased radiative lifetimes which may be attributed to a decreased particle size and increased surface trap formation which is prevalent in nanoplates and hence highlighted by slightly reduced PLQYs relative to the isotropic cubic species.[60] Surface passivation treatments by introducing solvated solutions of $PbBr_2$ post synthesis have been reported to reduce the trap formations and

improve PLQY.[28,60] As a result, the mixed cation strategy tuned the optical properties, confirming the original hypothesis and enabling a range of blue-emitting materials.

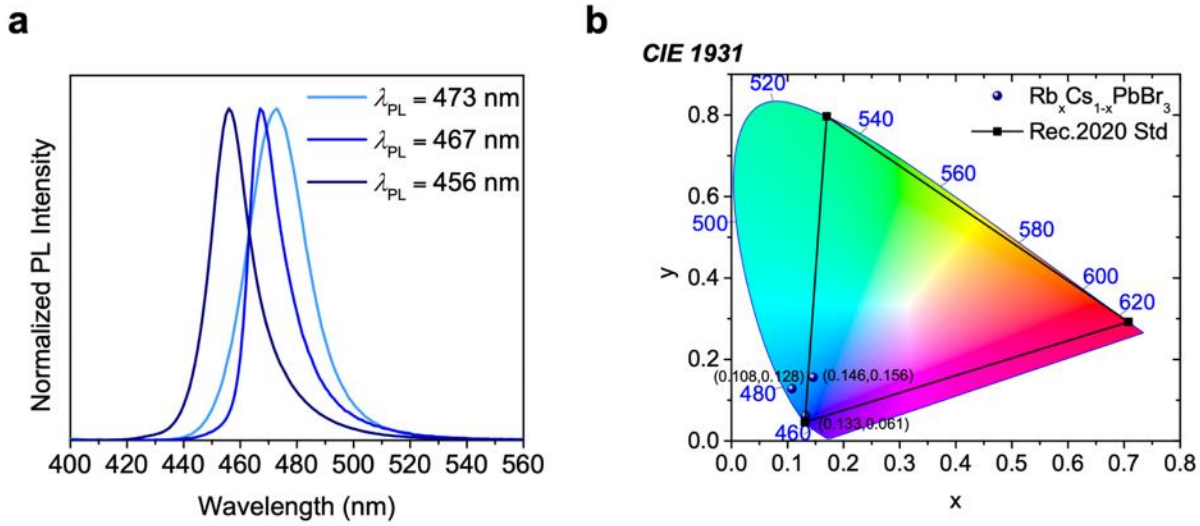


**Figure 4.3:** (a) Photoluminescence spectra of three $Rb_{0.4}Cs_{0.6}PbBr_3$ solutions, demonstrating narrow emission linewidths (< 20 nm). (b) CIE plot of the three solutions, indicating extremely colour pure materials approaching the edge of the colour gamut and meeting the Rec.2020 Standards for blue-emitting materials. Solutions and their respective (x,y) coordinates: λ=456 nm, (0.133, 0.061); λ=467 nm, (0.146, 0.157); λ=473 nm, (0.108, 0.128).

**Table 4.1:** Photoluminescence Quantum Yield (PLQY) measurements of PQDs in hexane.

| **Solution** | **Temperature [°C]** | **OA:OLA** | **$\lambda_{PL}$[a)] [nm]** | **PLQY [%]** |
|---|---|---|---|---|
| $CsPbBr_3$ | 150 | 1:1 | 510 | 93 |
| $Rb_xCs_{1-x}PbBr_3$ | 150 | 1:1 | 490 | 80 |
| $Rb_xCs_{1-x}PbBr_3$ | 135 | 1:1 | 480 | 70 |
| $Rb_xCs_{1-x}PbBr_3$ | 120 | 1:1 | 475 | 66 |
| $Rb_xCs_{1-x}PbBr_3$ | 120 | 2:1 | 465 | 60 |

## 4.4 Structural Characterization

I fabricated PQD films by drop-casting and spin-coating. I then studied the relationship between the synthetic reaction conditions and $Rb^+$ doping concentration via x-ray photoelectron spectroscopy. The resulting XPS traces are shown in **Figure 4.4**, which indicate that a $Rb^+$ signal is observed only in the Rb-doped colloidal dispersions (**Figure 4.4a**). The Cs 3d peaks exhibited a shift to lower binding energies suggesting that Rb incorporates into the perovskite nanocrystal. Previous reports have reasoned that this occurs due to change in the electronic density.[69] I then quantified the specific amounts of Cs:Rb within the various materials by integrating the area of the respective XPS traced yielding atomic Cs:Rb ratio of 2:1 for nanocubes and 1.5:1 for nanoplates. This suggested that the resulting compositions were of the form $Rb_{0.33}Cs_{0.66}PbBr_3$ and $Rb_{0.4}Cs_{0.6}PbBr_3$ respectively, matching that of the theoretically calculated values used to pursue the studies (**Table 4.2**).

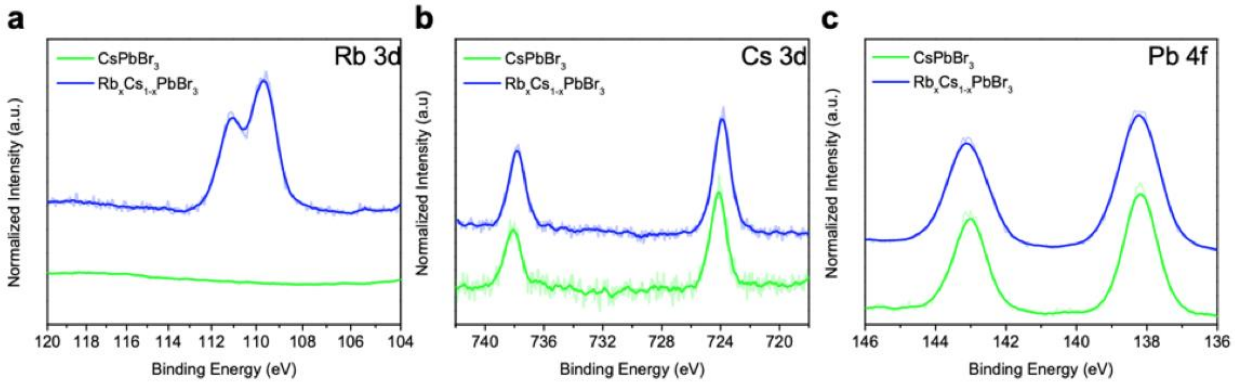


**Figure 4.4:** XPS Measurements (raw data and 10-point running average smoothing – thick line) of Rb (a), Cs (b), Pb (c) of drop-cast PQD films. Rb was present in the synthesized $Rb_xCs_{1-x}PbBr_3$ NCs (for all temperatures and reaction conditions).

**Table 4.2:** Calculated atomic ratios by integrating the spectra over the specified energy range for each element of Rb-doped $CsPbBr_3$ quantum dots thin-films. A 1:1 ratio is present for (Rb+Cs):Pb as expected, but in certain instances higher Br concentration may arise from mixed phases or bromine rich surfaces.

| $\lambda_{PL}$ [a)] [nm] | Temperature [°C] | Cs [At. %] | Rb [At. %] | Pb [At. %] | Br [At. %] | Ratio Rb:Cs |
|---|---|---|---|---|---|---|
| 490 | 135 | 14.2 | 2.9 | 15.5 | 67.3 | 0.2:0.8 |
| 475 | 120 | 12.4 | 5.1 | 15.3 | 67.1 | 0.3:0.7 |
| 465 | 120 | 10.0 | 6.6 | 15.4 | 68.0 | 0.4:0.6 |

In addition to XPS, I performed powdered X-ray diffraction measurements to assess the crystal structure and corroborate the previous findings. I found that in films of $Rb_xCs_{1-x}PbBr_3$ the XRD spectra shift to larger $2\theta$ angles **Figure 4.5**. In particular, the main peaks of the control $CsPbBr_3$ QDs occur at values of 15.08 ° and 30.42 °; corresponding to the (100) and (200) crystal planes in a cubic crystal structure. However, upon the incorporation of $Rb^+$, these values increase to 15.26 ° and 30.66 ° respectively. The increase is expected as $Rb^+$ replaces $Cs^+$ in the crystal structure which inherently increases the Pb-Br chemical bond and a tilt of the $PbBr_6$ octahedra. This in turn shifts the XRD spectra towards larger $2\theta$ angles which is consistent with the identical case of $Cl^-$ doping in $CsPbBr_3$ NCs ($r_{Cl^-} > r_{Br^-}$) as reported.[70,71] I then looked to examine the pure $RbPbBr_3$ literature values (blue) and find that the observed peaks match the experimental $Rb_xCs_{1-x}PbBr_3$ orthorhombic perovskite QDs, evidencing successful incorporation of $Rb^+$ within the crystal as the peaks shift in the direction of the pure Rb-phase. Modulation of the temperature and ligand concentration led to the observation of additional peaks, which can be attributed to $Rb_4PbBr_6$ phase, potentially synthesized as an energetically favorable by-product (cyan bars in **Figure 4.5**). These measurements evidence of $Rb^+$ presence in the films.

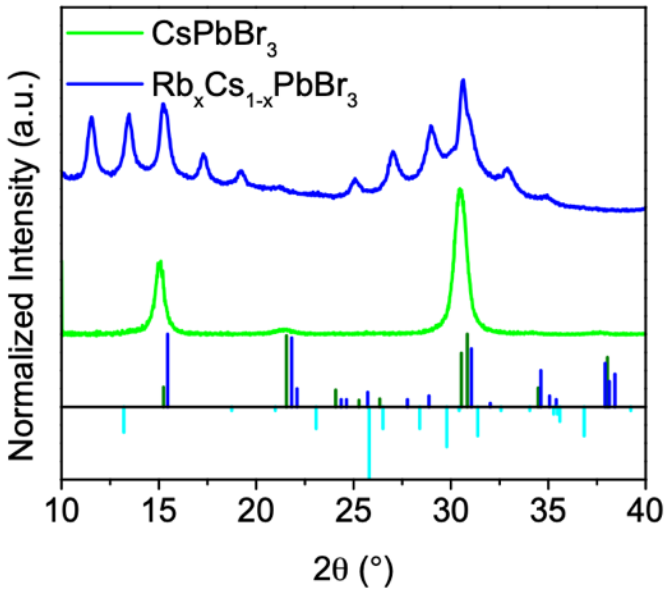


**Figure 4.5:** X-ray diffraction measurements of cubic $CsPbBr_3$ NCs (green curve) and nanoplates of $Rb_xCs_{1-x}PbBr_3$ nanoplates (blue curve). Deep-blue, green and cyan bars underneath the raw spectra correspond to peaks of $RbPbBr_3$ (PDF 00-028-0924), $CsPbBr_3$ (PDF 00-018-0364), and $Rb_4PbBr_6$ (PDF 00-025-0724) as obtained from the ICDD database.

To determine the colloidal species synthesized, we carried out transmission electron microscopy (TEM). The images in **Figure 4.6** indicate that nanocubes were observed at higher reaction temperatures and particularly at an equal OA:OLA ratio, whereas the nanoplates were the dominant species at lower reaction temperatures and at a 2:1 OA:OLA ratio. The lateral dimensions of these systems agree with previously reported PQDs of similar compositions.[28,52,60] Energy Dispersive X-ray measurements (**Appendix B1 Figure 2**) of these particles highlighted the presence of Rb only in samples which implemented the dual cation approach.

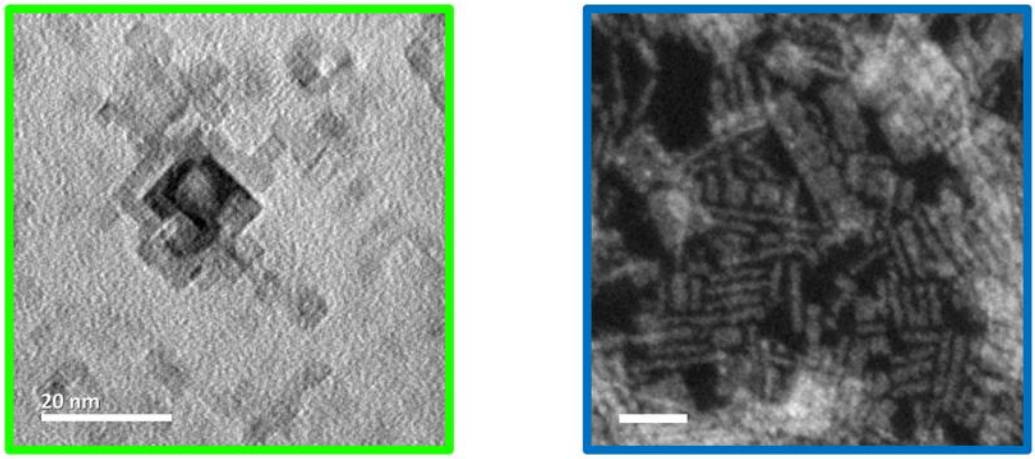


**Figure 4.6:** TEM images of synthesized $Rb_xCs_{1-x}PbBr_3$ nanocubes (left, green outline) and STEM dark-field image of $Rb_xCs_{1-x}PbBr_3$ nanoplates (right image, blue outline) with inset scale bars of 20 nm.

Motivated by the successful blue-emitting optoelectronic properties and the tunability of the system, we fabricated LEDs. The LED architecture can be summarized as a stacked set of layers consisting of: indium tin oxide (ITO)/ PEDOT:PSS/ poly-TPD/ perovskite QDs/ TPBi (60 nm) / LiF (1 nm)/ Al (150 nm) and displayed in **Figure 4.7**.

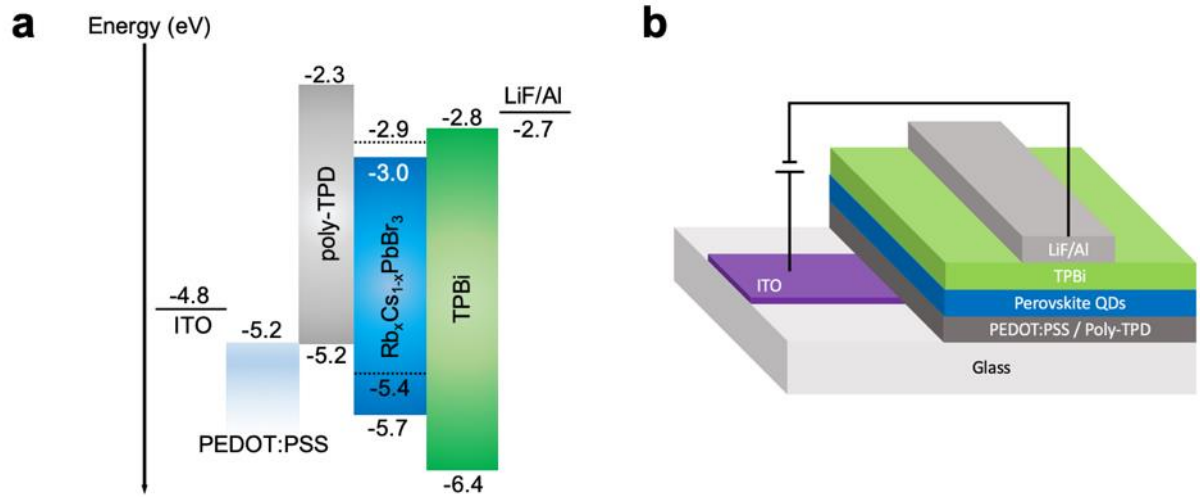


**Figure 4.7:** (a) Device band diagram consisting of all the layers and their respective energy levels. (b) Device architecture.

## 4.5 Tunable and Spectrally Stable Light-Emitting Diodes

As noted in the previous chapter, achieving stable blue electroluminescence has been rarely seen in mixed anion approaches. Reports have shown that $Cl^-$ is well known to introduce vacancies and cause trap formation within the perovskite QDs, resulting in considerable red-shifts of the EL peak.[60,72,73] By contrast, the mixed cation approach retains a pure bromine crystal structure, and this improves PL and EL stability as demonstrated by the lack of a shift in the EL peak across the blue (from 464 nm to 490 nm, **Figure 4.8**) under increased voltage bias. At the time of publication, this was the first set of Rb-doped perovskite QD LEDs that demonstrated high colour-purity (**Figure 4.9**).[52]

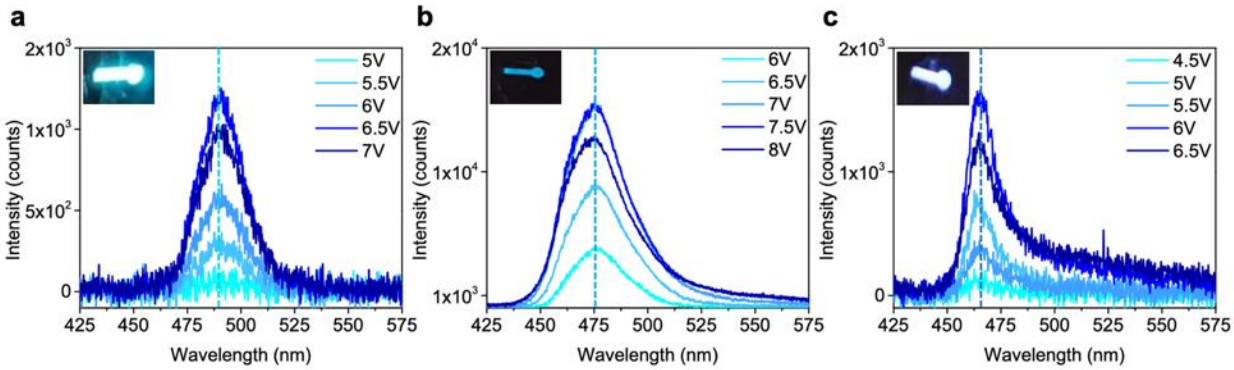


**Figure 4.8:** Electroluminescence spectra of $Rb_xCs_{1-x}PbBr_3$ light-emitting diodes (PeLEDs) exhibiting stabilized peaks at a) 490 nm (sky-blue), b) 475 nm (blue), and c) 464 nm (deep-blue) emitting devices for various operating voltages. Inset photographs are of EL devices under operating conditions for the various wavelengths.

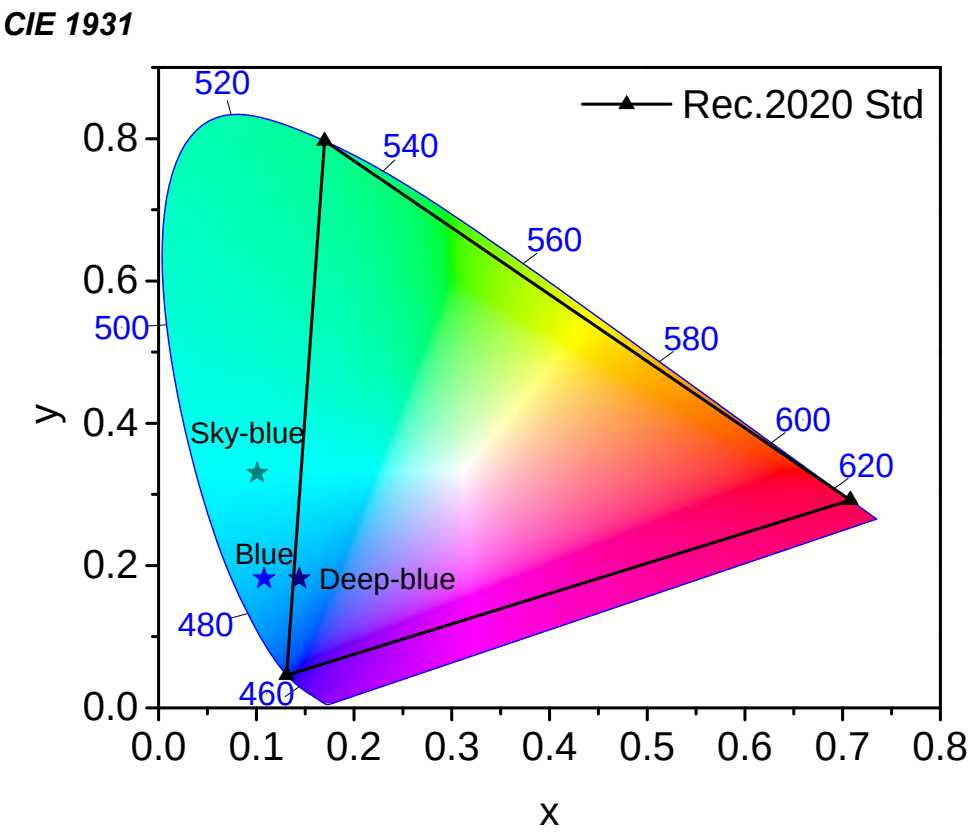


**Figure 4.9:** EL Spectra CIE coordinates as calculated by the formulas, plotted with respect to the Rec.2020 colour standards.

I found that, by optimizing the purification and fabrication procedure, I was able to obtain sky-blue and deep-blue $Rb_xCs_{1-x}PbBr_3$ PeLEDs which exhibited low turn-on voltages (< 4V) and a luminance greater than a pre-set practical minimum threshold luminance of 10 cd $m^{-2}$, particularly 186 cd $m^{-2}$ and 71 cd $m^{-2}$, respectively **(Figure 4.10a-b)**. The best device performance is summarized in **Table** 4.3 .

Table 4.3: Best $Rb_xCs_{1-x}PbBr_3$ PeLED performance.

| **Device** | **Peak $\lambda_{EL}$ (FWHM) [nm]** | **Peak Luminance [cd $m^{-2}$]** | **Peak EQE [%]** | **Luminance (@ $EQE_{peak}$) [cd $m^{-2}$]** |
|---|---|---|---|---|
| Sky-blue | 490 (22) | 186 | 0.87 | 93 @ 0.75% |
| Deep-blue | 464 (18) | 71 | 0.11 | 29 @ 0.11% |

I also found that the $Rb_xCs_{1-x}PbBr_3$ PeLEDs showed a much higher luminance at their most efficient point of operation – the maximum external quantum efficiency **(Figure 4.10c)**. In particular, the sky-blue and deep-blue devices displayed a peak luminance at the maximum EQE of 93 cd $m^{-2}$ at 0.75% and 29 cd $m^{-2}$ at 0.11%, respectively. These values were an order of magnitude higher relative to all previously reported PQD related candidates **(Figure 4.10d)**.[52,56,70] However, it should be noted that the low absolute EQE values in the deep-blue devices were attributed to the decrease in the PLQY of the materials in film as an increase in the purification steps reduced surface passivation and introduced surface defects. These defects act as traps and offer non-radiative recombination pathways for the charge carriers to pursue. One common technique to address this has been QD surface passivation, but in combination with interfacial losses within the device structure may further improve device performance.[27,52,71,74–76]

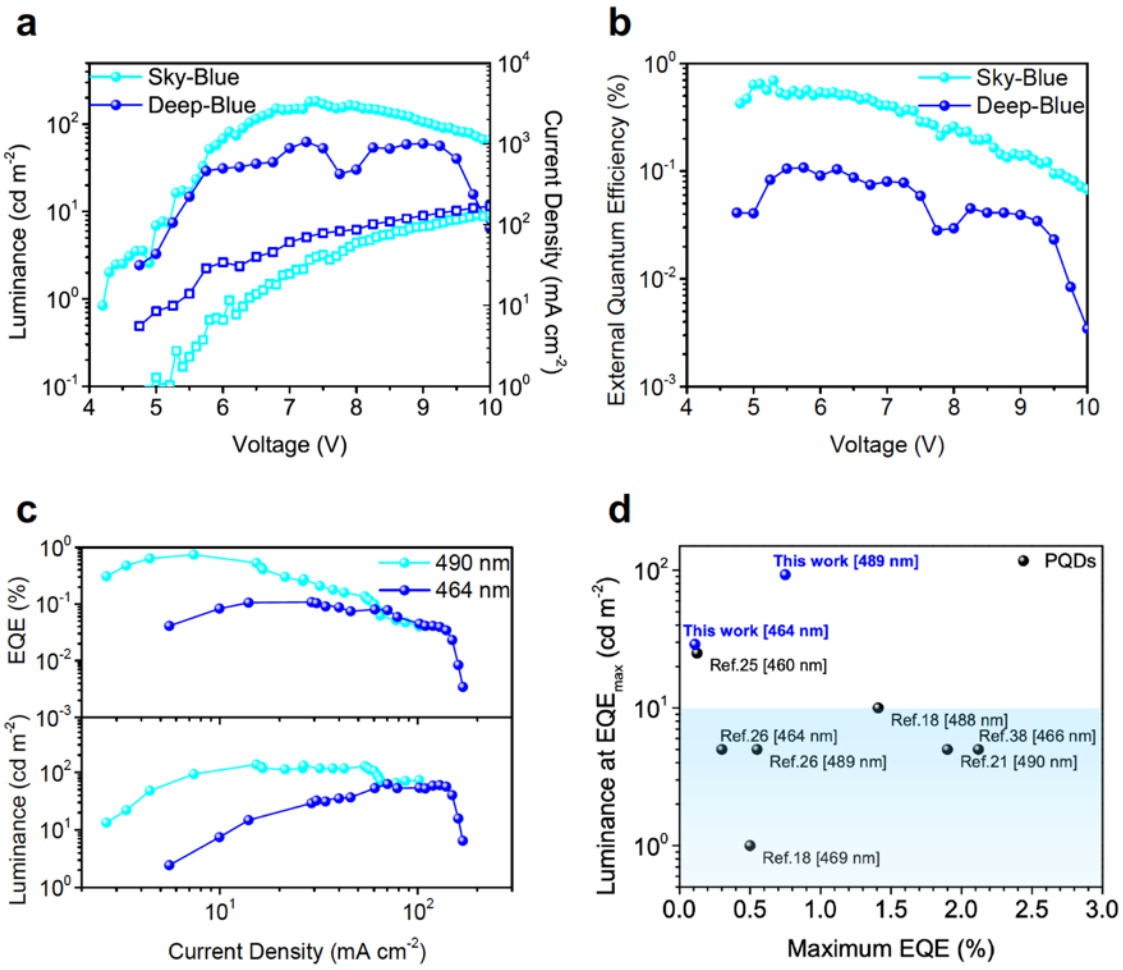


**Figure 4.10:** PeLEDs fabricated from $Rb_xCs_{1-x}PbBr_3$ QDs. (a) Current density (J) and luminance (L), (b) external quantum efficiency (all reported EQE values here are reported with at least 10 cd $m^{-2}$) device performances of sky-blue (cyan line) and deep-blue (blue line) as a function of applied bias. (c) Devices which exhibited the largest luminance at their peak EQEs (Table 4.3**)** summarizes the performance values). (d) Comparison of reported perovskite quantum dot device luminance at maximum EQEs [at peak wavelength]. A horizontal line at 10 cd $m^{-2}$ segments the data to indicate the importance of luminance at the reported maximum EQEs and highlights the improved device performance of $Rb_xCs_{1-x}PbBr_3$ devices.

## 4.6 Summary

In this chapter, I designed a mixed-cation chemical synthesis strategy for $Rb_xCs_{1-x}PbBr_3$ QDs. This led to tunable, narrow linewidths; and stable (thermally and under operating conditions) light-emitting materials. This approach addresses the poor spectral stability commonly observed in typical mixed-anion strategies since halide segregation. I characterized the colloidal solutions for their optical and structural properties, verifying the successful incorporation of $Rb^+$: the main mechanism resulting in the improved optoelectronic properties. I then fabricated the first $Rb_xCs_{1-x}PbBr_3$ QD LEDs to be reported and obtained stable spectral performance throughout the blue spectrum. The approach offers an avenue towards the design and development of practical and spectrally stable perovskite systems.

# 5 Improving Spectral Stability in Perovskite LEDs

Based on: Ma, D.[†], **Todorović, P.[†],** Meshkat, S., Saidaminov, M. I., Wang, Y. K., Chen, B., ... & Sargent, E. H. (2020). Chloride Insertion–Immobilization Enables Bright, Narrowband, and Stable Blue-Emitting Perovskite Diodes. *Journal of the American Chemical Society*, *142*(11), 5126-5134.

Modulating the dimensionality in perovskite nanostructures offers an additional route for a tunable system. In this chapter I examine the design of quasi-2D perovskites (consisting of quantum wells) as candidates for blue emission.

Controlling the formation of particular quantum wells in these reduced dimensional systems has been challenging. I investigated post-synthesis molecular treatment of these nanostructures to modify the optoelectronic properties. I observed that organophosphoryl chlorides such as diphenylphopshinic chloride (DPPOCl) induced particular reaction kinetics, yielding films with narrow phase distributions. Precise and limited phase distributions improved the quantum yield, inhibited efficient charge funneling and narrowed the emission spectra – a combination required for practical light-emitting applications. I hypothesized the reaction mechanism and performed the appropriate characterizations to support the hypothesis responsible for the observed optoelectronic properties. Based on these results, devices were fabricated to highlight the benefit of the post-synthetic treatment towards producing simultaneous record high luminance and stable blue perovskite LEDs.

This work was conducted in collaboration with postdoctoral fellow Dr. Dongxin Ma, with whom I share first co-authorship. I proposed the reaction mechanisms, led the optical (TA) and structural characterization (XRD, XPS), data analysis, visualizations and materials design. Dr. Dongxin Ma fabricated all thin-films, devices and led the device performance measurements. Other co-authors contributed in experimental guidance, additional characterization methods, computational studies (DFT calcuations) and overall discussions of results.

## 5.1 Introduction

In the previous chapter I discussed the first strategy utilized to obtain deep blue emission and address the spectral instability issue of typical materials. In this chapter I discuss an alternative method which relies on tailoring reduced dimensional perovskites geometry as opposed to tuning the elemental composition.[45]

Reduced dimensional perovskites (RDPs) are classified as a quasi-2D structure – a hybrid of a two and three-dimensional (2D and 3D) system whereby an organic ligand generates well defined and spatially confined quantum wells with particular emission wavelengths.[77–79] Reduced dimensional perovskites have garnered significant interest as promising materials for light-emitting applications owing to their high PLQY and ease of manufacturing.[30,45,80–82]

Today, the fabrication of RDPs leads to the formation of multiple quantum wells having varying degrees of confinement, and thus varying emission spectra.[57,83–85] The distribution of quantum wells is influenced by the processing conditions and precursor concentrations. The distribution of thicknesses of quantum wells leads to a variation in the energy levels throughout the RDP solid. This leads to energy gradients among the phases: a cascade that has the potential to exhibit transfer of excitons among the variously-confined inclusions.

When energy transfer is efficient (transfer occurs prior to radiative recombination), then emission can occur from the smallest-gap/longest-wavelength members of the population.[83] Controlling the quantum well thickness distribution has the potential to allow improved engineering of this charge funneling, and to narrow the emission spectra and increate quantum yield, all relevant to light-emitting applications.

I sought therefore to investigate how organochloride ligands introduced via post-synthesis transformed the reduced dimensional perovskite nanostructures. I led the structural and optical characterization of the typical $PEA_2Cs_{1.6}MA_{0.4}Pb_3Br_{10}$ perovskite material system and investigated the dynamic treatment procedure. I found that organophosphoryl chlorides such as diphenylphopshinic chloride (DPPOCl) induced reaction kinetics, yielding films with narrow phase distributions and emission profiles. I explored how the post-treatment modification resulted in well passivated films at various concentrations while simultaneously introducing chlorine into the perovskite crystal. This led to a tunable system which exhibited a blue-shift in emission. I specifically conducted X-ray diffraction (XRD) measurements to determine how the perovskite

crystal structure was modified via the chloride insertion-immobilization strategy. In addition, I studied the perovskite films using ultrafast transient absorption (TA) spectroscopy to investigate the photophysical properties of the films which revealed improved thermal and spectral stabilities. To support the proposed mechanism, I analyzed the elemental compositions via X-ray photoelectron spectroscopy (XPS) and reported the variation throughout the film by etching methods. The combination of these characterizations was necessary to develop insight of organic phosphide molecules and their role in stabilizing reduced-perovskite nanostructures, reducing the edge states and enabling blue emission. The experimental data confirmed the originally proposed mechanism and complements the computational results.

Based on the observations, I sought to take advantage of improved photophysical and structural properties and apply them in light-emitting applications. DPPOCl treated LEDs, displayed reproducible record luminance greater than 5000 cd $m^{-2}$ at a wavelength of 489 nm, and stable operating half-life of 51 minutes at a luminance of 1500 cd $m^{-2}$. Further optimization resulted in tuning the perovskites towards deeper blues with external quantum efficiencies of 5.2% at 479 nm and half-life of 90 minutes at a practical 100 cd $m^{-2}$ with no shift in the electroluminescence peak in operation. These devices displayed record performance and stability at the time of the publication.

## 5.2 Post-Synthesis Ligand Treatment Overview

Initially, this project was developed as a continuing study of the degradation and passivation schemes in reduced dimensional perovskites. It was well established that in these quasi-2D systems, degradation in performance and stability under photoexcitation and electrical injection was largely attributed to the presence of edge states.[86,87] These edge states form by the reactivity between the intercalating amine group with moisture and oxygen resulting in non-radiative pathways for the charge carriers to funnel to. This in turn is detrimental to obtaining efficient emission, and especially true for large bandgap materials (i.e. blue).[88] Previous reports have indicated that successful edge passivation can be achieved by utilizing organophosphoryl molecules such as triphenylphosphine oxide (TPPO) during film fabrication to reduce these edge states and lead to enhanced optoelectronic properties.[51] Previous reports have indicated that vacancies in the perovskite crystals induced halide migration under an applied electric field.[89] However, stabilized blue emission while reducing the moisture related degradation remained to be a challenge.

I sought therefore to investigate how similar organic phosphide species can be introduced in a post-treatment step to yield the aforementioned properties and obtain the desired edge passivation in blue. I focused on the general $PEA_2Cs_{1.6}MA_{0.4}Pb_3Br_{10}$ perovskite system which has shown promise as a highly efficient green emitting material.[47] Rather than tuning the optical properties via compositional engineering through chlorine-doped precursors, I postulated a dynamic treatment which would be implemented as a secondary film application step as shown in **Figure 5.1**. I theorized the dynamic treatment to serve in dual purpose: (a) utilize the trace water (from the remaining solvent and precursor solution) to passivate the crystal edges and (b) blue-shift the emission spectra. This required an intermediate thin-film step, whereby I posited that an organic chloride dissolved in antisolvent would help introduce $Cl^-$ in-situ in the perovskite grains, thereby leading to a blue-shift in emission and act as a passivating ligand (**Figure 5.2**). Discussions with colleagues and inspired by previous research studies we suggested the following set of molecules[51]:

i. Diphenylphosphinic chloride (DPPOCl);
ii. Phenylphosphonic dichloride ($PPOCl_2$);
iii. Benzenesulfonyl chloride ($PSO_2Cl$);
iv. Benzoyl chloride (PCOCl).

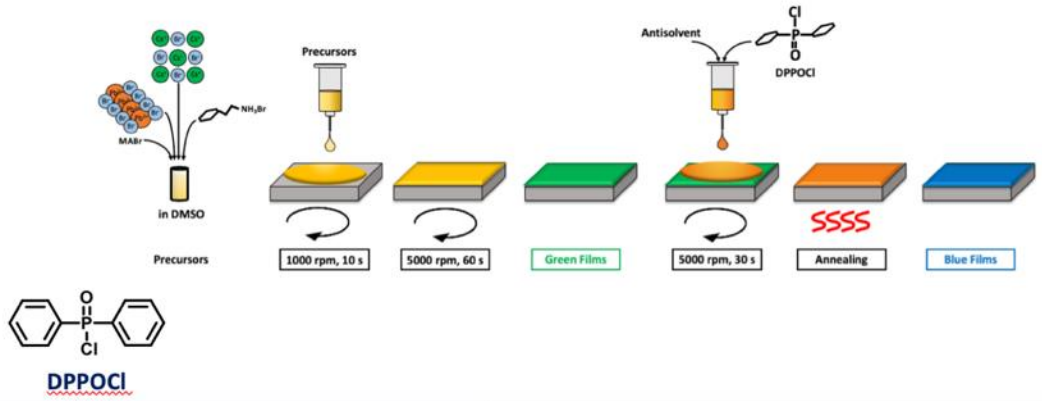


**Figure 5.1**: Postulated Phosphyryl Chloride Dynamic Treatment Process of Film-Fabrication (Second step, anti-solvent and ligand addition to form blue emitting perovskites)

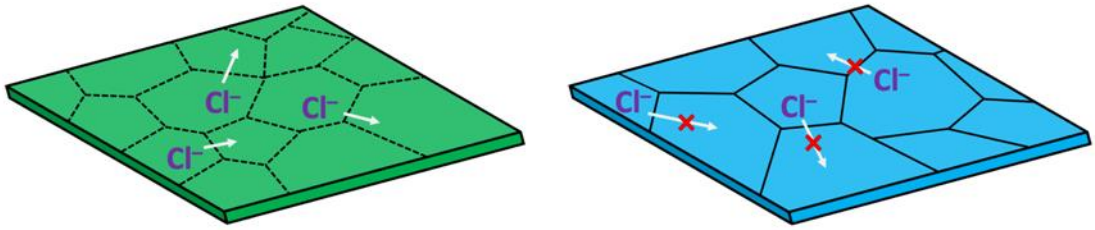


**Figure 5.2**: Imagined scenario of the perfect passivation scheme of the perovskite thin-films, inhibiting ion migration and resulting in stable, narrow blue emitters

To assess candidates, Density Functional Theory (DFT) calculations were carried out by my computational co-authors to establish the reactivity of the proposed molecules with trace water. It was found that DPPOCl in particular had the potential to release $Cl^-$ when interacting with trace water forming an intermediate diphenylphosphinic acid (DPPOOH) and $Cl^-$ ion (**Appendix B.2 – Table 1)**. DPPOOH would then form hydrogen bonds with the halogen ion (O-H···Cl and O-H···Br), passivating surface halide vacancies and preventing halide segregation. As a result, it was appropriate to name this mechanism as a dynamic chloride insertion-immobilization strategy. In contrast, this was not observed for the remaining candidates $PSO_2Cl$ and PCOCl. Therefore, this narrowed the focus of the post-synthesis strategy with DPPOCl as the main molecule of study. The reaction mechanism can be summarized in **Figure 5.3** below which highlights the difference in the typical chloride doping strategy and the proposed chloride insertion-immobilization mechanism through DPPOCl treatment.

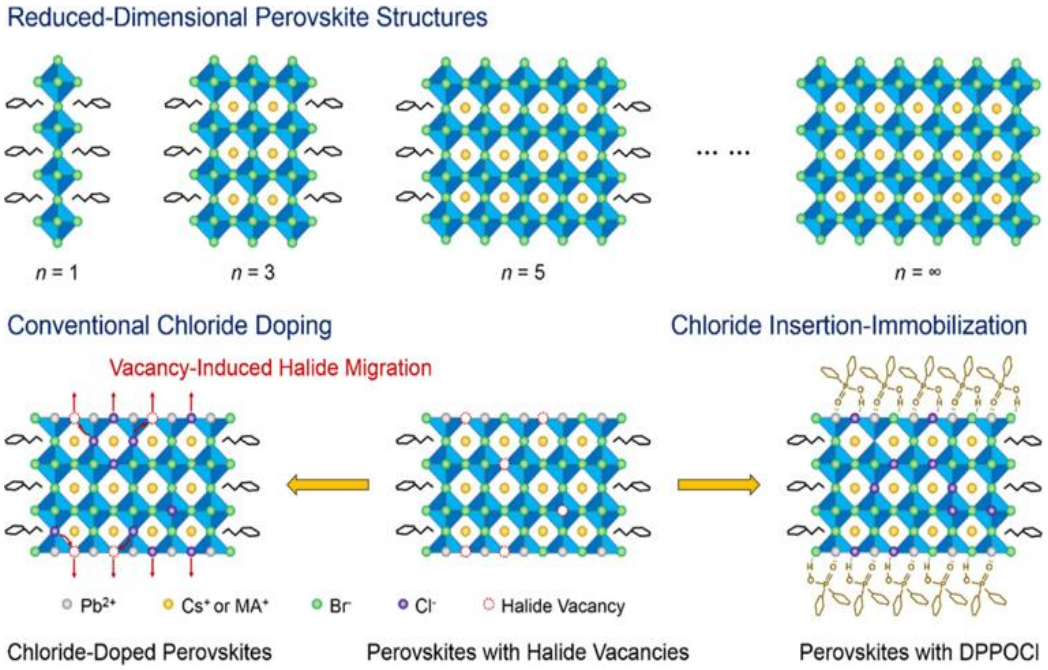


**Figure 5.3**: Perovskite structures and mechanism. In conventional chloride-doped perovskites, halide vacancies enable severe $Cl^-$ migration; while in perovskites treated with DPPOCl, $Cl^-$ is inserted and immobilized in the perovskite flake.

Motivated by the computational results, we fabricated films of $PEA_2Cs_{1.6}MA_{0.4}Pb_3Br_{10}$ (experimental details in Appendix A2) with DPPOCl treatment as described (with varying concentrations of 10, 20 and 30 mg/mL) and in the conventional chloride precursor method. The initial set of measurements of nuclear magnetic resonance spectroscopy confirmed the reactivity between trace water and DPPOCl as hinted by the resulting peaks observed. To date, the most widely implemented approach for blue emission in quasi-2D perovskites was introducing a mixture of $PbBr_2$ and $PbCl_2$ in the starting precursor solutions.[57,90,91] I refer to this as conventional chloride doping. I reasoned that a fair comparison would entail the conventional chloride-doped perovskite system as the standard control to evaluate the DPPOCl strategy. Thus, further characterizations were required to develop greater insight of the treatment procedure.

## 5.3 Optical Properties

The optical properties of the aforementioned thin-films were the first set of characterization. The absorption (**Figure 5.4a**) and photoluminescence (**Figure 5.4b**) peaks indicated that films treated with DPPOCl (solid line) led to a blue-shift towards shorter wavelengths, PLQYs exceeding 50% and longer radiative lifetimes with increasing concentration relative to the base $PEA_2Cs_{1.6}MA_{0.4}Pb_3Br_{10}$. The blue-shift was also present in the control group (*x = 1, 2, 3,* dashed line) but these films exhibited lower PLQYs and shorter lifetimes (**Figure 5.4c**). PL stability was monitored in ambient conditions and it was found that under continuous excitation (**Figure 5.4d**), DPPOCl treated perovskites demonstrated an improved ability to maintain their initial intensity as time progressed. As with previous studies, this suggested that the molecular ligands indeed helped provide an effect method for surface passivation as the observed rate of PL intensity decay decreased with increasing DPPOCl treatment (maximal stability observed in the case 30 mg/mL DPPOCl, **Figure 5.4d** solid blue line).[92,93]

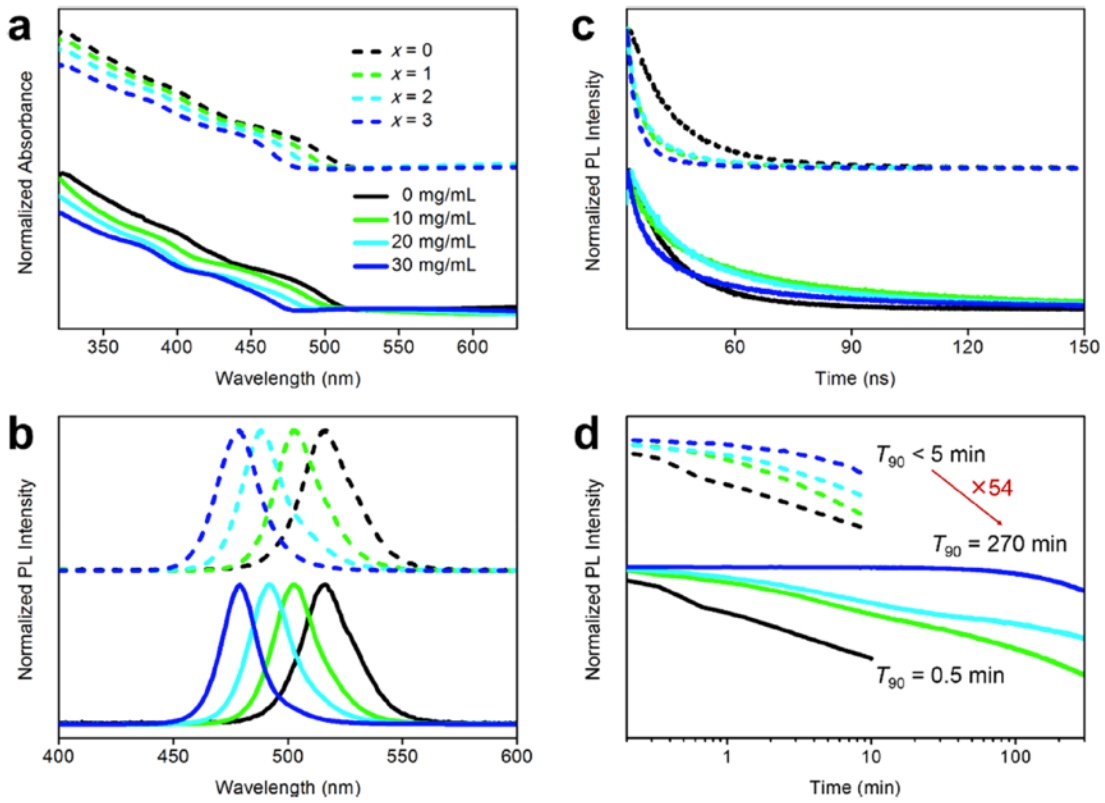


**Figure 5.4**: Optical properties. a, Absorption spectra. b, PL spectra. c, PL radiative lifetime. d, PL stability of control $PEA_2Cs_{1.6}MA_{0.4}Pb_3Br_{10-x}Cl_x$ ($x$ = 1, 2, or 3) (dashed line) and perovskites treated with 10, 20, or 30 mg/mL DPPOCl (solid line).

The photostability of the films was measured at an average optical excitation density of 180 mW/cm$^2$ (**Appendix A.2** for further details). These results suggest that, in terms of power density, DPPOCl treated films have the potential to be more robust under applied voltage bias. Total energy dissipated within the films will also be a function of the thickness of the active layer, and the molecular passivation obtained through DPPOCl is expected to enhance this further relative to prior Cl-doped perovskites.

As noted previously, reduced dimensional perovskite thin films typically exhibit poor PLQYs unless coupled with an effective method to passivate the surface defects. The dynamic perovskite treatment protocol addressed this limitation, showing that DPPOCl passivated the surface defects, blue-shifted the PL peaks, improved PLQY and PL stability under constant fluence. Inspired by these photophysical observations, I then sought to investigate the films from a structural level.

## 5.4 Nanostructure Characterization

X-ray diffraction (XRD) was used to characterize the nanostructures formed in the perovskite crystal. The base undoped $PEA_2Cs_{1.6}MA_{0.4}Pb_3Br_{10}$ system displayed the bulk perovskite signals occurring at 2θ angles of 15.7° and 30.9°, corresponding to the set of 110 and 220 crystal planes respectively. **Figure 5.5** highlights that both control and DPPOCl treated samples the exhibit a shift in bulk perovskite peaks towards larger values.

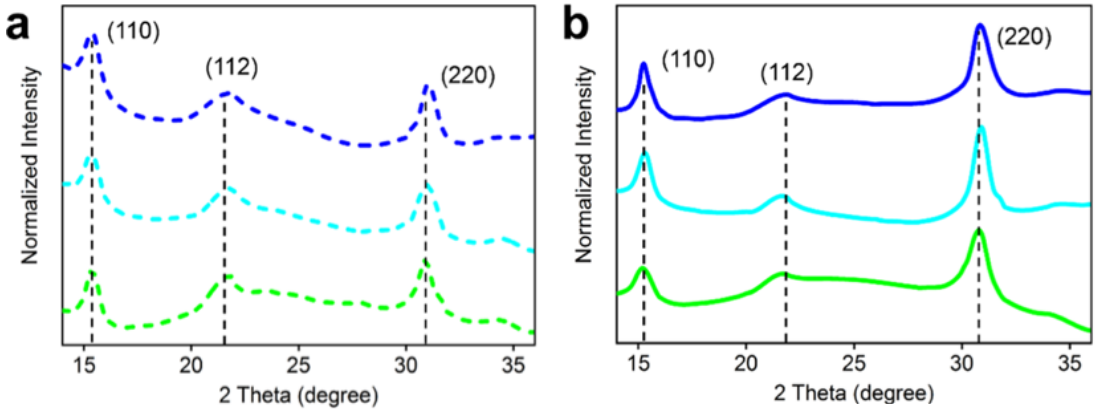


**Figure 5.5**: Structural XRD spectra a, control $PEA_2Cs_{1.6}MA_{0.4}Pb_3Br_{10-x}Cl_x$ (x = 1, 2, or 3) and b, perovskites treated with 10, 20, or 30 mg/mL DPPOCl.

This is expected and consistent with previous reports.[94] The angular shifts increase with increased concentrations of chloride treatment, indicating greater doping and successful incorporation into the crystal lattice. This verifies the observations of the blue-shifted PL peaks as a consequence of enlargement of the bandgap. The XRD peaks reveal a similar width, suggesting that the crystal sizes were of the same order despite the varying concentrations. Using the Scherrer equation (**Equation 5.1**), I calculated the crystallite size of the samples which were roughly 8-10 nm:

$$\tau = \frac{K\lambda}{\beta cos\theta} \tag{5.1}$$

where $\tau$ is the mean size of the crystalline domains, which may be smaller or equal to the grain size; $K$ is a dimensionless shape factor, with a value close to unity; $\lambda$ is the wavelength of the x-ray source; $\beta$ is the line broadening at half the maximum intensity, after subtracting the instrumental line broadening, in radians; and $\theta$ is the Bragg angle.

Similar peak shifts were observed in perovskites treated with $PPOCl_2$, but not with $PSO_2Cl$ or PCOCl (**Appendix B.2 - Figure 1)**. Therefore, it further supported our hypothesis that DPPOCl was the most optimal choice of passivating ligand to develop the insertion-immobilization chloride mechanism. To gain further insight of the perovskite nanostructures, I proceeded with ultrafast transient absorption (TA) measurements.

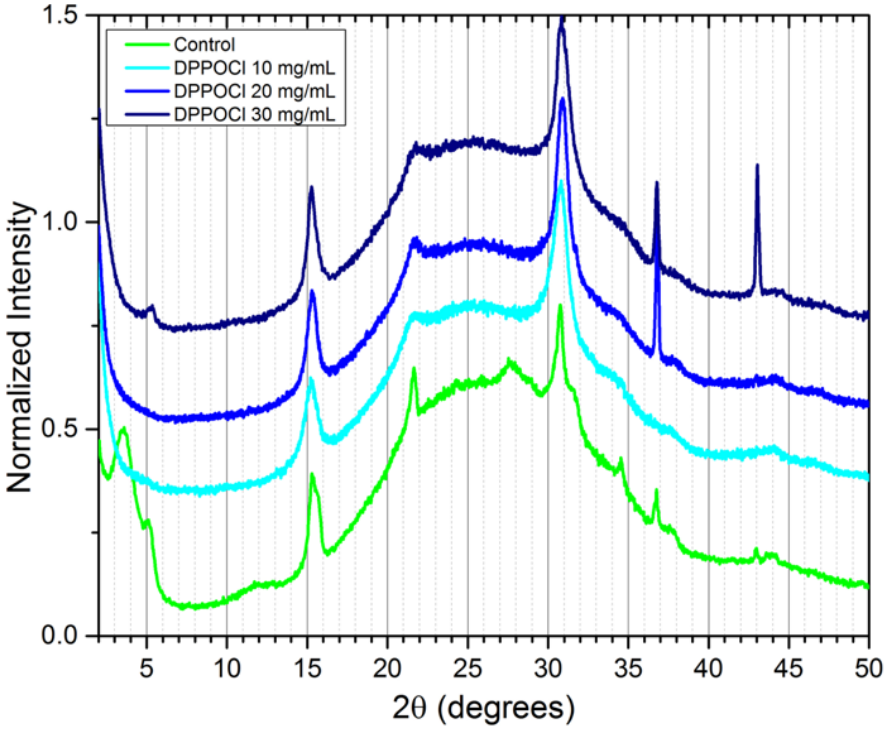


**Figure 5.6:** Detailed XRD Spectra of DPPOCl to elucidate the increase of the angle towards larger values with increasing concentration shifts.

## 5.5 Film Kinetics and Film Formation

Transient absorption measurements allowed me to determine how the quasi-2D film was altered after the ligand passivation technique and in particular examine the size distribution of the perovskite grains. TA spectra of the initial base perovskite $PEA_2Cs_{1.6}MA_{0.4}Pb_3Br_{10}$, five photobleach valleys at 404, 433, 464, and 509 nm were observed (**Figure 5.7**) and are plotted against the bulk 3D perovskite of composition $Cs_{0.8}MA_{0.2}PbBr_3$ which displays one single bulk absorption. The valleys in $PEA_2Cs_{1.6}MA_{0.4}Pb_3Br_{10}$ correspond to the $n$ = 1, 3, 5, and 5+ phases in the perovskite structure. The formation of the varied phases in RDPs is seen in $PEA_2Cs_{1.6}MA_{0.4}Pb_3Br_{10}$. As the thickness $n$ of the perovskite layers increases, the energy difference decreases and the photobleach valleys overlap one another. The largest energy

differences exist in the case of low *n* phases (namely n=1, 3, 5) and at shorter wavelengths. Narrow emission linewidths can be realized by funneling charge carriers via efficient exciton transfer from the large to small bandgap phases; or via the precise tuning of the energy landscape.

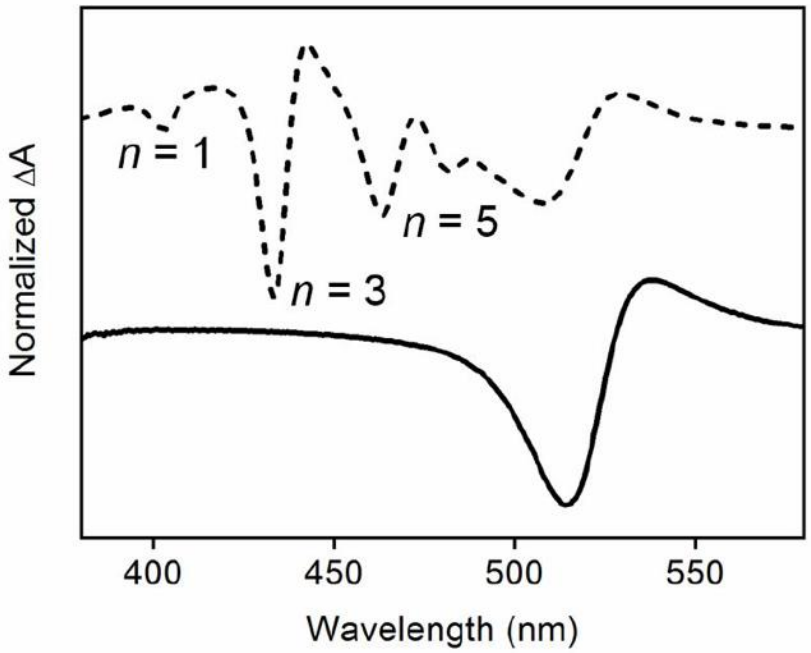


**Figure 5.7**: TA spectra of 3D perovskite $Cs_{0.8}MA_{0.2}PbBr_3$ (solid line) and quasi-2D perovskites $PEA_2Cs_{1.6}MA_{0.4}Pb_3Br_{10}$ (dashed line) reported at 10 ps delay following photoexcitation pulse.

In the case of control $PEA_2Cs_{1.6}MA_{0.4}Pb_3Br_{10-x}Cl_x$ ($x$ = 1, 2, or 3), the photobleach valleys blue-shifted with an increase in the chloride:bromide ratio (**Figure 5.8a**) agreeing with the structural XRD measurements. However, for perovskites treated through dynamic DPPOCl addition, the TA spectra showed a significant difference in the suppression of lower *n*-phases (**Figure 5.8b**) as seen by the absolute removal in their respective intensities (reduction in $n$ = 1, 3, 5). These films exhibited a dominant proportion of $n$ = 5+ phases, which improved the recombination rate through effective passivation and a reduction in the phase dispersity relative to the lower phases. Previous reports have observed similar phenomena – supporting these findings.[26]

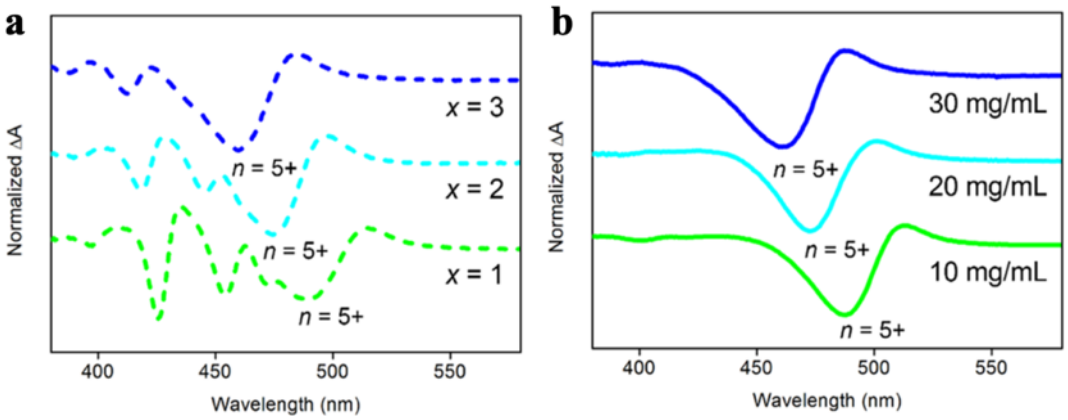


**Figure 5.8**: TA spectra of control $PEA_2Cs_{1.6}MA_{0.4}Pb_3Br_{10-x}Cl_x$ ($x$ = 1, 2, or 3) and perovskites treated with 10, 20, or 30 mg/mL DPPOCl (measured at 10 ps).

Perovskites treated with $PPOCl_2$ showed similar TA spectra, but $PSO_2Cl$ or PCOCl portrayed much different results at a concentration of 10 mg/mL (**Figure 5.9, Appendix B.2 - Figure 2**). The results highlight that DPPOCl was the optimal choice from the family of phosphoryl chlorides which enables precise control of the crystallization process, decreasing the coexistence multiple reduced-dimensional perovskite domains, and thus enabling narrowed emission linewidths of 20 nm. Lastly, I show that decay dependent TA studies in (**Appendix B.2 - Figure 3**) highlight that both the control and DPPOCl treated perovskites the amplitude of photobleach valleys slowly increase with delay time, yet the peak positions remain constant indicating film stability.

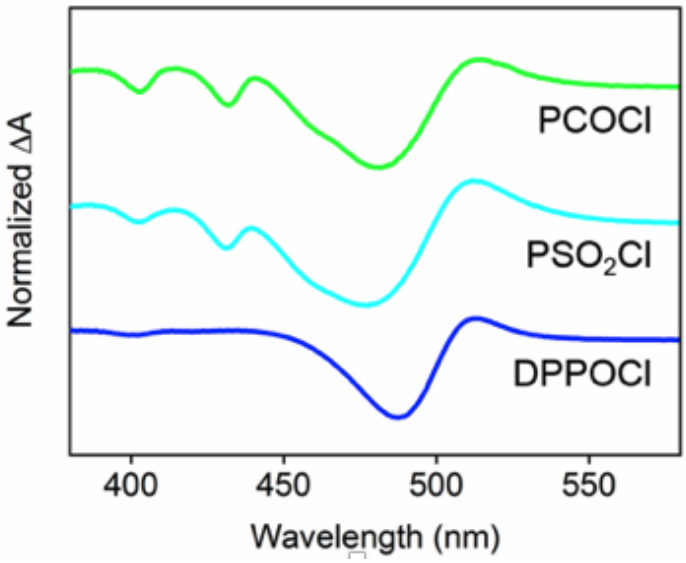


**Figure 5.9**: TA spectra of perovskites $PEA_2Cs_{1.6}MA_{0.4}Pb_3Br_{10}$ treated with 10 mg/mL DPPOCl, $PSO_2Cl$, or PCOCl (measured at 10 ps).

## 5.6 Chemical Composition

I then proceeded to investigate the chemical composition through X-ray photoelectron spectroscopy (XPS). I confirmed the presence of Cl in both the perovskite treated films with DPPOCl and in the control $PEA_2Cs_{1.6}MA_{0.4}Pb_3Br_{10-x}Cl_x$ ($x$ = 1, 2 or 3) on the surface, confirming the Cl-doping and supporting the blue-shifted optical properties. Since XPS is a surface sensitive technique, I reasoned that measurements throughout the depth of the film would improve insight of the treatment process and understand the chemical composition as a function of film thickness. Cross-sectional SEM results indicated that the thickness of the perovskite film in the fabricated devices was roughly 60 nm (**Appendix B.2 - Figure 4**).

I utilized $Ar^+$ ion-etching to obtain 3 separate depth levels: the surface, ~15 nm, and ~30 nm depth. After the etching was completed, XPS measurements were performed at the two depth levels and the chemical compositions were obtained by integration of the resulting spectra using the instrument software. The two films presented different elemental distributions throughout the depth of the film. As the etch depth increased, the Cl ratio increased for all perovskite films treated with DPPOCl, whereas the opposite trend was observed for the control films (**Table 5.1**). These results showed an improved chlorine doping mechanism throughout the overall film, attributing to the overall stability and optoelectronic performance enhancement. In addition, XPS measurements

revealed that P was more present on the surface of the perovskites treated by DPPOCl (and non-existent in the control), implying a passivated film surface. However, phosphorus is an extremely light element and therefore it was problematic to quantify the exact ratio of P in the perovskites treated with DPPOCl, especially post-etching in ultra-high vacuum conditions. For that reason, it has been omitted from the table below.

**Table 5.1**: XPS Measurements and the resulting compositions of Cl/Br as determined by integrating the spectra

| | **Surface** | | **In the film (30 nm deep)** | |
|---|---|---|---|---|
| **Perovskite Formula** | Ratio of Cl (%) | Ratio of Br (%) | Ratio of Cl (%) | Ratio of Br (%) |
| **$PEA_2Cs_{1.6}MA_{0.4}PbBr_9Cl$ ($x$ = 1)** | 12.6 | 87.4 | 11.4 | 88.6 |
| **$PEA_2Cs_{1.6}MA_{0.4}PbBr_8Cl_2$ ($x$ = 2)** | 22.7 | 77.3 | 18.7 | 81.3 |
| **$PEA_2Cs_{1.6}MA_{0.4}PbBr_7Cl_3$ ($x$ = 3)** | 30.3 | 69.7 | 26.8 | 73.2 |
| **$PEA_2Cs_{1.6}MA_{0.4}PbBr_{10}$ 10 mg/mL DPPOCl** | 9.7 | 90.3 | 10.3 | 89.7 |
| **$PEA_2Cs_{1.6}MA_{0.4}PbBr_{10}$ 20 mg/mL DPPOCl** | 10.9 | 89.1 | 17.8 | 82.2 |
| **$PEA_2Cs_{1.6}MA_{0.4}PbBr_{10}$ 30 mg/mL DPPOCl** | 15.3 | 84.7 | 23.1 | 76.9 |

## 5.7 Device Performance

I then sought to take advantage of the improved photostability while simultaneously enlarging the bandgap and realizing blue reduced dimensional perovskites through the insertion-immobilization strategy. LEDs were fabricated based on the architecture described below in **Figure 5.10**. The LED follows the following stack: indium tin oxide (ITO)/ PEDOT: PSS: PFI

(~200 nm)/ Perovskite (~60 nm)/ TPBi (30 nm)/ LiF (1 nm)/ Al. The choice of materials was chosen based on previous literature and their particular energy levels described below[51,77]:

1. PEDOT: PSS: PFI served as the exciton-buffering and hole-injection layer;
2. TPBi was the electron-transport layer;
3. Lithium fluoride (LiF) as the electron-injection layer;
4. Al as the cathode.

The energy band diagram of the resulting perovskites is also displayed in the right panel, determined by UPS measurements, which enabled the efficient and charge-balanced injection.

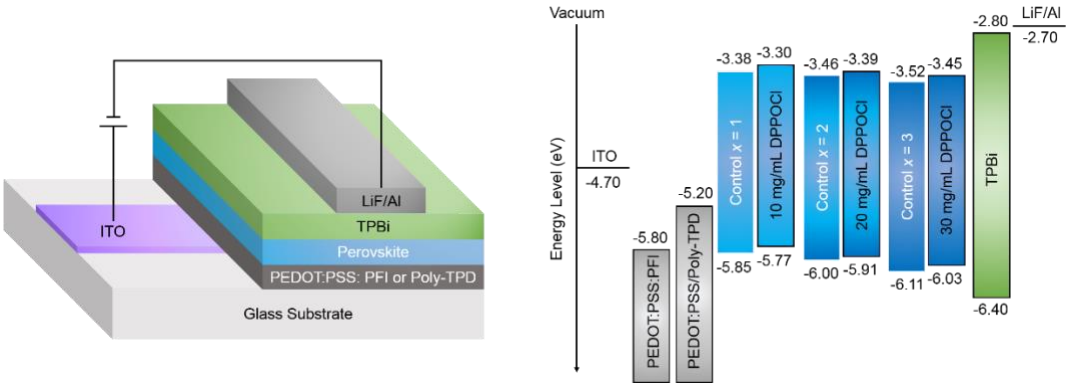


**Figure 5.10**: Perovskite LED architecture and energy band diagram based on literature and UPS measurements.

Device performance is summarized in **Figure 5.11** and **Table 5.2**. Perovskite LEDs which leverage the DPPOCl treatment exhibited higher current densities and EL performance relative to control $PEA_2Cs_{1.6}MA_{0.4}Pb_3Br_{10-x}Cl_x$ ($x$ = 1, 2, or 3). This I attribute to enhanced conductivity through the improved phase purity. EQE and luminance increase with increasing DPPOCl concentration which directly correlates with the PLQYs of the corresponding films. Perovskites treated with 10 mg/ mL DPPOCl showed a highest EQE of 7.4% and luminance of 32,320 cd/m$^2$ at 510 nm. Perovskites treated with 20 mg/mL DPPOCl exhibited a peak EQE of 3.5% and luminance of 15,290 cd/m$^2$ at 499 nm. Perovskites treated with 30 mg/mL DPPOCl operated with a maximum EQE of 1.3% and luminance of 5,141 cd/m$^2$ at 489 nm achieving the highest luminance among reported perovskite LEDs in the blue region (**Table 5.2**).[95]

I also observed that LEDs which applied DPPOCl treatment enabled narrow FWHM below 20 nm through the reduction in the phase dispersity, providing a tighter size distribution and enhanced the colour stability by preventing ion migration under operation. The conventional chloride doped perovskite $PEA_2Cs_{1.6}MA_{0.4}Pb_3Br_{10-x}Cl_x$ ($x$ = 1, 2, or 3) displayed a clear shift in the EL spectra and change in the CIE coordinates. Specifically, a WSHM of 1.0, 3.4, and 5.9 nm, respectively was observed for the three concentrations in increasing order. On the other hand, perovskites treated with DPPOCl showed stable EL spectra with no observable wavelength shift (**Figure 5.12**).

The best-performing sky-blue LEDs treated with 30 mg/mL DPPOCl achieved an EQE of 5.2%, a narrow linewidth (FWHM of 18 nm) and stable (WSHM of zero) emission at 479 nm (**Figure 5.12**). The two measured half-lives were 5 min at an initial luminance of 468 cd/m$^2$ and 90 min at 100 cd/m$^2$, exceeding prior blue perovskite LEDs (**Table 5.2**).[95]

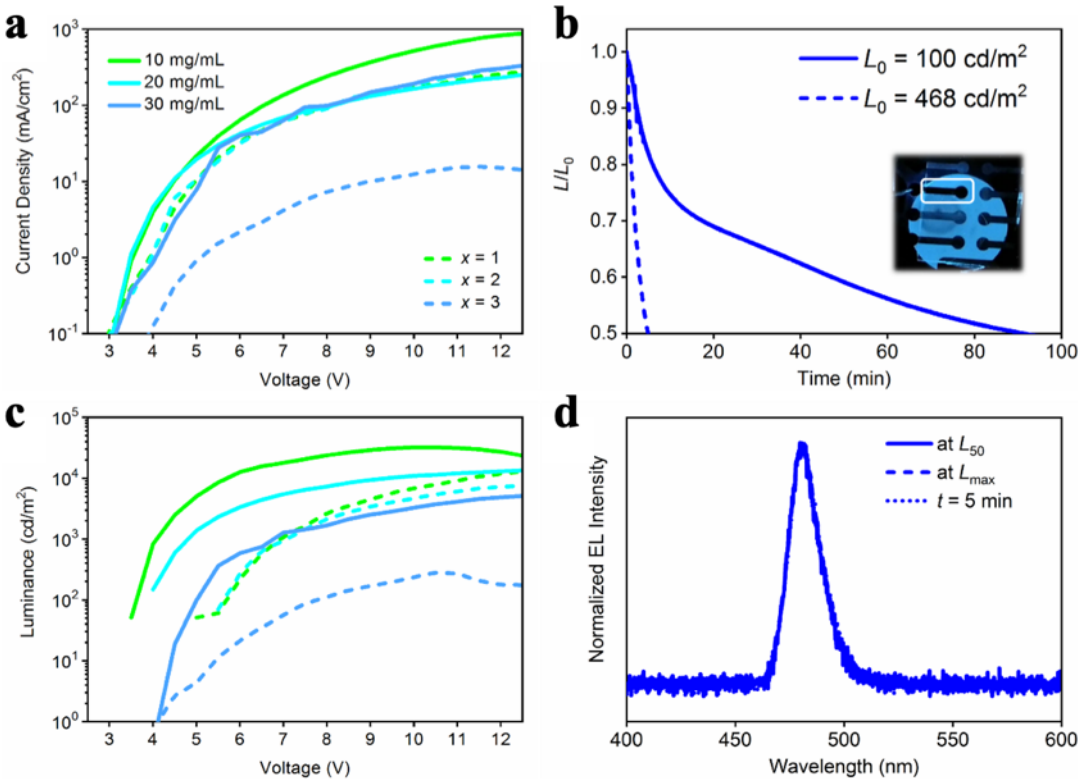


**Figure 5.11**: LED performance a. Current density versus voltage curves. **c,** Luminance versus voltage curves of LEDs based on control $PEA_2Cs_{1.6}MA_{0.4}Pb_3Br_{10-x}Cl_x$ (x = 1, 2, or 3, dashed lines) and perovskites treated with DPPOCl (10, 20, or 30 mg/mL, solid lines). **b,** Operating lifetime of the sky-blue LEDs under different constant driving currents, and the inset shows a photograph of the operating device at 468 cd/m$^2$. **d,** EL spectra at half of the maximum luminance (234 cd/m$^2$), maximum luminance (468 cd/m$^2$) and during the lifetime measurement at t = 5 min when the luminance dropped to the half.

**Table 5.2**: Performance of reported blue-emitting perovskite LEDs.

| Perovskite[Reference] | EQE $_{max}$ (%) | $L_{max}$ (cd/m$^2$) | $\lambda_{EL}$ (nm) | FWHM / WSHM (nm) | $T_{50}$ |
|---|---|---|---|---|---|
| $PEA_2PbBr_4$[96] | 0.04 | N. A. | 410 | 14 / - | N.A. |
| $PEA_2(Rb_{0.4}Cs_{0.6})_2Pb_3Br_{10}$[97] | 1.5 | 854 | 490 (at $L_{50}$)<br>490 (at $L_{max}$) | 30 / 0 | 2 min at 126 cd/m$^2$ |
| $(IPA)(PEA)_2(Cs/MA)_{1.5}Pb_{2.5}Br_{9.5}$[53] | 1.5 | 2,480 | 490 (at $L_{50}$)<br>490 (at $L_{max}$) | 28 / 0 | 0.5 min at 210 cd/m$^2$ |
| $(PBA)_{1.1}FA_{0.3}Cs_{0.7}PbBr_{4.1}$[98] | 9.5 | 700 | 483 (at $L_{50}$)<br>483 (at $L_{max}$) | 26 / 0 | 4 min at 100 cd/m$^2$ |
| $(BA/Cs)PbBr_{1.26}Cl_{1.74}$[55] | 2.4 | 962 | 465 (at $L_{50}$)<br>472 (at $L_{max}$) | 23 / 7 | 1 min at 500 cd/m$^2$ |
| $(BA/Cs)PbBr_{2.52}Cl_{0.48}$[55] | 6.2 | 3,340 | 487 (at $L_{50}$)<br>487 (at $L_{max}$) | 25 / 0 | 10 min at 800 cd/m$^2$ |
| $(PEA/Cs)PbBr_{2.1}Cl_{0.9}$[99] | 5.7 | 3,780 | 480 (at $L_{50}$)<br>488 (at $L_{max}$) | 21 / 8 | 10 min at 1,500 cd/m$^2$ |
| $PEA_2Cs_{1.6}MA_{0.4}Pb_3Br_{10}$ treated with DPPOCl | 1.3 | 5,141 | 489 (at $L_{50}$)<br>489 (at $L_{max}$) | 18 / 0 | 51 min at 1,500 cd/m$^2$ |
| | 5.2 | 468 | 479 (at $L_{50}$)<br>479 (at $L_{max}$) | 18 / 0 | 90 min at 100 cd/m$^2$ |

* $EQE_{max}$, maximum external quantum efficiency; $L_{max}$, maximum luminance; $L_{50}$, half of the maximum luminance; $\lambda_{EL}$, EL wavelength; FWHM, Full-Width at Half Maximum; WSHM, Wavelength Shift between Half and Maximum luminance; $T_{50}$, half-life

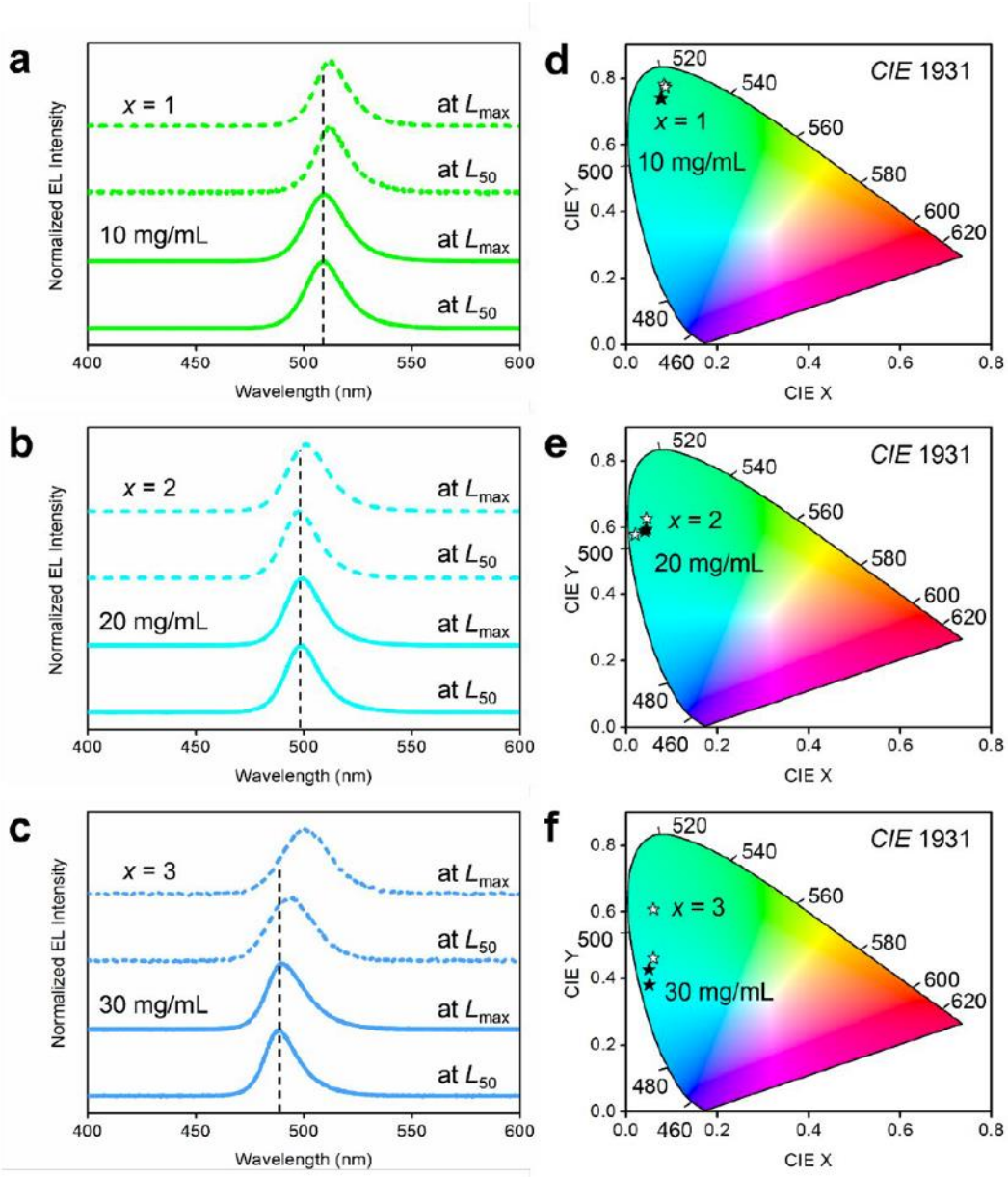


**Figure 5.12**: Colour purity and spectral stability. a-c, EL spectra. d-f, CIE values of the green-blue, ice-blue, and sky-blue LEDs based on control $PEA_2Cs_{1.6}MA_{0.4}Pb_3Br_{10-x}Cl_x$ (x = 1, 2, or 3, dashed lines and hollow stars) and perovskites treated with DPPOCl (10, 20 and 30 mg/mL, solid lines and stars).

## 5.8 Summary

In this chapter, I reported the design of a dynamic chlorine doping and molecular passivation treatment system based on introducing DPPOCl post-film fabrication that resulted in precise control of the quantum well size distribution in a quasi-2D perovskite system. The chloride insertion-immobilization mechanism passivated the edges of the resulting films and introduced chlorine into the crystal domains thereby shifting the emission towards the blue. This strategy led to the narrow emission profiles and improved spectral stability in devices. Relative to prior chloride-based precursor doping strategies, the treatment method resulted in a non-existent WSHM shift of the emission spectra under operation – leading to improved life-time stabilities. The proposed mechanism was supported by computational density-functional-theory calculations, and experimental evidence verified the reaction pathways which led to the observed improvements.

This dynamic treatment approach enabled bright and colour-pure blue-emitting perovskites. It addresses the problem of spectral stability caused by ion migration in prior reports. In the next chapter, I focus on combining computational efforts to help guide and efficiently discover next-generation semiconductors for light-emitting applications.

# 6 Semiconductor Discovery Guided via Machine Learning

Based on: Choubisa, H.†, **Todorović, P.†,** Pina, J.M., Parmar, D.H., Li, Z., Voznyy, O., Tamblyn, I., Sargent, E.H., 2021. Interpretable discovery of new semiconductors with machine learning. *Submitted to JACS.*

*Ab initio* methods such as density functional theory (DFT) are used to explore materials computationally. DFT is used by the research community to predict and estimate electronic properties of materials and to examine which crystal structures are most favoured energetically. However, accurate calculations are computationally expensive even for modern day supercomputer clusters. In this Chapter, I advanced a graph-based neural network architecture by designing specific input data structures to predict the optoelectronic bandgaps of inorganic materials with high accuracies. I utilized a DFT dataset containing hybrid-functional calculations of the bandgap – an approach known to improve accuracy, though to come at the cost of being computationally demanding – to train the algorithm. Inspired by biology, an evolutionary algorithm is implemented which levers the machine-learned models to explore materials space efficiently and rapidly. Chemical insights are derived from the proposed candidates and design rules are established which help guide experimental research efforts. Based on the interpretable rules which I discovered, I proposed a set of candidate UV semiconducting materials. These were realized experimentally and studied for their photophysical properties. These findings illustrate the unification of computational machine learning and experiment for AI-guided materials discovery. The overall system was named DARWIN: Deep Adaptive Regressive Weighted Intelligent Network.

This work was conducted in collaboration my fellow doctoral candidate Hitarth Choubisa whom I share first co-authorship. I designed, trained and optimized the deep learning models used to predict the optoelectronic properties, implemented the evolutionary algorithm, led the data visualization and statistical analysis of the computational and experimental results, and guided the experimentalists in synthesis procedures. Hitarth provided all DFT calculations and verifications, and he designed the DNNs responsible for classification and regression tasks on the structural and stability properties. Other co-authors carried out experimental characterization of the predicted materials including XRD, PL studies, and overall discussions of results.

## 6.1 Introduction

In the previous chapter I discuss the experimental strategies to design nanoscale perovskite materials for light-emitting applications. In this chapter, I focus on complementing and guiding the experimental discovery of materials via computational methods. A simplified diagram of the blended experimental-computational approach is illustrated in Error! Reference source not found..

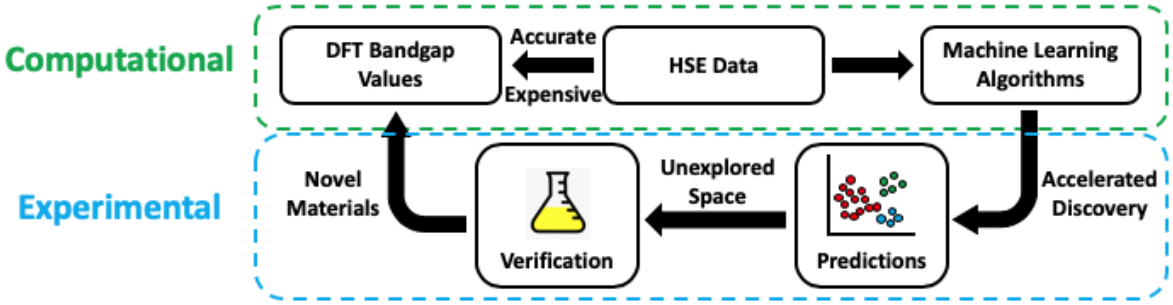


**Figure 6.1**: Machine-learning algorithm and the schematic of the experimental-computational bridge of predicted materials validation.

## 6.2 Deep Learning – Graph Neural Networks (GNNs)

The first constituent component of DARWIN is the DNNs used to predict the properties of interest. Graph Neural Networks (GNNs) are a type of DNN which use graphs as input. They have shown promise in ML predictions of materials due to their effectiveness in capturing non-arbitrary irregular structures such as that of molecules and crystals.[100,101] The crystal structures from the DFT dataset are represented as 2D graphs with structural information following the formulation of previous reports.[100–102] The crystals structures are formatted as undirected graphs *G:= {V, E}* which represent nodes (*n*) as atoms and edges connecting the corresponding atoms as bonds, respectively (**Figure 6.2**). Atomic features are denoted as $u_i$ and represent physical and chemical properties native to the atom at node *i* (refer to Appendix for an exhaustive list). Similarly, an edge feature vector labelled $e_{i,j}$ incorporates the reciprocal distance $d_e^{-1}$ between the connecting nearest neighbouring atoms *i* and *j* (**Figure 6.2**). The concept of convolution in this network helps encode local information from the neighbouring atomic elements, selected by implementing a cut-off radius of 8Å – ensuring that only the local environment is considered. I posited that the specific

reciprocal distance edge attribute would capture the strength of the relative atomic properties for the varied elements in the crystal system and scale them as accordingly. This concept arose from the physical intuition that many forces scale with the inverse of the distance (i.e., gravitational, electrostatic attraction, etc). This led to the model efficiently learning on a smaller but accurate dataset. The details of the graph encoding procedure and standard convolution implementation of models for supervised regression and classification tasks I include in **Appendix A3**.

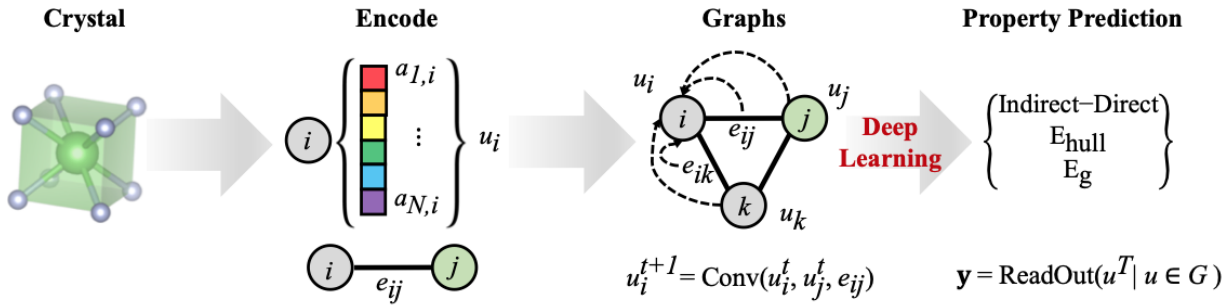


**Figure 6.2**: Mapping crystals to graph representations through encoding atomic information. Then the Graph Neural Networks are trained to predict the desired property – bandgaps, energies, and direct/indirect nature.

### 6.2.1 Predictive Graph Convolutional Neural Network Models – Bandgap

Many studies have implemented various convolutional operators with success[100,101,103,104], but here I use a complementary set of convolutional graph neural networks as the basis for the predictive ML models. I design a specific convolution operation for the bandgap regressor shown below. Each crystal graph is fed into the network as an input; wherein the convolutional layer is defined by the following order of operations: the maximum vector after concatenation ($\oplus$) of the current atoms feature vector ($u_i^t$), the product of each neighbouring ($\mathcal{N}(i)$) atomic feature vectors ($u_j^t$) with the corresponding edge features ($e_{ij}$) at each iteration $t$. The $\gamma^t$ represents the update function (typically defined by a multilayer perceptron (MLP) consisting of a non-linear activation function $g$) and weight tensors $W_s^t$ and $b^t$ which are learnt during the training steps for each convolutional layer.

$$u_i^{t+1} = \gamma^t \left[ \max_{j \in \mathcal{N}(i)} \left( u_i^t \oplus \left( u_j^t \cdot e_{ij} \right) \right) \right], \qquad \begin{matrix} \forall\, i, j \in G \\ \forall\, t \in \{1, \ldots, T\} \end{matrix} \tag{6.1}$$

$$u_i^{t+1} = g\left[\max_{j \in \mathcal{N}(i)} \left(u_i^t \oplus (u_j^t \cdot e_{ij})\right) W_s^t + b^t\right], \qquad \begin{matrix} \forall\, i,j \in G \\ \forall\, t \in \{1,\ldots,T\} \end{matrix} \tag{6.2}$$

An output value is obtained by pooling all of the hidden nodal features using the mean pooling function which results in the prediction of a bandgap value $\hat{y}_{bandgap}$.

$$\hat{y}_{bandgap} = \frac{1}{n}\sum_{i=1}^{n} u_i^T, \qquad \forall\, u \in G \tag{6.3}$$

To measure the accuracy of the ML models, I use the mean squared error as a cost/loss function. I seek to minimize the MSE during training which evaluates how well our predicted bandgap is with respect to the target values. I achieved this minimization by finding the optimal values for the weight and bias matrices in the corresponding convolutional layers.

$$MSE = \frac{1}{n}\sum_{i=1}^{n} (y_i - \hat{y}_i)^2, \qquad \forall\, i \in G \tag{6.4}$$

GCNN generates a global representation of the crystal structure from the chemical features representative of each element at a given node and edge feature that scales as the reciprocal distance between the atoms to reproduce the predictions of accurate ab initio calculations (**Figure 6.2**, see **Appendix A3** for details). I train the bandgap regressor (**Figure 6.3**) on a newly generated dataset of 1,800 samples calculated using the computationally expensive HSE functional, which is known to correlate well with experimental values.

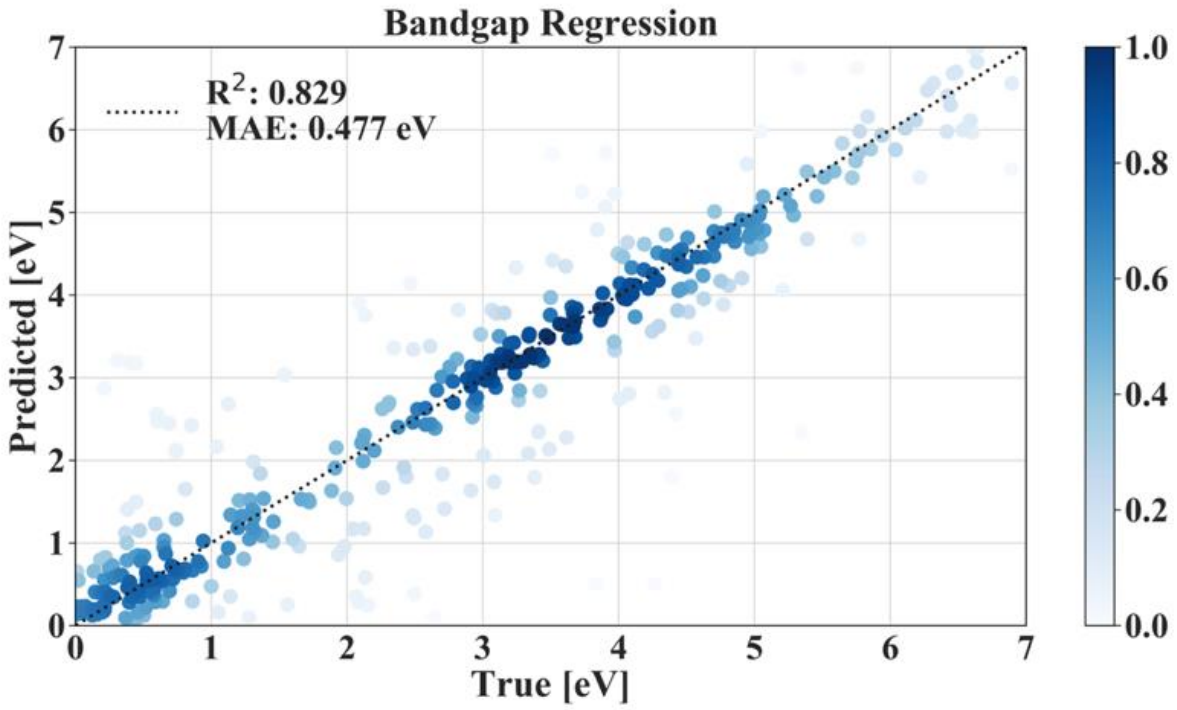


**Figure 6.3**: ML Bandgap Predictions vs. True (DFT) Predicted bandgap values on the validation data for the best performing and hyperparameter tuned bandgap regressor as previously mentioned. The resulting model predicts the true HSE bandgap value with a coefficient of determination of 0.829 and mean-absolute-error of 0.477 eV. This error is lower by 20% relative to current DFT errors for the bandgap calculations (MAE of DFT[105] ~ 0.6 eV).

I observed that a total of 4 convolutional layers and 2 fully connected dense layers were the most optimal choice of the network that led to accurate predictions of the bandgaps. The list of atomic features (**Appendix B3 – Table 1 and Table 2**) and the best performing set are reported in the **Appendix B3**. All features were normalized via standard ML procedures prior to the crystal graph generation to ensure comparable scalar magnitudes. Graphs were generated using the aforementioned process, enabling efficient and rapid batch training.

In training the model, hyperparameters are an additional set of variables which are model specific and can be modified to improve accuracy and accelerate training. Examples include the optimization methods, activation functions, learning rate and regularization parameter of the neural network. The optimal set is determined by training the model several times while varying the values and evaluating the final performance on a validation dataset. The set of hyperparameters that perform best are then selected and implemented on the "out-of-sample" test data to generate

an unbiased performance of the model. Here, the main choice of hyperparameters available to be optimized in the graph model include: the size of each convolutional layer, choice of activation function, pooling layer, learning rate and weight decay. I found that the most optimal hyperparameters were the following: the Adam optimizer, a rectifying linear unit activation function (ReLU), learning rate of 0.01, weight-decay of 0.0005, 4 convolutional layers (consisting of 64, 64, 32, 16 output channels).

Since $MAE_{DFT}$ ~0.6 eV[105] relative to experimental bandgaps, and error in the GNN is not systematic, it is expected that the ML predictions will be closer to experimental results as well. The previously optimized set of hyperparameters resulted in a mean-absolute-error of 0.48 eV on validation data after 3000 epochs of training on a set of roughly 1,800 crystals. I report the prediction comparison of the optimized ML model, DFT and experimental values of the bandgaps in **Figure 6.4**. Despite training on DFT values, ML predicted bandgaps show good agreement with measured values on a test set of experimentally confirmed compounds. The trained and optimized GCNN models predict HSE06 bandgaps with mean absolute errors (MAE) of 0.53 eV on test data. This implies that the model is quite accurate in predicting the optoelectronic properties of materials outside the training space, highlighting the ability to learn and generalize from the training set. Thus, the best out-of-sample model was chosen and used as one of the surrogate models for the implementation in the evolutionary algorithm.

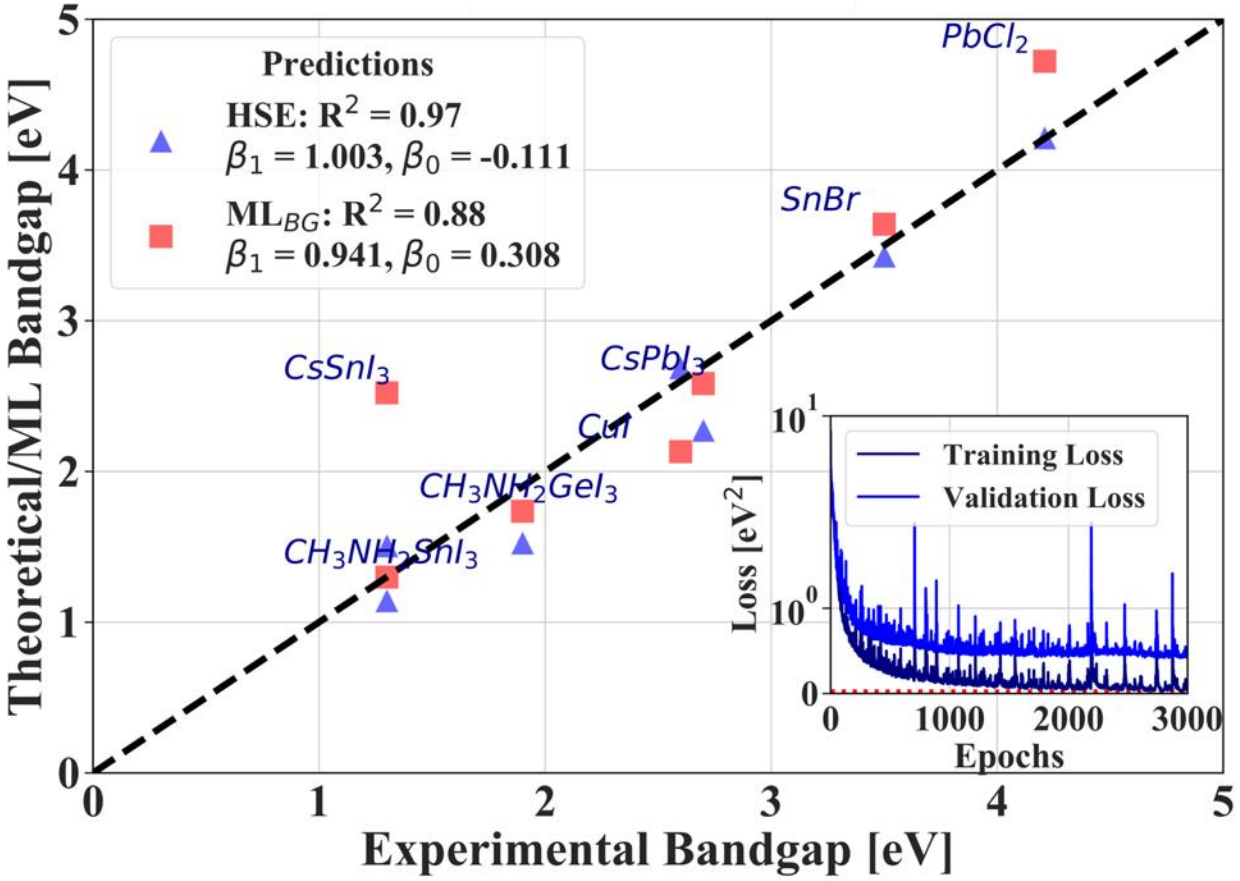


**Figure 6.4**: Performance of the ML model and HSE06 exchange-correlation functional calculated values in predicting experimental bandgaps (inset of training/validation loss curves). The legend includes the coefficient of determination and linear regression parameters as obtained by fitting a linear regression model between the true experimental value and the two various predictions methods (DFT vs. ML).

## 6.3 Evolutionary Algorithm

We then sought to leverage and utilize the optimized GCNNs as surrogate models and implement them in a learning-based (i.e. intelligent)[106,107] agent (evolutionary algorithm) to search through materials space. The evolutionary search process is divided into two components: (1) random generation of the initial candidates from all possible crystal structures, using compositions that satisfy the charge balance, and (2) an iterative update-evaluation step (**Appendix A3** for details) in which candidates are evaluated for fitness and ranked relative to one another based on chosen fitness score. The most intuitive and typical fitness function is the sum of the mean squared errors of the predicted bandgap, energy above hull, and direct-indirect nature relative to their desired values and then ranked accordingly. All candidate materials are ranked in descending order of fitness such that those having the highest error are ranked lowest. After the ranking and sorting, the bottom half is discarded, and the top half is replicated but with each corresponding structure receiving a mutation, thereby generating a new group of candidates. In our case, we substitute a random element of equivalent oxidation state from a set dictionary of elements available to maintain the charge neutrality of the structure. This procedure results in a new generation of potential solutions of the same initial size and referred to as mutation and the overall process is described in **Appendix A3**. In addition to mutation, crossover is another genetic operator which modifies the set of potential solutions at each iteration. However, crossover would take the top-ranked candidates and randomly select the atoms from this top selection and form arbitrary combinations of compositions which may or may not fundamentally coexist in the physical realm. In addition, crossover methods potentially proceed towards local-optima and a suboptimal solution as a result of the similarity among the top-ranked individuals – motivating the single mutation strategy and omitting crossover.[108] I found that mutations alone were enough to direct the search towards the optimal compositions of the large chemical space, confirmed by the decreasing loss as a function of increased iterations, or increasing set of species generations (**Figure 6.5**).

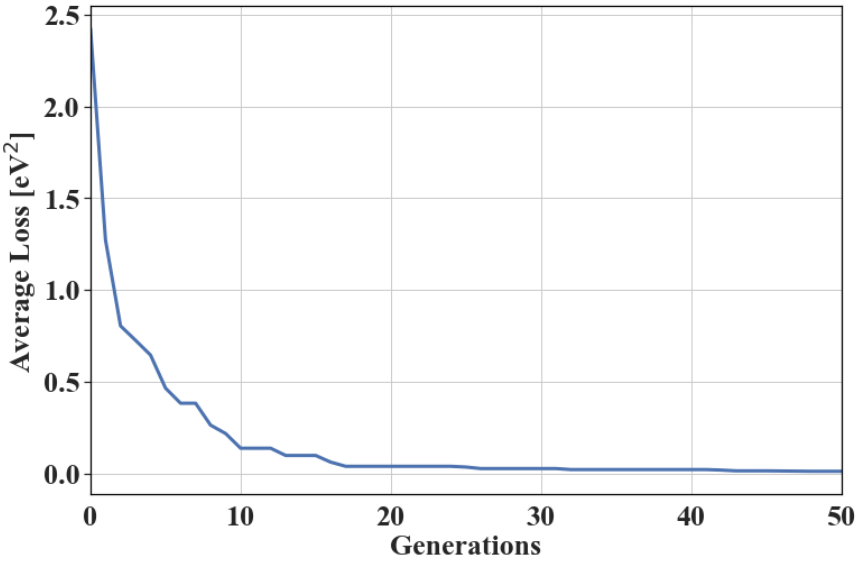


**Figure 6.5**: Average loss as a function of generations. Using random mutations alone, we achieve quick loss convergences for finding optimal bandgap and stable materials for a target bandgap. Result shown for finding stable, direct bandgap material with bandgap of 3.1 eV.

Evolutionary search was initialized with a set of randomly generated prototype structures spanning 220 space groups and 7 crystal systems synonymous with the original dataset. The search algorithm relies on the ML surrogate models to predict the properties of interest and evaluate the set of candidates for their fit as described previously. Although evolutionary search combined with a surrogate model can lead to promising compositions, it does not on its own provide intuitive understanding for the discovery of such materials. The last component of DARWIN enables interpretation[101,109]. The complete process is illustrated in **Figure 6.5**, describing each component.

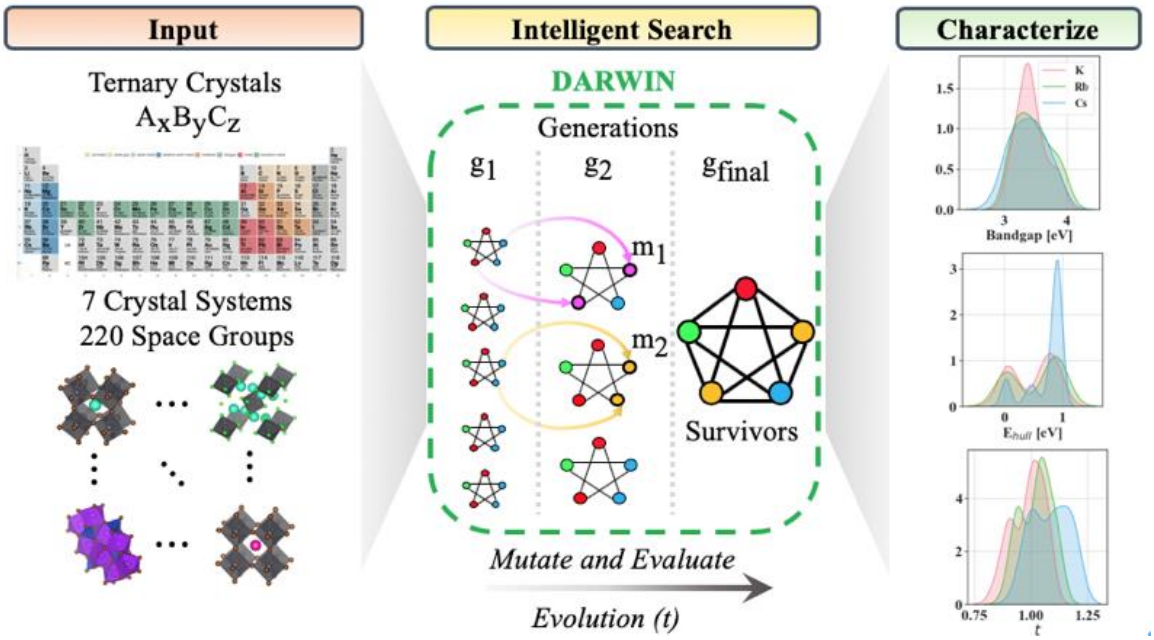


**Figure 6.6**: Evolutionary Search via surrogate models - DARWIN. Input. To enable search of compounds with non-rare elements, we limited DARWIN search by excluding Lanthanides, Actinides and rare transition elements. Crystals were generated using substitutions in prototype structures and spanned over 7 crystal systems and 220 space groups; Intelligent Search. DARWIN uses trained Graph Networks as surrogate models and mutations to find new candidates; Characterize. DARWIN enables the discovery of new compounds and uncovers new chemical trends via unsupervised learning and feature-based ML methods.

## 6.4 Materials Search

I proceed with applying DARWIN to search for stable and direct UV bandgap materials (3eV - 4eV), a relatively unexplored and vast chemical space[110,111]. I expand the list of predicted candidates by executing the materials search multiples times using different random initializations, such that a larger space is covered. The initialization provides a distinct set of optimized crystal structures for each iteration, which I aggregate together to form the overall set of predicted materials. It is important to note that several structures may appear repeatedly as the algorithm converged to the local minima given the initialization or mutations that arrived to the corresponding solutions. In these cases, the average target value was taken for every candidate composition. I observed that structures of the form: $ABX_4$, $ABX_3$ and $A_2BX_3$ typically exhibited

the lowest predicted energy above hull indicating high stability. Examples of the top-ranking stable materials include the following list: $Cs_2SnBr_4$, $Rb_2SnBr_4$, $Rb_2CrBr_4$, $CsScBr_4$, $KInBr_4$, and $K_2CuCl_3$. These results highlight the elemental diversification among the predictions which can be achieved in such an evolutionary computing approach.

DARWIN yields several promising UV structures from which I select ternary candidates with the A-site containing one of the common alkali metals {K, Rb, Cs} and the X-site be occupied one of the halogens {Cl, Br, I} for further analysis. This selection is implemented to enable ease of synthesis and due to limited precursor availability. To further assess the quality of the predictions, DFT bandgaps were calculated on the proposed set of candidates (**Table 6.1**). Evaluation of the mean absolute difference between the DARWIN bandgap and DFT-calculated bandgap of ternary crystal-based systems, suggests that those which contain Cu as a B-site cation exhibit high prediction accuracy. In the context of UV-bandgap materials, these findings illustrate high prediction precision for Cu-based systems positions them as the optimal choice of candidates to focus further analysis.

**Table 6.1**: DARWIN Predicted UV Materials and their ML Bandgaps with post-DFT HSE06 Verification Calculations.

| Predicted Structural Formula | Mean DARWIN Predicted Bandgap [eV] | HSE Bandgap [eV] | Absolute Difference [eV] | 2nd Element in Structure | Mean Absolute Difference [eV] |
|---|---|---|---|---|---|
| Cs2ZnCl4 | 3.49 | 3.45 | 0.04 | Zn | 0.96 |
| Rb2ZnCl4 | 4.06 | 3.41 | 0.64 | | |
| CsZnCl3 | 3.40 | 2.60 | 0.80 | | |
| SrZnBr4 | 3.19 | 1.20 | 1.99 | | |
| CsZnBr3 | 3.55 | 4.87 | 1.32 | | |
| Rb2CuCl3 | 3.80 | 3.50 | 0.30 | Cu | 0.19 |
| Cs2Cu1I3 | 3.52 | 3.77 | 0.25 | | |
| Rb2CuBr3 | 3.66 | 3.71 | 0.05 | | |
| CsCu2Br3 | 3.32 | 3.16 | 0.16 | | |
| K2CuCl3 | 3.66 | 3.54 | 0.12 | | |
| K2CuI3 | 3.63 | 3.82 | 0.19 | | |
| Rb2CuI3 | 3.69 | 3.45 | 0.24 | | |
| CsCu2Cl3 | 3.40 | 3.69 | 0.30 | | |
| RbCu2Cl3 | 3.31 | 3.47 | 0.16 | | |
| GaCuBr4 | 3.50 | 3.34 | 0.17 | | |
| ZnMg2Cl6 | 3.80 | 1.23 | 2.57 | Mg | 1.50 |
| CsMgBr3 | 3.53 | 4.65 | 1.12 | | |
| CaMgBr4 | 3.84 | 3.10 | 0.74 | | |
| ZrMg2Br4 | 3.30 | 1.30 | 2.00 | | |
| SrMgBr4 | 4.00 | 2.93 | 1.07 | | |

Although DARWIN can lead us to interesting compositions quickly, it fails to rationalise the discovery of such materials. Graph based deep learning models also lack interpretation which limit the ability to discover new science and uncover interesting patterns[101,109]. Therefore, it is imperative to find the chemical features or insights which are the descriptors responsible for the predicted results to help guide experiment.

## 6.5 Post-Prediction Analysis for Experimental Guidance

I performed a manual feature analysis of the promising candidates generated by the evolutionary search. I examined features beyond those included as input to the GNN and found that DARWIN reconfirmed known descriptors predictive of bandgap, such as the A-site cations and halide choice in typical perovskite-based crystals. These results showed how prediction stability trends match the empirical tolerance factor *t* - a known proxy for stable perovskite materials[112–114].

I used a pair plot to qualitatively examine the relationships and distributions of the DARWIN predicted bandgap and energy above hull with respect to the calculated tolerance factor and the electronegativity of the B-site. The analysis was extended as a function of the A-site cation, as indicated by the three different cations K, Rb, Cs (pink, green, blue in **Figure 6.7**). Off-diagonal components of the Figure illustrate the relationship between the various parameters, whereas the diagonals show the parameter distribution of the predicted compounds dataset. This enabled me to establish general trends among the predictions, such as the increased peak bandgap of compounds which have K occupy the A-site. It is also observed that as the cation radii increases (K to Cs), the calculated tolerance factor increases as expected – tolerance factor and A-site size are linearly related. Surprisingly, I found a strong positive pair-wise relationship between the electronegativity of the B-site and the tolerance factor, suggesting that a particular range of electronegativity values potentially lead to stable materials. A similar parameter analysis was performed but as a function of the halide ion, supporting the qualitative trends found in stability of the predicted compounds (i.e., tolerance factor linearly related with anion radii, **Figure 6.8**). The trends I found related to B-site electronegativity led me to extend the feature analysis and investigate the difference in electronegativity (EN) of the B-site (the second most metallic element in the composition) and X-site (most electronegative anion), which I denote as $\Delta_{X\text{-}B}$.

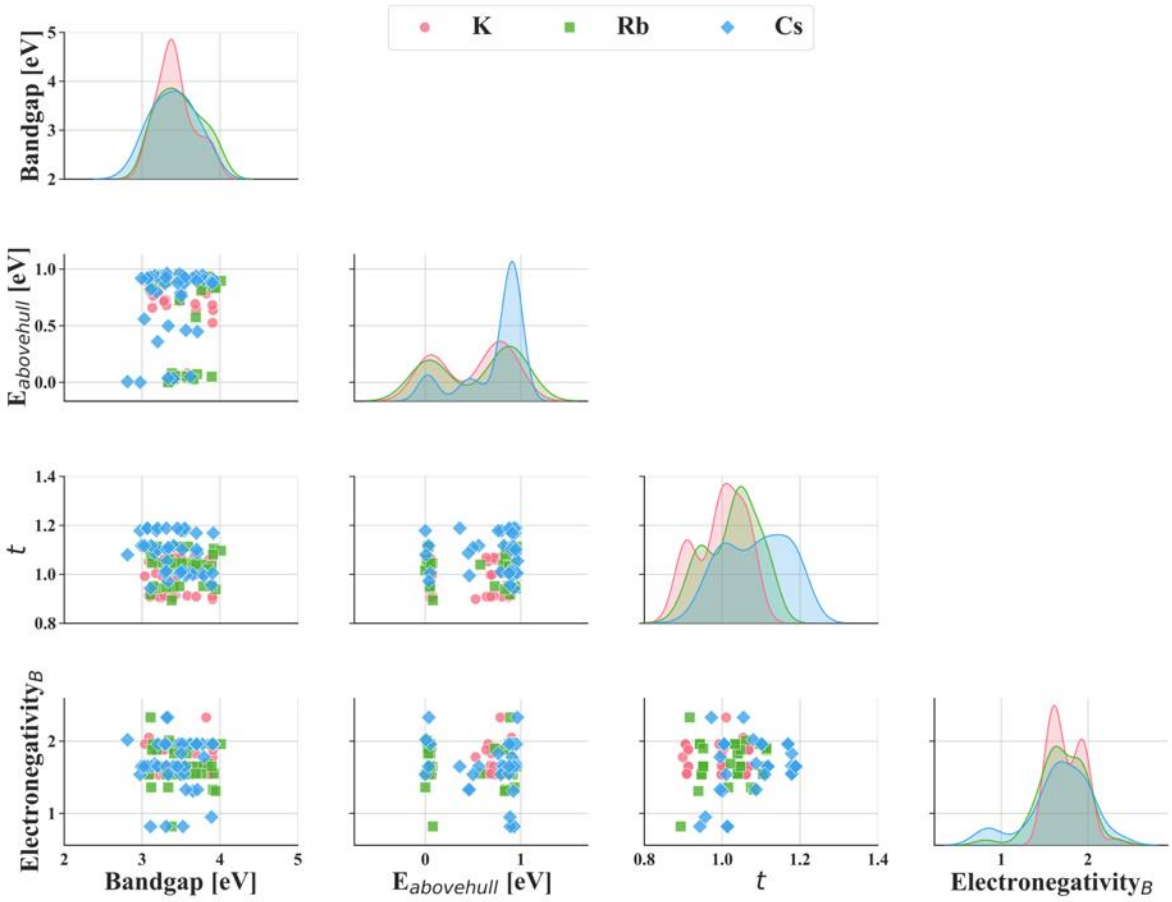


**Figure 6.7**: Relationship between the predicted properties *t* = tolerance factor of interest as a function of the A-site cation choice. For calculating the tolerance factor, I used the atomic radii of the corresponding elements. I observe a strong positive pair-wise relationship between the electronegativity of the B-site cation and the tolerance factor – suggesting the relative importance of electronegativity as a proxy for stability in perovskite systems. We further notice that this observation is valid for all three cations of choice (K, Rb, Cs).

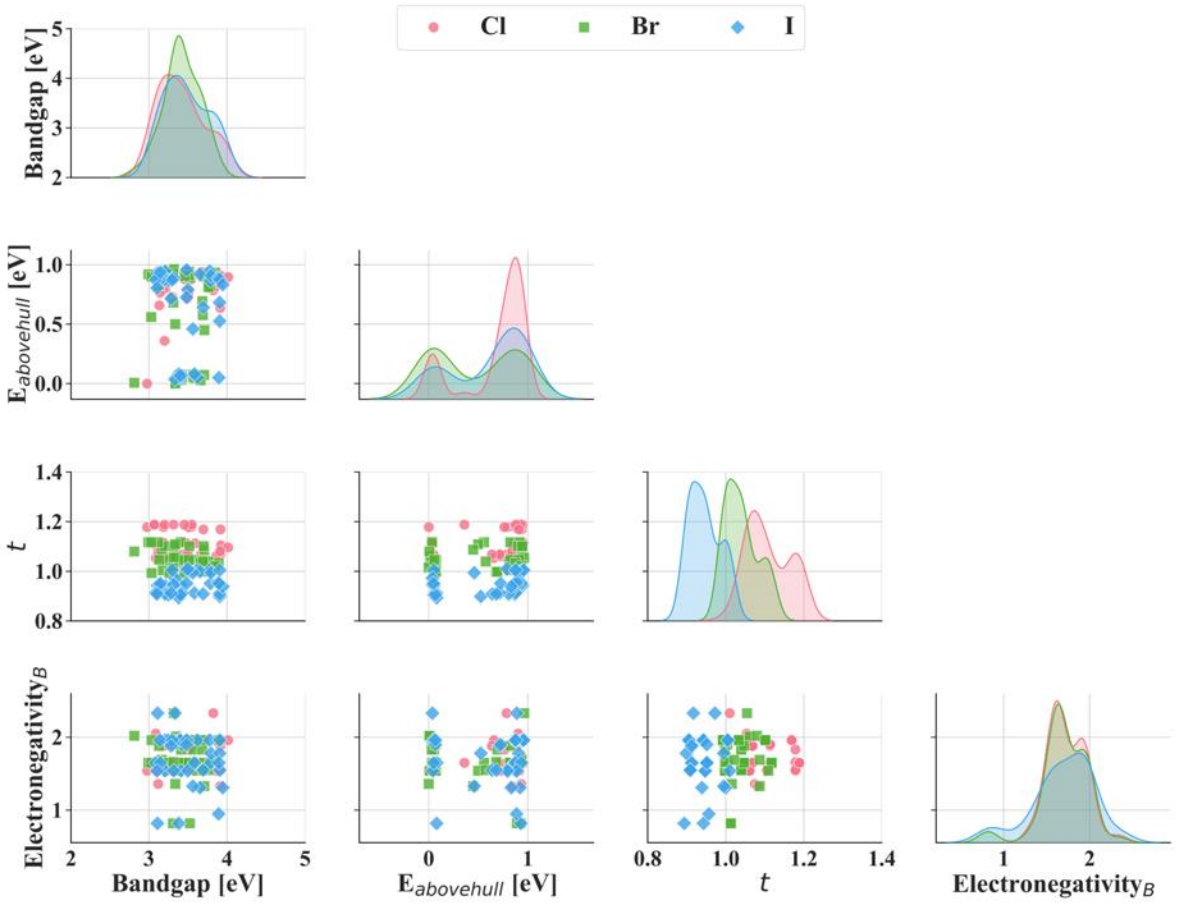


**Figure 6.8**: Pair-wise relationship between the predicted properties of interest as a function of the X-site anion choice. I exhibit the exact same positive pair-wise relationship between the electronegativity of the B-site cation regardless of the choice of anion. The tolerance factor decreases steadily as the radii of the anion increases, as expected. Bromide based perovskites fall into the most "ideal" range of tolerance factors which are a proxy for stability.

I found this newly designed measure to be a strong predictor of stability and plot the resulting proposed candidates as a function of the bandgap and energy above hull (**Figure 6.9a**). I specifically analyzed the "map" for all materials which had low energy above hull (< 0.10 eV) and classify the compounds by their corresponding $\Delta_{X\text{-}B}$ and B-site cation. I found that when $\Delta_{X\text{-}B}$ is within (0.95, 1.5), the material is a stable UV direct bandgap semiconductor (**Figure 6.9b**). I denote this specific range as the Optimal Electronegativity Difference Window (OEDW). The distribution of this metric is shown in **Figure 6.9b**. The inset graph shows the relative frequency

of the five most common elements which occupy the B-site of the ternary structures consisting of the aforementioned criteria.

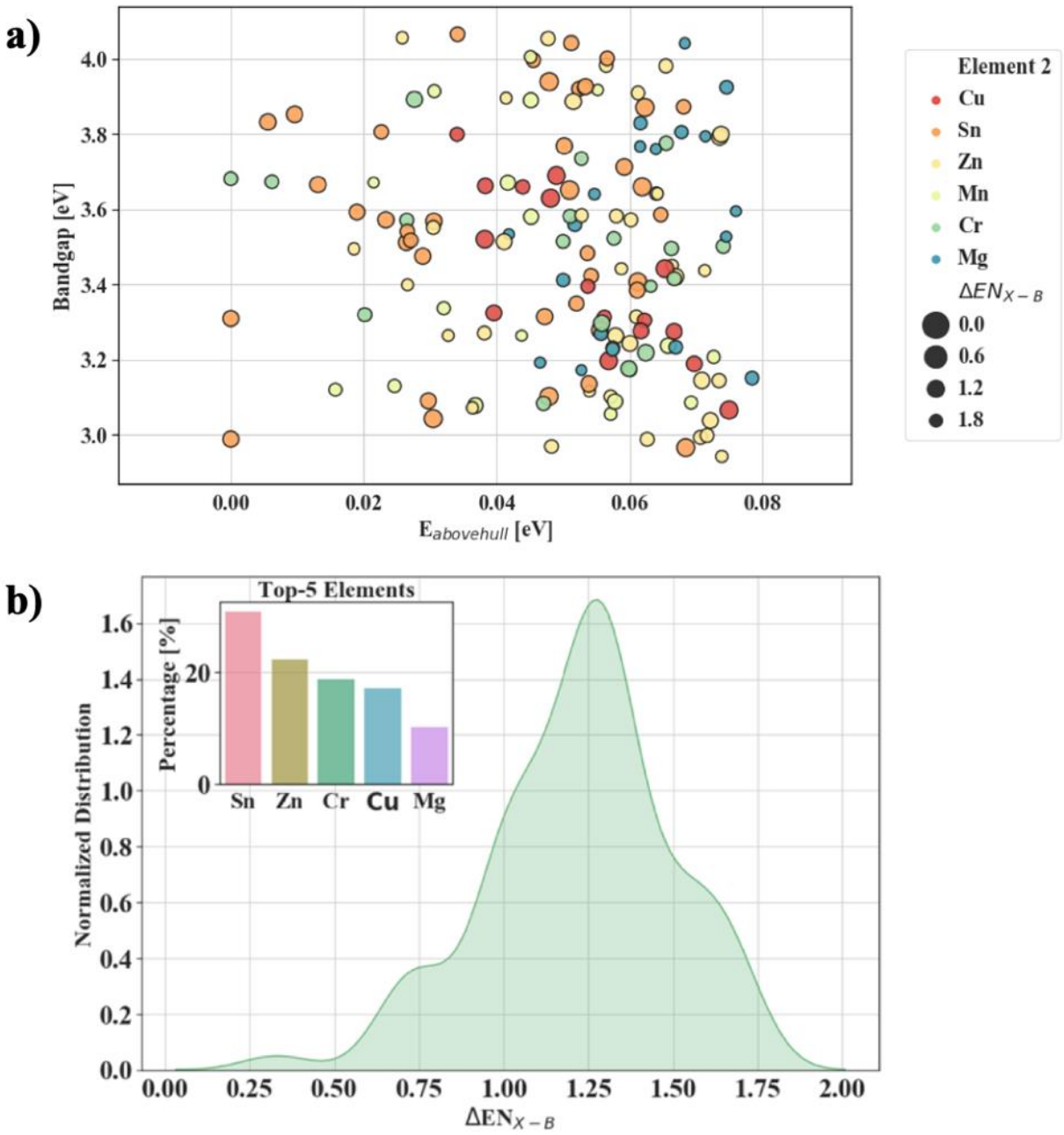


**Figure 6.9**: a) Plot illustrates all proposed candidates which had at least 10 unique structures predicted by DARWIN. The predicted energy above hull and bandgap (mean of all structures containing the same formula) show how the varying B-site cation range spans the entire UV-space and that size of the dot reflects the $\Delta_{X\text{-}B}$ metric we developed. The results suggest an ideal value of 1.2 in systems which comprise of {K, Cs, Rb} and {Cl, Br, I} as the A-site and X-site, respectively are the most optimal choice for combined stability and direct bandgap material. b) Distribution of the difference of electronegativity between B-site (second most metallic element in a ternary) and the halide among all the successful candidates.

Thus, empowered by the accurate ML models and design rules manually extracted via DARWIN, I narrowed our focus towards ternary UV-emitting systems. I narrow down the ternary candidates imposing the A-site to consist of common alkali metals {K, Rb, Cs} and the X-site to be occupied by a halogen species {Cl, Br, I}. Combining these predictions and experimental chemical intuition, I noticed that $K_2CuX_3$ and $Rb_2CuX_3$ (**Figure 6.9b** inset) are predicted to be UV emitters with bandgaps ranging from 3.1 eV to 3.7 eV. In particular, DFT simulations indeed verify the predicted optical properties of both $K_2CuCl_3$ and $K_2CuBr_3$ indicating direct bandgap materials. Further analysis of the elemental contributions in the orbitally-resolved projected density of states (PDOS) reveals that the halide species significantly contributes to the valence band maxima (VBM) of such materials and the B-cation dominates the conduction band minima (CBM) (**Appendix B3 - Figure 1**), thus rationalizing the observation that $\Delta_{X\text{-}B}$ is a good predictor of the bandgap. Specifically, I noticed that $K^+$ does not contribute to the electronic structure of the in $K_2CuX_3$ materials and that the strong orbital interaction of the Cu and Cl species leads to the observed optical properties[115,116].

To assess the validity of these predictions, experimental verification was required. Here, I suggested that experiments be focused on $K_2CuCl_3$ and $K_2CuBr_3$ as initial validation sets given the availability of precursors and ease of solid-state chemical synthesis (see **Appendix A3** for detailed synthesis conditions). This combined human interpretation of the proposed candidates leads to an improved directed and AI-guided approach.

## 6.6 Experimental Realization

$K_2CuCl_3$ and $K_2CuBr_3$ were synthesized via spin-coating with an intermediate anti-solvent dripping step (**Appendix A.3** for detailed procedure) .[117,118] The thin-films were then characterized for their optical and structural properties. The absorption spectrum (**Figure 6.10**, solid violet line) of $K_2CuCl_3$ shows an onset at 360 nm and a photoluminescence peak at 375 nm (**Figure 6.10**, dashed violet line). However, $K_2CuBr_3$ (**Figure 6.10**, blue lines) displays a strong absorption onset at roughly 404 nm and a photoluminescence peak at 420 nm. It is important to note that both materials exhibit a small Stokes-shift, an essential parameter for efficient light-emission. These values corroborate with the expected bulk bandgaps of the material and further confirm the original DFT verified calculations.

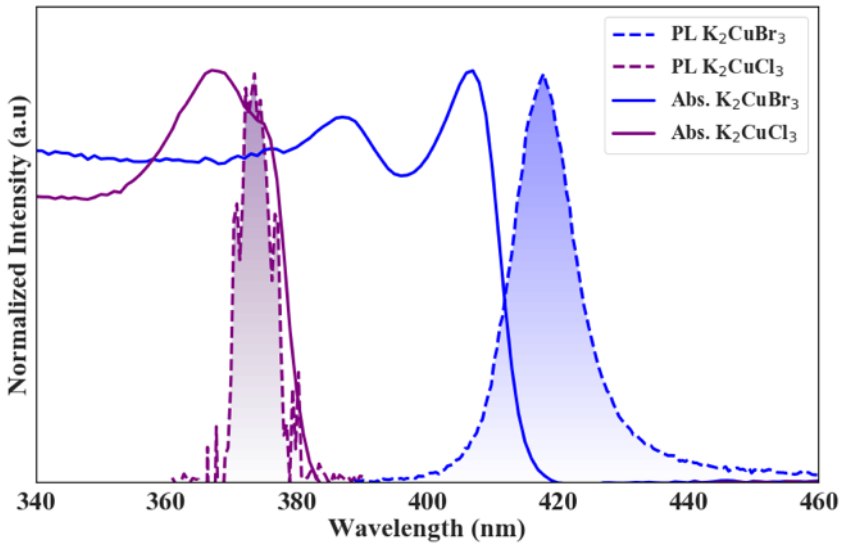


**Figure 6.10**: Absorption spectrum and PL profiles of $K_2CuBr_3$ and $K_2CuCl_3$

Structural characterization is attained by measuring the x-ray diffraction profiles. The diffractograms both indicate high levels of crystalline material as evidenced by the sharp intense peaks. In particular, $K_2CuCl_3$ shows a crystallized structure with diffraction peaks at 14.08°, 14.70°, 15.24° and 15.86°, matching those of simulated bulk $K_2CuCl_3$ (**Figure 6.11** top subplot with violet lines, Materials Project and ICSD-150293) and throughout the full range of 2θ. Similarly, $K_2CuBr_3$ observes strong diffraction peaks occurring at 13.46°, 13.98° and 15.22°, agreeing with bulk $K_2CuBr_3$ (**Figure 6.11** bottom subplot with blue lines, Materials Project and ICSD-150293).

The shift to larger 2θ angles in $K_2CuCl_3$ relative to $K_2CuBr_3$ is expected as the $r_{Cl^-} > r_{Br^-}$, and as previously reported – the expanded lattice leads to an increase in angles of diffraction.[119] This family of materials forms in the orthorhombic crystal arrangement and space group *Pnma*, exhibiting 1D chains of $[CuX_3]^{2-}$ (X = Cl, Br), separated by $K^+$ as shown in Figure 4a (similar to $Rb_2CuX_3$ systems)[115,116]. Coincidentally, previous reports have found these materials prevalent in X-ray scintillator applications[116]. DARWIN can clearly reproduce conventional materials discovery efforts underlining its significant applicability in materials research.

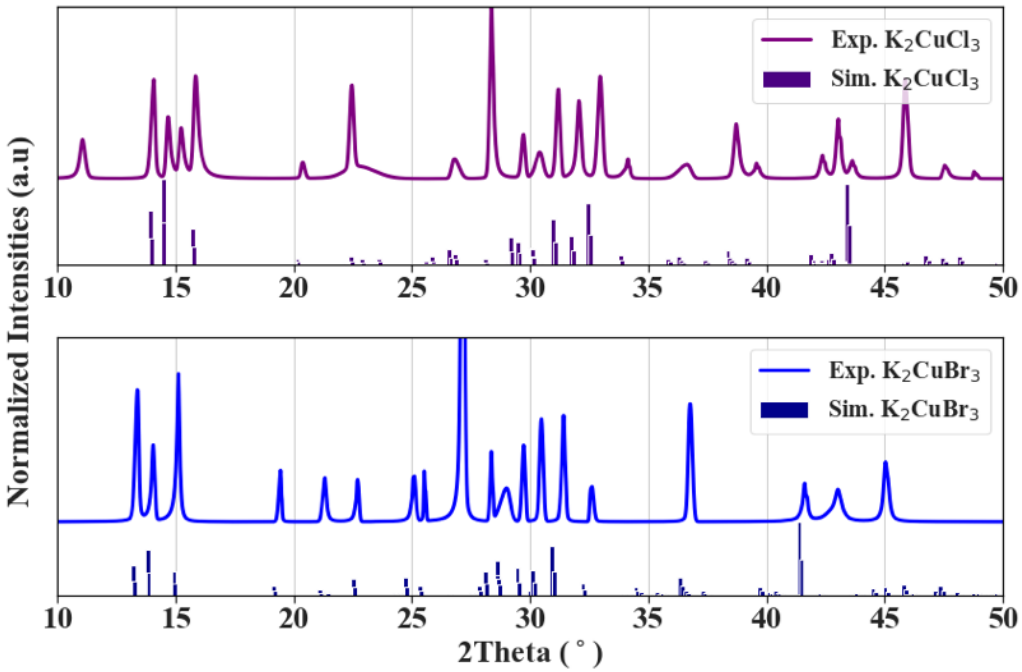


**Figure 6.11**: Simulated[120] and experimental (powder) X-ray diffraction measurements of $K_2CuBr_3$ and $K_2CuCl_3$ .

## 6.7 Summary

In this chapter I focused on the design of materials aided by the use of machine learning techniques – namely, deep learning and evolutionary computing. DARWIN demonstrates that a computational well-designed neural network enabled efficient, rapid and predictions which accelerate materials discovery and exploration. The manual post-prediction human analysis led to the construction of heuristic rules, which ultimately guided experimental efforts, and a previously-underexplored set of semiconducting materials was identified. The results of this study offer a proof-of-concept principle for novel materials design. Future work on ML algorithms that account for overall device architecture will further increase the probability of success in predicting materials for application.

# 7 Conclusion

In this thesis, I focused on the design of perovskite materials for light-emitting applications through experimental and computational methods. Here, I summarize the key results of each individual research project comprising this thesis and then provide an outline for future work to further advance the studies of perovskites as the next-generation of light-emitting materials for consumer display applications. I end with a list of my publications during my graduate studies.

## 7.1 Summary of Findings

I began by pursuing a colloidal synthesis strategy to create perovskite quantum dots for deep-blue emission. I posited that a mixed-cation perovskite quantum dot would exhibit improved spectral stability while simultaneously modifying the optoelectronic bandgap. Pure perovskite quantum dots of $CsPbCl_3$ or $CsPbBr_3$ are known not to achieve the desired blue wavelengths, and thus prior researchers had relied on mixed systems of $CsPbCl_{3-x}Br_x$. However, these mixtures were widely observed to lead to large spectral shifts as a consequence of the halide segregation occurring in devices under applied bias.

I found that by introducing $Rb^+$ directly during synthesis of $CsPbBr_3$ nanocrystals I was able alloy and form $Rb_xCs_{1-x}PbBr_3$. The addition of $Rb^+$ resulted in enlarging the bandgap of pure $CsPbBr_3$ and shifting emission towards the blue. Additionally, the mixed-cation approach addressed the spectral instability of blue-emitting PQDs as a pure bromine perovskite crystal phase was retained. Blue perovskite quantum dots of various geometries were synthesized via modification of the reaction conditions to yield narrow emission linewidths. I found that $Rb_xCs_{1-x}PbBr_3$ LEDs exhibited stable and narrow electroluminescence emissions, while simultaneously demonstrating record high luminance values at peak operating external quantum efficiencies: 93 cd $m^{-2}$ at 0.75% and 29 cd $m^{-2}$ at 0.11% for sky-blue (490 nm) and deep-blue (464 nm) emission, respectively. This work shed light into the A-site compositional engineering of perovskites as a method to design blue emitting materials which lacked voltage-induced phase segregation and yielding colour-pure electroluminescence devices.

I found that dimensionality reduction of 3D perovskite systems provided an additional route to blue-emitting materials. Modifying the dimensionality of quasi-2D perovskites, through a post-

synthesis thin-film treatment, I was able to precisely control the fabrication of the quantum wells produced in the resulting material films – which addressed the major limitation of phase dispersion in the field of reduced dimensional perovskites. This method relied on organic phosphoryl compounds whose interactions with perovskite grain surfaces yielded narrow phase distributions of the perovskite composition. I found that DPPOCl in particular was an ideal molecule which stimulated the reaction kinetics, leading to precise and limited phase distributions with improved quantum yields, efficient charge funneling and narrowed the emission relative to conventional $PbX_2$ precursor doped strategies. Materials characterizations and computational studies led to the development of the theoretical explanation and hypothesis of the hydrolysis reaction kinetics which resulted in the chlorine-insertion mechanism while simultaneously passivating the edge states. These findings explained the observed improvements in the optoelectronic properties. Based on these findings, steady-state devices were fabricated to illustrate the benefit of the dynamic strategy for bright and colour-pure blue-emitting perovskites. The DPPOCl treated perovskite LEDs exhibited improved lifetime stabilities and no wavelength shift between half and maximum luminance of the emission spectra under operation, with record high EQEs. In sum, this work developed insight of tailoring perovskite nanostructures for addressing spectral and operating stability – a combination which is essential for practical light-emitting applications.

Although significant experimental research progress has been made in developing novel perovskites by compositional tuning, the vast combinations of elements hinder experimental efforts for high-throughput materials exploration. I then investigated the role of accelerated materials discovery by utilizing machine learning to predict perovskite compositions with desired properties. Typical computational methods rely on ab initio calculations to investigate novel compositions of perovskite systems, which are computationally expensive and inefficient when considering the size of the materials space. I address this by levering Deep Neural Networks to build a model which accurately predicts the optoelectronic properties and better relative to traditional DFT methods. These models were built and trained on a specific dataset, which then act as surrogates to an evolutionary algorithm utilizing them to rapidly search through materials space and predict compositions with the desired target properties. The approach enabled chemical insights such as the optimal electronegativity difference window of the B-site and X-site in ternary perovskites to be derived from the proposed candidate solutions, which enabled a focused approach towards experimental realization of these compounds. Ultimately, several of the

predicted compounds were successfully synthesized in the lab highlighting the relative importance of computational methods in the realm of materials discovery. It was estimated that approximately acceleration factors of 100-fold were attained using the method to search for materials when compared to traditional machine learning methods. Overall, this work represented a stepping stone towards the blend of experimental and computation methods for advancing research in the design of materials systems, particularly in ternary perovskites for light-emitting applications.

## 7.2 Future Directions

This work highlights strategies that can be implemented experimentally and computationally to advance the design of perovskite systems. The studies were particularly focused on the needs of displays. Although significant progress has been made in the area of PeLEDs, much remains to be studied and understood in this emerging class of materials which has gained a large interest in the past decade in terms of degradation mechanisms. Ultimately, for these materials to reach commercialization in consumer electronics it is imperative to develop not only materials but device architectures which enable high luminance, long operating lifetimes and colour-pure emissions.

### 7.2.1 Advancing A-site alloyed systems for practical application

In the context of A-site compositional engineering, recently research studies have implemented this strategy similarly in reduced dimensional perovskite systems[97] and have found improved LED performance. In the context of PQDs, the studies I presented showed efficient and spectrally stable PeLEDs during a short-operating measurement. However, to fully realize the potential of the $Rb_xCs_{1-x}PbBr_3$ LEDs, I propose two avenues worth exploring: improvements in the efficiency by an order of tenfold in combination with long-term lifetime tests. Long-term lifetime tests entail measuring the luminance under constant current, or conversely set a constant luminance and modulate the voltage applied in the device to maintain this value. Studies of the degradation in performance would let one understand how the active material is affected in operation. I found in my work that although I was able to synthesize colloidal nanoplates with extremely narrow linewidths, but washing procedures to purify the nanocrystals would remove the long-chain ligands expose the surface of the PQDs with defects (trap states) and reduced PLQYs, and therefore lower EQEs. Therefore, post-passivation schemes such as treating the surface with short chain organic ligands, or conversely inorganic ligands (such as $PbX_2$) would improve the

quality of the synthesized material. Recently, studies have shown that post-treatment and inorganic shelling techniques have significantly improved and led to highly efficient blue emission in perovskites.[52,121] I expect that further research in the passivation schemes for PQDs to be one viable avenue of research which would advance the field of perovskites. Additionally, engineering the device architecture by investigating the optimal hole-transport and electron-transport layer and the role of degradation at the interfaces is also an area which requires much optimization and research effort. Specifically, optimal thickness of the device layers should be studied to enable efficient charge transport and result in efficient recombination.

In application, toxicity is a concern, and research is underway to develop of heavy-metal-free light emitters. Examples of materials which have shown promise include chalcogenide quantum dots such as InP, ZnSe, and also Cu-based perovskites and carbon based quantum dots.[122] Future impact of such technologies can be realized through fast scaling and manufacturing processes enabling the synthesis of large quantities of quantum dots, and fast and precise manufacturing of the PeLEDs. Economies of scale and road to commercialization can be accelerated if current manufacturing processes and techniques which are utilized in the production of OLEDs (ink-jet printing, roll-to-roll, etc) can be adopted with modest modification.

### 7.2.2 Developing improved reduced dimensional perovskites

My work on reduced dimensional perovskites highlighted the ability to modify and control the nanostructures formed during thin-film fabrication. This was only achieved by investigating a particular family of phosphonic chlorides which led to the improved performances. However, many organic molecules with different functional groups remain unexplored in these systems that may offer even further enhancements and tailored optoelectronic properties. Apart from the organic chlorides studied in this work, several groups have shown that ligand length and various functional groups of common alkylammonium molecules lead to improved phase control and fine tunability of perovskite emission.[123–125] However, it has been observed that although this leads to improved device performance, long-term operation is still a limitation for the 2D and quasi-2D systems as they rely on these insulating organic molecules to design the particular quantum confined wells responsible for emission. Therefore, for achieving long operating lifetimes, further work should focus on potentially investigating the loss mechanisms which occur at the nanostructures grain boundaries of the fabricated thin-films. For these materials to compete with

current technologies in mobile displays, target operating lifetimes on the orders of 30,000 – 100,000 hours at peak luminance values ranging between 500 – 1,000 cd $m^{-2}$ should be the ultimate goal. In particular, it would be worthwhile to design using a bilayer organic ligand approach to fine-tune and tailor the formation of nanostructures. In addition, an alternative strategy to yield efficient devices is to investigate organic molecules which simultaneously act as the organic spacer between the wells, but offer high conductivity and thereby potentially alleviating the need for an electron/hole transport layer in the resulting LED. However, this is highly complex and would involve very specific engineering of the organic molecules from an energy band perspective. To augment materials development, device design for efficient photon extraction will go beyond the planar configuration, with its photon extraction losses. Introducing nanostructured cavities in future can help maximize photon extraction and improve device efficiency.

### 7.2.3 The next-frontier of machine learning for applied materials discovery

My contributions to machine learning for accelerated materials discovery advanced a method that levered high-quality datasets. Going forward, one avenue worth exploring is better deep learning models applied to predict material properties with much lower errors. In DARWIN, the input data was structured in a graph format, encoding all atomic information and crystal structure in a manual way. Elemental properties of the constituent atoms were used as input features, but to date there has been a lack of understanding which features are the most important for prediction of the optoelectronic and structural properties. It is therefore worthwhile to focus research efforts on finding an optimal representation of crystal structures for the training and prediction of optoelectronic properties. This would result in highly accurate models which could then be implemented as surrogate models for larger machine learning methods to efficiently and rapidly search through materials space. On that note, DARWIN in particular used an evolutionary algorithm which only used mutation as a means to produce the next set of proposed candidate solutions, however cross-over is another method that could be implemented and indeed produce improved results. The evolutionary algorithm, is a genetic algorithm but there are many other forms which can be introduced to lever the deep learned models and lead to far accelerated predictions of materials. Developing machine learning tools and post-analysis techniques to extract meaningful insights from a chemical and physical perspective is highly sought out by the materials science community. Intuitive understanding and design rules can then be developed and utilized

by experimentalists to help guide future work and pioneer the next set of semiconducting materials for light-emission. As observed with the Human Genome Project, the next revolution of materials design will incorporate a mixed approach whereby computational and experimental methods are implemented simultaneously and rely on one another to advance materials discovery as shown in **Figure 7.1**.

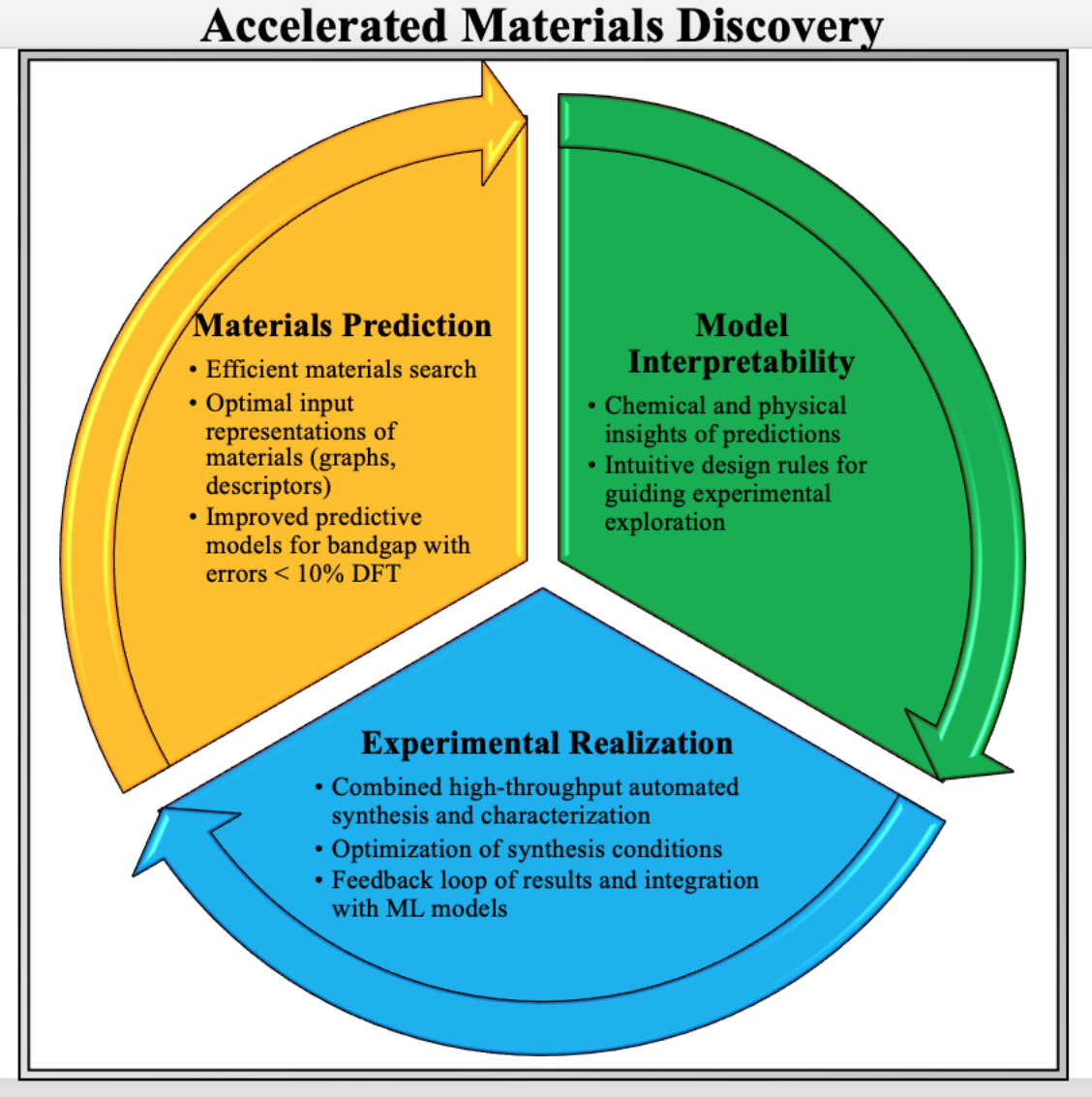


**Figure 7.1**: Accelerated materials discovery roadmap illustrating the various components responsible for designing the next generation of materials. All components work symbiotically to advance the process, requiring focus and attention in various areas.

# 8 List of Publications

**Patents:**

1. Jihyun, M.I.N., Jang, E.J., Jang, H.S., Jain, A., Sargent, E., Voznyy, O., Levina, L., Hoogland, S., **Todorović, P**. and Saidaminov, M., University of Toronto, 2019. *Semiconductor nanocrystal particles and production methods thereof*. U.S. Patent Application 16/254,676.

**First Authored or co-first authored:**

1. **Todorović, P.†,** Ma, D.†, Chen, B., Quintero-Bermudez, R., Saidaminov, M.I., Dong, Y., Lu, Z.H. and Sargent, E.H., 2019. Spectrally Tunable and Stable Electroluminescence Enabled by Rubidium Doping of CsPbBr3 Nanocrystals. *Advanced Optical Materials*, *7*(24), p.1901440.
2. Ma, D.†, **Todorović, P.†,** Meshkat, S., Saidaminov, M.I., Wang, Y.K., Chen, B., Li, P., Scheffel, B., Quintero-Bermudez, R., Fan, J.Z. and Dong, Y., 2020. Chloride Insertion–Immobilization Enables Bright, Narrowband, and Stable Blue-Emitting Perovskite Diodes. *Journal of the American Chemical Society*, *142*(11), pp.5126-5134.
3. Choubisa, H.†, **Todorović, P.†,** Pina, J.M., Parmar, D.H., Li, Z., Voznyy, O., Tamblyn, I., Sargent, E.H., 2021. Interpretable discovery of new semiconductors with machine learning. *Submitted to JACS.*

**Co-Authored Publications (excluding those listed immediately above)**

1. De Luna, P., Quintero-Bermudez, R., DInh, C. T., Ross, M. B., Bushuyev, O. S., **Todorović, P.**, Regier, T., Kelley, S. O., Yang, P. and Sargent, E. H. (2018) 'Catalyst electro-redeposition controls morphology and oxidation state for selective carbon dioxide reduction', *Nature Catalysis*. doi: 10.1038/s41929-017-0018-9.
2. Xu, J., Voznyy, O., Liu, Mengxia, Kirmani, A. R., Walters, G., Munir, R., Abdelsamie, M., Proppe, A. H., Sarkar, A., García De Arquer, F. P., Wei, M., Sun, B., Liu, Min, Ouellette, O., Quintero-Bermudez, R., Li, J., Fan, J., Quan, L., **Todorovic, P.**, Tan, H., Hoogland, S., Kelley, S. O., Stefik, M., Amassian, A. and Sargent, E. H. (2018) '2D matrix engineering for homogeneous quantum dot coupling in photovoltaic solids', *Nature Nanotechnology*. doi: 10.1038/s41565-018-0117-z.

3. Tan, H., Che, F., Wei, M., Zhao, Y., Saidaminov, M. I., **Todorović, P.**, Broberg, D., Walters, G., Tan, F., Zhuang, T., Sun, B., Liang, Z., Yuan, H., Fron, E., Kim, J., Yang, Z., Voznyy, O., Asta, M. and Sargent, E. H. (2018) 'Dipolar cations confer defect tolerance in wide-bandgap metal halide perovskites', *Nature Communications*. doi: 10.1038/s41467-018-05531-8.
4. Nam, D. H., Bushuyev, O. S., Li, J., De Luna, P., Seifitokaldani, A., Dinh, C. T., García De Arquer, F. P., Wang, Y., Liang, Z., Proppe, A. H., Tan, C. S., **Todorović, P.**, Shekhah, O., Gabardo, C. M., Jo, J. W., Choi, J., Choi, M. J., Baek, S. W., Kim, J., Sinton, D., Kelley, S. O., Eddaoudi, M. and Sargent, E. H. (2018) 'Metal-Organic Frameworks Mediate Cu Coordination for Selective CO2 Electroreduction', *Journal of the American Chemical Society*. doi: 10.1021/jacs.8b06407.
5. De Luna, P., Liang, W., Mallick, A., Shekhah, O., García De Arquer, F. P., Proppe, A. H., **Todorović, P.**, Kelley, S. O., Sargent, E. H. and Eddaoudi, M. (2018) 'Metal-Organic Framework Thin Films on High-Curvature Nanostructures Toward Tandem Electrocatalysis', *ACS Applied Materials and Interfaces*. doi: 10.1021/acsami.8b04848.
6. Proppe, A. H., Elkins, M. H., Voznyy, O., Pensack, R. D., Zapata, F., Besteiro, L. V., Quan, L. N., Quintero-Bermudez, R., **Todorovic, P.**, Kelley, S. O., Govorov, A. O., Gray, S. K., Infante, I., Sargent, E. H. and Scholes, G. D. (2019) 'Spectrally Resolved Ultrafast Exciton Transfer in Mixed Perovskite Quantum Wells', *Journal of Physical Chemistry Letters*. doi: 10.1021/acs.jpclett.9b00018.
7. Gao, Y., Walters, G., Qin, Y., Chen, B., Min, Y., Seifitokaldani, A., Sun, B., **Todorovic, P.**, Saidaminov, M. I., Lough, A., Tongay, S., Hoogland, S. and Sargent, E. H. (2019) 'Electro-Optic Modulation in Hybrid Metal Halide Perovskites', *Advanced Materials*. doi: 10.1002/adma.201808336.
8. Yang, Z., Wei, M., Voznyy, O., **Todorovic, P.**, Liu, M., Quintero-Bermudez, R., Chen, P., Fan, J. Z., Proppe, A. H., Quan, L. N., Walters, G., Tan, H., Chang, J. W., Jeng, U. S., Kelley, S. O. and Sargent, E. H. (2020) 'Anchored Ligands Facilitate Efficient B-Site doping in metal halide perovskites', *Journal of the American Chemical Society*. doi: 10.1021/jacs.9b02565.
9. Quintero-Bermudez, R., Proppe, A. H., Mahata, A., **Todorović, P.**, Kelley, S. O., De Angelis, F. and Sargent, E. H. (2019) 'Ligand-Induced Surface Charge Density Modulation Generates Local Type-II Band Alignment in Reduced-Dimensional Perovskites', *Journal of the American Chemical Society*. doi: 10.1021/jacs.9b04801.

10. Voznyy, O., Levina, L., Fan, J. Z., Askerka, M., Jain, A., Choi, M. J., Ouellette, O., **Todorović, P.**, Sagar, L. K. and Sargent, E. H. (2019) 'Machine Learning Accelerates Discovery of Optimal Colloidal Quantum Dot Synthesis', *ACS Nano*. doi: 10.1021/acsnano.9b03864.
11. Fan, J. Z., Andersen, N. T., Biondi, M., **Todorović, P.**, Sun, B., Ouellette, O., Abed, J., Sagar, L. K., Choi, M. J., Hoogland, S., de Arquer, F. P. G. and Sargent, E. H. (2019) 'Mixed Lead Halide Passivation of Quantum Dots', *Advanced Materials*. doi: 10.1002/adma.201904304.
12. Biondi, M., Choi, M. J., Ouellette, O., Baek, S. W., **Todorović, P.**, Sun, B., Lee, S., Wei, M., Li, P., Kirmani, A. R., Sagar, L. K., Richter, L. J., Hoogland, S., Lu, Z. H., García de Arquer, F. P. and Sargent, E. H. (2020) 'A Chemically Orthogonal Hole Transport Layer for Efficient Colloidal Quantum Dot Solar Cells', *Advanced Materials*. doi: 10.1002/adma.201906199.
13. Wang, X., Wang, Z., Zhuang, T. T., Dinh, C. T., Li, J., Nam, D. H., Li, F., Huang, C. W., Tan, C. S., Chen, Z., Chi, M., Gabardo, C. M., Seifitokaldani, A., **Todorović, P.**, Proppe, A., Pang, Y., Kirmani, A. R., Wang, Y., Ip, A. H., Richter, L. J., Scheffel, B., Xu, A., Lo, S. C., Kelley, S. O., Sinton, D. and Sargent, E. H. (2019) 'Efficient upgrading of CO to C3 fuel using asymmetric C-C coupling active sites', *Nature Communications*. doi: 10.1038/s41467-019-13190-6.
14. Johnston, A., Dinic, F., **Todorović, P.**, Chen, B., Sagar, L. K., Saidaminov, M. I., Hoogland, S., Voznyy, O. and Sargent, E. H. (2020) 'Narrow Emission from Rb3Sb2I9 Nanoparticles', *Advanced Optical Materials*. doi: 10.1002/adom.201901606.
15. Na Quan, L., Ma, D., Zhao, Y., Voznyy, O., Yuan, H., Bladt, E., Pan, J., García de Arquer, F. P., Sabatini, R., Piontkowski, Z., Emwas, A. H., **Todorović, P.**, Quintero-Bermudez, R., Walters, G., Fan, J. Z., Liu, M., Tan, H., Saidaminov, M. I., Gao, L., Li, Y., Anjum, D. H., Wei, N., Tang, J., McCamant, D. W., Roeffaers, M. B. J., Bals, S., Hofkens, J., Bakr, O. M., Lu, Z. H. and Sargent, E. H. (2020) 'Edge stabilization in reduced-dimensional perovskites', *Nature Communications*. doi: 10.1038/s41467-019-13944-2.
16. Choi, J., Choi, M. J., Kim, J., Dinic, F., **Todorovic, P.**, Sun, B., Wei, M., Baek, S. W., Hoogland, S., García de Arquer, F. P., Voznyy, O. and Sargent, E. H. (2020) 'Stabilizing Surface Passivation Enables Stable Operation of Colloidal Quantum Dot Photovoltaic Devices at Maximum Power Point in an Air Ambient', *Advanced Materials*. doi: 10.1002/adma.201906497.

17. Wang, Y., Wang, Z., Dinh, C. T., Li, J., Ozden, A., Golam Kibria, M., Seifitokaldani, A., Tan, C. S., Gabardo, C. M., Luo, M., Zhou, H., Li, F., Lum, Y., McCallum, C., Xu, Y., Liu, M., Proppe, A., Johnston, A., **Todorovic, P.**, Zhuang, T. T., Sinton, D., Kelley, S. O. and Sargent, E. H. (2020) 'Catalyst synthesis under CO2 electroreduction favours faceting and promotes renewable fuels electrosynthesis', *Nature Catalysis*. doi: 10.1038/s41929-019-0397-1.
18. Zhuang, T. T., Li, Y., Gao, X., Wei, M., García de Arquer, F. P., **Todorović, P.**, Tian, J., Li, G., Zhang, C., Li, X., Dong, L., Song, Y., Lu, Y., Yang, X., Zhang, L., Fan, F., Kelley, S. O., Yu, S. H., Tang, Z. and Sargent, E. H. (2020) 'Regioselective magnetization in semiconducting nanorods', *Nature Nanotechnology*. doi: 10.1038/s41565-019-0606-8.
19. Wei, M., Xiao, K., Walters, G., Lin, R., Zhao, Y., Saidaminov, M. I., **Todorović, P.**, Johnston, A., Huang, Z., Chen, H., Li, A., Zhu, J., Yang, Z., Wang, Y. K., Proppe, A. H., Kelley, S. O., Hou, Y., Voznyy, O., Tan, H. and Sargent, E. H. (2020) 'Combining Efficiency and Stability in Mixed Tin–Lead Perovskite Solar Cells by Capping Grains with an Ultrathin 2D Layer', *Advanced Materials*. doi: 10.1002/adma.201907058.
20. Kirman, J., Johnston, A., Kuntz, D. A., Askerka, M., Gao, Y., **Todorović, P.**, Ma, D., Privé, G. G. and Sargent, E. H. (2020) 'Machine-Learning-Accelerated Perovskite Crystallization', *Matter*. doi: 10.1016/j.matt.2020.02.012.
21. Sagar, L.K., Bappi, G., Johnston, A., Chen, B., **Todorović, P.**, Levina, L., Saidaminov, M.I., García de Arquer, F.P., Hoogland, S. and Sargent, E.H., (2020). Single-Precursor Intermediate Shelling Enables Bright, Narrow Line Width InAs/InZnP-Based QD Emitters. *Chemistry of Materials*.
22. Tan, C. S., Hou, Y., Saidaminov, M. I., Proppe, A., Huang, Y. S., Zhao, Yicheng, Wei, M., Walters, G., Wang, Z., Zhao, Yongbiao, **Todorovic, P.**, Kelley, S. O., Chen, L. J. and Sargent, E. H. (2020) 'Heterogeneous Supersaturation in Mixed Perovskites', *Advanced Science*. doi: 10.1002/advs.201903166.
23. Biondi, M., Choi, M.J., Ouellette, O., Baek, S.W., **Todorović, P**., Sun, B., Lee, S., Wei, M., Li, P., Kirmani, A.R. and Sagar, L.K., 2020. A chemically orthogonal hole transport layer for efficient colloidal quantum dot solar cells. *Advanced Materials*, *32*(17), p.1906199.
24. Xue Wang, Ziyun Wang, F. Pelayo García de Arquer, Cao-Thang Dinh, Adnan Ozden, Yuguang C. Li, Dae-Hyun Nam, Jun Li, Yi-Sheng Liu, Joshua Wicks, Zitao Chen, Miaofang Chi, Bin Chen, Ying Wang, Jason Tam, Jane Y. Howe, Andrew Proppe, **Petar Todorović**,

Fengwang Li, Tao-Tao Zhuang, Christine M. Gabardo, Ahmad R. Kirmani, Christopher McCallum, Sung-Fu Hung, Yanwei Lum, Mingchuan Luo, Yimeng Min, Aoni Xu, Colin P. O'Brien, Bello Stephen, Bin Sun, Alexander H. Ip, Lee J. Richter, Shana O. Kelley, David Sinton and Edward H. Sargent (2020). Efficient electrically powered CO 2-to-ethanol via suppression of deoxygenation. *Nature Energy*, *5*(6), 478-486

25. Choi, M.J., Baek, S.W., Lee, S., Biondi, M., Zheng, C., **Todorovic, P.**, Li, P., Hoogland, S., Lu, Z.H., de Arquer, F.P.G. and Sargent, E.H., 2020. Colloidal Quantum Dot Bulk Heterojunction Solids with Near-Unity Charge Extraction Efficiency. *Advanced Science*, *7*(15), p.2000894.
26. Dong, Yitong and Wang, Ya-Kun and Yuan, Fanglong and Johnston, Andrew and Liu, Yuan and Ma, Dongxin and Choi, Min-Jae and Chen, Bin and Chekini, Mahshid and Baek, Se-Woong and Sagar, Laxmi Kishore and Fan, James and Hou, Yi and Wu, Mingjian and Lee, Seungjin and Sun, Bin and Hoogland, Sjoerd and Quintero-Bermudez, Rafael and Ebe, Hinako and **Todorovic, Petar** and Dinic, Filip and Li, Peicheng and Kung, Hao Ting and Saidaminov, Makhsud I. and Kumacheva, Eugenia and Spiecker, Erdmann and Liao, Liang-Sheng and Voznyy, Oleksandr and Lu, Zheng-Hong and Sargent, Edward H. (2020). Bipolar-shell resurfacing for blue LEDs based on strongly confined perovskite quantum dots. *Nature Nanotechnology*, *15*(8), 668-674.
27. Sagar, L. K., Bappi, G., Johnston, A., Chen, B., **Todorović, P**., Levina, L., Saidaminov, M.I., García de Arquer, F.P., Nam, D.H., Choi, M.J. Hoogland, S., Sargent, E. H. (2020). Suppression of Auger Recombination by Gradient Alloying in InAs/CdSe/CdS QDs. *Chemistry of Materials*, *32*(18), 7703-7709.

.

# 9 References


1. IEA, I. E. A. World Energy Outlook 2019 – Analysis - IEA. *World Energy Outlook 2019* (2019).
2. Kimble, A., Dc, W., Gallinat, C., Alarcon, H. & Bennich, P. Global Lighting Challenge : Changing the world through public-private partnerships. 1671–1675
3. IEA. Cooling – Tracking Buildings – Analysis - IEA. *IEA Reports* (2019).
4. John, D. Buildings: Tracking Clean Energy Progress. *Tracking Clean Energy Progress* (2019).
5. U.S. Department of Energy. *2016 Solid-State Lighting R&D Plan*. *Electronic Publishing* (2016). doi:10.1017/S1365100512000181
6. Consulting, N. Energy Savings Forecast of Solid-State Lighting in General Illumination Applications. *U.S. Dep. Energy Rep.* (2014).
7. GSMA Association. The Mobile Economy 2020. *Gsma* (2020).
8. IDC, I. D. C. IDC - Smartphone Market Share. *IDC: The premier global market intelligence company* (2020).
9. O'Dea, S. Global smartphone sales to end users 2007-2021. *Statista.com* (2020).
10. Jang, E. Environmentally Friendly Quantum Dots for Display Applications. in *Technical Digest - International Electron Devices Meeting, IEDM* (2019). doi:10.1109/IEDM.2018.8614647
11. Lee, E., Wang, C. K., Yurek, J. & Ma, R. A new frontier for quantum dots in displays. *Inf. Disp. (1975).* (2018). doi:10.1002/j.2637-496X.2018.tb01132.x
12. Lee, J. H. Qd display: A game-changing technology for the display industry. *Information Display* (2020). doi:10.1002/msid.1163
13. Display, S. Quantum Dot Physics- A Guide to Understanding QD Displays. *Samsung Disp.* (2018).
14. Led, L. Chapter 6 : Light -Emitting Diodes Photoluminescence and Electroluminescence. 1–36
15. Smith, T. & Guild, J. The C.I.E. colorimetric standards and their use. *Transactions of the Optical Society* (1931). doi:10.1088/1475-4878/33/3/301
16. Wright, W. D. A re-determination of the trichromatic coefficients of the spectral colours.

*Trans. Opt. Soc.* (1929). doi:10.1088/1475-4878/30/4/301

17. CIE, C. Commission internationale de l'eclairage proceedings, 1931. *Cambridge Univ. Cambridge* (1931).
18. International Telecommunication Union - ITU-R. Parameter values for ultra-high definition television systems for production and international programme exchange. *Recomm. ITU-R BT.2020* (2014).
19. International Telecommunication Union. Parameter values for the HDTV standards for production and international programme exchange. *Recommendation ITU-R BT.709-6* **5**, (2002).
20. Sugawara, M., Choi, S. Y. & Wood, D. Ultra-high-definition television (Rec. ITU-R BT.2020): A generational leap in the evolution of television [standards in a nutshell]. *IEEE Signal Process. Mag.* (2014). doi:10.1109/MSP.2014.2302331
21. ITU. Recommendation ITU-R BT.2020-2: Parameter values for ultra-high definition television systems for production and international programme exchange. *Recommendation ITU-R BT.2020* (2015).
22. Schanda, J. *Colorimetry: Understanding the CIE System*. *Colorimetry: Understanding the CIE System* (2007). doi:10.1002/9780470175637
23. Berends, A. C. & De Mello Donega, C. Ultrathin One- and Two-Dimensional Colloidal Semiconductor Nanocrystals: Pushing Quantum Confinement to the Limit. *Journal of Physical Chemistry Letters* (2017). doi:10.1021/acs.jpclett.7b01640
24. Tan, Z. K. *et al.* Bright light-emitting diodes based on organometal halide perovskite. *Nat. Nanotechnol.* **9**, 687–692 (2014).
25. Murray, C. B., Norris, D. J. & Bawendi, M. G. Synthesis and Characterization of Nearly Monodisperse CdE (E = S, Se, Te) Semiconductor Nanocrystallites. *J. Am. Chem. Soc.* (1993). doi:10.1021/ja00072a025
26. Sinatra, L.; Pan, J. . B. O. Methods of Synthesizing Monodisperse Colloidal Quantum Dots. *Mater. Matters* (2017).
27. Zhou, Y., Chen, J., Bakr, O. M. & Sun, H. T. Metal-Doped Lead Halide Perovskites: Synthesis, Properties, and Optoelectronic Applications. *Chemistry of Materials* **30**, 6589–6613 (2018).
28. Akkerman, Q. A., Rainò, G., Kovalenko, M. V. & Manna, L. Genesis, challenges and

opportunities for colloidal lead halide perovskite nanocrystals. *Nat. Mater.* **17**, 394–405 (2018).

29. Pasquarelli, R. M., Ginley, D. S. & O'hayre, R. Solution processing of transparent conductors: From flask to film. *Chem. Soc. Rev.* (2011). doi:10.1039/c1cs15065k
30. Sutherland, B. R. & Sargent, E. H. Perovskite photonic sources. *Nature Photonics* (2016). doi:10.1038/nphoton.2016.62
31. Dubey, D. K. *et al.* Wide Color Gamut deep-blue OLED Architecture for Display Application. **85**, 33–39 (2018).
32. Bergman, L. Blue high-efficiency TADF emitters for OLED lighting; Cynora GmbH. in *DOE SSL Workshop* 9 (2018).
33. Kim, Y. H., Cho, H. & Lee, T. W. Metal halide perovskite light emitters. *Proceedings of the National Academy of Sciences of the United States of America* (2016). doi:10.1073/pnas.1607471113
34. Wang, L. *et al.* Blue Quantum Dot Light-Emitting Diodes with High Electroluminescent E ffi ciency. *Appl. Mater. Interfaces* **9**, 38755–38760 (2017).
35. Pathak, S. *et al.* Perovskite Crystals for Tunable White Light Emission. *Chem. Mater.* **27**, 8066–8075 (2015).
36. Brandt, R. E. *et al.* Searching for " Defect-Tolerant " Photovoltaic Materials: Combined Theoretical and Experimental Screening. *Chem. Mater.* **29**, 4667–4674 (2017).
37. Protesescu, L. *et al.* Nanocrystals of Cesium Lead Halide Perovskites (CsPbX3, X = Cl, Br, and I): Novel Optoelectronic Materials Showing Bright Emission with Wide Color Gamut. *Nano Lett.* **15**, 3692–3696 (2015).
38. Quan, L. N., García de Arquer, F. P., Sabatini, R. P. & Sargent, E. H. Perovskites for Light Emission. *Advanced Materials* (2018). doi:10.1002/adma.201801996
39. Deschler, F. *et al.* High photoluminescence efficiency and optically pumped lasing in solution-processed mixed halide perovskite semiconductors. *J. Phys. Chem. Lett.* (2014). doi:10.1021/jz5005285
40. Xing, G. *et al.* Low-temperature solution-processed wavelength-tunable perovskites for lasing. *Nat. Mater.* (2014). doi:10.1038/nmat3911
41. Green, M. A., Ho-Baillie, A. & Snaith, H. J. The emergence of perovskite solar cells. *Nature Photonics* (2014). doi:10.1038/nphoton.2014.134

42. Kojima, A., Teshima, K., Shirai, Y. & Miyasaka, T. Organometal halide perovskites as visible-light sensitizers for photovoltaic cells. *J. Am. Chem. Soc.* (2009). doi:10.1021/ja809598r
43. Lee, M. M., Teuscher, J., Miyasaka, T., Murakami, T. N. & Snaith, H. J. Efficient hybrid solar cells based on meso-superstructured organometal halide perovskites. *Science (80-. ).* **338**, 643–647 (2012).
44. Dou, L. *et al.* Solution-processed hybrid perovskite photodetectors with high detectivity. *Nat. Commun.* (2014). doi:10.1038/ncomms6404
45. Stranks, S. D. & Snaith, H. J. Metal-halide perovskites for photovoltaic and light-emitting devices. *Nature Nanotechnology* **10**, 391–402 (2015).
46. Mao, L., Stoumpos, C. C. & Kanatzidis, M. G. Two-Dimensional Hybrid Halide Perovskites: Principles and Promises. *J. Am. Chem. Soc.* (2019). doi:10.1021/jacs.8b10851
47. Lin, K. *et al.* Perovskite light-emitting diodes with external quantum efficiency exceeding 20 per cent. *Nature* **562**, 245–248 (2018).
48. Chiba, T. *et al.* Anion-exchange red perovskite quantum dots with ammonium iodine salts for highly efficient light-emitting devices. *Nat. Photonics* **12**, 681–687 (2018).
49. Hou, S., Gangishetty, M. K., Quan, Q. & Congreve, D. N. Efficient Blue and White Perovskite Light- Emitting Diodes via Manganese Doping. *Joule* (2018). doi:10.1016/j.joule.2018.08.005
50. Quan, L. N. *et al.* Edge management in reduced-dimensional perovskites enables efficient and stable light-emitting diodes. *Under Rev.*
51. Na Quan, L. *et al.* Edge stabilization in reduced-dimensional perovskites. *Nat. Commun.* (2020). doi:10.1038/s41467-019-13944-2
52. Hoye, R. L. Z. *et al.* Identifying and Reducing Interfacial Losses to Enhance Color-Pure Electroluminescence in Blue-Emitting Perovskite Nanoplatelet Light-Emitting Diodes. *ACS Energy Lett.* **4**, 1181–1188 (2019).
53. Xing, J. *et al.* Color-stable highly luminescent sky-blue perovskite light-emitting diodes. *Nat. Commun.* (2018). doi:10.1038/s41467-018-05909-8
54. Cheng, L. *et al.* Sky-blue perovskite light-emitting diodes based on quasi-two-dimensional layered perovskites. *Chinese Chem. Lett.* **28**, 29–31 (2017).

55. Vashishtha, P., Ng, M., Shivarudraiah, S. B. & Halpert, J. E. High Efficiency Blue and Green Light-Emitting Diodes Using Ruddlesden-Popper Inorganic Mixed Halide Perovskites with Butylammonium Interlayers. *Chem. Mater.* **31**, 83–89 (2019).
56. Pan, J. *et al.* Highly Efficient Perovskite-Quantum-Dot Light-Emitting Diodes by Surface Engineering. *Adv. Mater.* (2016). doi:10.1002/adma.201600784
57. Li, G. *et al.* Highly Efficient Perovskite Nanocrystal Light-Emitting Diodes Enabled by a Universal Crosslinking Method. *Adv. Mater.* **28**, 3528–3534 (2016).
58. Song, J. *et al.* Quantum Dot Light-Emitting Diodes Based on Inorganic Perovskite Cesium Lead Halides (CsPbX3). *Adv. Mater.* **27**, 7162–7167 (2015).
59. Kumawat, N. K. *et al.* Band Gap Tuning of $CH_3NH_3Pb(Br_{1-x}Cl_x)_3$ Hybrid Perovskite for Blue Electroluminescence. *ACS Appl. Mater. Interfaces* **7**, 13119–13124 (2015).
60. Bohn, B. J. *et al.* Boosting Tunable Blue Luminescence of Halide Perovskite Nanoplatelets through Postsynthetic Surface Trap Repair. *Nano Lett.* **18**, 5231–5238 (2018).
61. Xiao, J. W. *et al.* Stabilizing RbPbBr 3 Perovskite Nanocrystals through Cs + Substitution. *Chem. - A Eur. J.* **25**, 2597–2603 (2019).
62. Park, Y. H. *et al.* Inorganic Rubidium Cation as an Enhancer for Photovoltaic Performance and Moisture Stability of HC(NH2)2PbI3 Perovskite Solar Cells. *Adv. Funct. Mater.* **27**, (2017).
63. Linaburg, M. R., McClure, E. T., Majher, J. D. & Woodward, P. M. Cs1-xRbxPbCl3 and Cs1-xRbxPbBr3 Solid Solutions: Understanding Octahedral Tilting in Lead Halide Perovskites. *Chem. Mater.* **29**, 3507–3514 (2017).
64. Maughan, A. E., Ganose, A. M., Almaker, M. A., Scanlon, D. O. & Neilson, J. R. Tolerance Factor and Cooperative Tilting Effects in Vacancy-Ordered Double Perovskite Halides. *Chem. Mater.* **30**, 3909–3919 (2018).
65. Amgar, D., Binyamin, T., Uvarov, V. & Etgar, L. Near ultra-violet to mid-visible band gap tuning of mixed cation Rb : X Cs 1- x PbX 3 (X = Cl or Br) perovskite nanoparticles. *Nanoscale* **10**, 6060–6068 (2018).
66. Wu, H. *et al.* $Rb^+$ cations enable the change of luminescence properties in perovskite ($Rb_xCs_{1-x}PbBr_3$) quantum dots. *Nanoscale* **10**, 3429–3437 (2018).

67. Protesescu, L. *et al.* Dismantling the 'red Wall' of Colloidal Perovskites: Highly Luminescent Formamidinium and Formamidinium-Cesium Lead Iodide Nanocrystals. *ACS Nano* **11**, 3119–3134 (2017).
68. Akkerman, Q. A. *et al.* Tuning the optical properties of cesium lead halide perovskite nanocrystals by anion exchange reactions. *J. Am. Chem. Soc.* **137**, 10276–10281 (2015).
69. Liu, Y. *et al.* Considerably enhanced exciton emission of CsPbCl3 perovskite quantum dots by the introduction of potassium and lanthanide ions. *Nanoscale* **10**, 14067–14072 (2018).
70. Gangishetty, M. K., Hou, S., Quan, Q. & Congreve, D. N. Reducing Architecture Limitations for Efficient Blue Perovskite Light-Emitting Diodes. *Adv. Mater.* **30**, (2018).
71. Hou, S., Gangishetty, M. K., Quan, Q. & Congreve, D. N. Efficient Blue and White Perovskite Light-Emitting Diodes via Manganese Doping. *Joule* **2**, 2421–2433 (2018).
72. Walsh, A. & Stranks, S. D. Taking Control of Ion Transport in Halide Perovskite Solar Cells. *ACS Energy Lett.* **3**, 1983–1990 (2018).
73. Wu, Y., Li, X. & Zeng, H. Highly Luminescent and Stable Halide Perovskite Nanocrystals. *ACS Energy Lett.* **4**, 673–681 (2019).
74. Wu, Y. *et al.* In Situ Passivation of PbBr 64- Octahedra toward Blue Luminescent CsPbBr 3 Nanoplatelets with Near 100% Absolute Quantum Yield. *ACS Energy Lett.* **3**, 2030–2037 (2018).
75. Zou, Y., Yuan, Z., Bai, S., Gao, F. & Sun, B. Recent progress toward perovskite light-emitting diodes with enhanced spectral and operational stability. *Mater. Today Nano* **5**, 100028 (2019).
76. Shamsi, J., Urban, A. S., Imran, M., De Trizio, L. & Manna, L. Metal Halide Perovskite Nanocrystals: Synthesis, Post-Synthesis Modifications, and Their Optical Properties. *Chem. Rev.* **119**, 3296–3348 (2019).
77. Quan, L. N. *et al.* Ligand-Stabilized Reduced-Dimensionality Perovskites. *J. Am. Chem. Soc.* (2016). doi:10.1021/jacs.5b11740
78. Wehrenfennig, C., Eperon, G. E., Johnston, M. B., Snaith, H. J. & Herz, L. M. High charge carrier mobilities and lifetimes in organolead trihalide perovskites. *Adv. Mater.* (2014). doi:10.1002/adma.201305172
79. Shi, D. *et al.* Low trap-state density and long carrier diffusion in organolead trihalide

perovskite single crystals. *Science (80-. ).* (2015). doi:10.1126/science.aaa2725

80. Wang, Y. *et al.* All-Inorganic Colloidal Perovskite Quantum Dots: A New Class of Lasing Materials with Favorable Characteristics. *Adv. Mater.* **27**, 7101–7108 (2015).
81. Stranks, S. D. *et al.* Electron-hole diffusion lengths exceeding 1 micrometer in an organometal trihalide perovskite absorber. *Science (80-. ).* **342**, 341–344 (2013).
82. Quan, L. N. *et al.* Perovskites for Next-Generation Optical Sources. *Chemical Reviews* (2019). doi:10.1021/acs.chemrev.9b00107
83. Yuan, M. *et al.* Perovskite energy funnels for efficient light-emitting diodes. *Nat. Nanotechnol.* **11**, 872–877 (2016).
84. Wang, K. H. *et al.* Efficient and Color-Tunable Quasi-2D CsPbBr x Cl 3- x Perovskite Blue Light-Emitting Diodes. *ACS Photonics* (2019). doi:10.1021/acsphotonics.8b01490
85. Yoon, Y. J. *et al.* Reversible, Full-Color Luminescence by Post-treatment of Perovskite Nanocrystals. *Joule* (2018). doi:10.1016/j.joule.2018.07.012
86. Zhang, L. *et al.* Ultra-bright and highly efficient inorganic based perovskite light-emitting diodes. *Nat. Commun.* **8**, (2017).
87. Kovalenko, M. V., Protesescu, L. & Bodnarchuk, M. I. Properties and potential optoelectronic applications of lead halide perovskite nanocrystals. *Science* (2017). doi:10.1126/science.aam7093
88. Shi, E. *et al.* Extrinsic and Dynamic Edge States of Two-Dimensional Lead Halide Perovskites. *ACS Nano* (2019). doi:10.1021/acsnano.8b07631
89. Vashishtha, P. & Halpert, J. E. Field-Driven Ion Migration and Color Instability in Red-Emitting Mixed Halide Perovskite Nanocrystal Light-Emitting Diodes. *Chem. Mater.* (2017). doi:10.1021/acs.chemmater.7b01609
90. Hieulle, J. *et al.* Unraveling the Impact of Halide Mixing on Perovskite Stability. *J. Am. Chem. Soc.* (2019). doi:10.1021/jacs.8b11210
91. Xing, J. *et al.* Ultrafast ion migration in hybrid perovskite polycrystalline thin films under light and suppression in single crystals. *Phys. Chem. Chem. Phys.* (2016). doi:10.1039/c6cp06496e
92. Quan, L. N. *et al.* Tailoring the Energy Landscape in Quasi-2D Halide Perovskites Enables Efficient Green-Light Emission. *Nano Lett.* (2017). doi:10.1021/acs.nanolett.7b00976

93. Dequilettes, D. W. *et al.* Photoluminescence Lifetimes Exceeding 8 μs and Quantum Yields Exceeding 30% in Hybrid Perovskite Thin Films by Ligand Passivation. *ACS Energy Lett.* (2016). doi:10.1021/acsenergylett.6b00236
94. Gualdrón-Reyes, A. F. *et al.* Controlling the Phase Segregation in Mixed Halide Perovskites through Nanocrystal Size. *ACS Energy Lett.* (2019). doi:10.1021/acsenergylett.8b02207
95. Kumawat, N. K., Liu, X. K., Kabra, D. & Gao, F. Blue perovskite light-emitting diodes: Progress, challenges and future directions. *Nanoscale* **11**, 2109–2120 (2019).
96. Liang, D. *et al.* Color-Pure Violet-Light-Emitting Diodes Based on Layered Lead Halide Perovskite Nanoplates. *ACS Nano* **10**, 6897–6904 (2016).
97. Jiang, Y. *et al.* Spectra stable blue perovskite light-emitting diodes. *Nat. Commun.* **10**, (2019).
98. Liu, Y. *et al.* Efficient blue light-emitting diodes based on quantum-confined bromide perovskite nanostructures. *Nature Photonics* (2019). doi:10.1038/s41566-019-0505-4
99. Li, Z. *et al.* Modulation of recombination zone position for quasi-two-dimensional blue perovskite light-emitting diodes with efficiency exceeding 5%. *Nat. Commun.* **10**, (2019).
100. Xie, T. & Grossman, J. C. Crystal Graph Convolutional Neural Networks for an Accurate and Interpretable Prediction of Material Properties. *Phys. Rev. Lett.* (2018). doi:10.1103/PhysRevLett.120.145301
101. Chen, C., Ye, W., Zuo, Y., Zheng, C. & Ong, S. P. Graph Networks as a Universal Machine Learning Framework for Molecules and Crystals. *Chem. Mater.* (2019). doi:10.1021/acs.chemmater.9b01294
102. Duvenaud, D. *et al.* Convolutional networks on graphs for learning molecular fingerprints. in *Advances in Neural Information Processing Systems* (2015).
103. Back, S. *et al.* Convolutional Neural Network of Atomic Surface Structures to Predict Binding Energies for High-Throughput Screening of Catalysts. *J. Phys. Chem. Lett.* (2019). doi:10.1021/acs.jpclett.9b01428
104. Park, C. W. & Wolverton, C. Developing an improved crystal graph convolutional neural network framework for accelerated materials discovery. *Phys. Rev. Mater.* (2020). doi:10.1103/physrevmaterials.4.063801
105. Jain, A. *et al.* A high-throughput infrastructure for density functional theory calculations.

*Comput. Mater. Sci.* (2011). doi:10.1016/j.commatsci.2011.02.023

106. Padgham, L. & Winikoff, M. *Developing Intelligent Agent Systems*. *Developing Intelligent Agent Systems* (2004). doi:10.1002/0470861223
107. Wooldridge, M. Intelligent Agents: The Key Concepts. in (2002). doi:10.1007/3-540-45982-0_1
108. Hassanat, A. *et al.* Choosing mutation and crossover ratios for genetic algorithms-a review with a new dynamic approach. *Inf.* (2019). doi:10.3390/info10120390
109. Kearnes, S., McCloskey, K., Berndl, M., Pande, V. & Riley, P. Molecular graph convolutions: moving beyond fingerprints. *J. Comput. Aided. Mol. Des.* (2016). doi:10.1007/s10822-016-9938-8
110. Davies, D. W. *et al.* Computational Screening of All Stoichiometric Inorganic Materials. *Chem* (2016). doi:10.1016/j.chempr.2016.09.010
111. Allahyari, Z. & Oganov, A. R. Coevolutionary search for optimal materials in the space of all possible compounds. *npj Comput. Mater.* (2020). doi:10.1038/s41524-020-0322-9
112. Goldschmidt, V. M. Die Gesetze der Krystallochemie. *Naturwissenschaften* (1926). doi:10.1007/BF01507527
113. Bhalla, A. S., Guo, R. & Roy, R. The perovskite structure - A review of its role in ceramic science and technology. *Materials Research Innovations* (2000). doi:10.1007/s100190000062
114. Bartel, C. J. *et al.* New tolerance factor to predict the stability of perovskite oxides and halides. *Sci. Adv.* (2019). doi:10.1126/sciadv.aav0693
115. Yang, B. *et al.* Lead-Free Halide Rb2CuBr3 as Sensitive X-Ray Scintillator. *Adv. Mater.* (2019). doi:10.1002/adma.201904711
116. Gao, W. *et al.* 1D all-inorganic K2CuBr3 with violet emission as efficient X-ray scintillators. *ACS Appl. Electron. Mater.* (2020). doi:10.1021/acsaelm.0c00414
117. Spingler, B., Schnidrig, S., Todorova, T. & Wild, F. Some thoughts about the single crystal growth of small molecules. *CrystEngComm* (2012). doi:10.1039/c1ce05624g
118. *Springer Handbook of Crystal Growth*. *Springer Handbook of Crystal Growth* (2010). doi:10.1007/978-3-540-74761-1
119. Comin, R. *et al.* Structural, optical, and electronic studies of wide-bandgap lead halide perovskites. *J. Mater. Chem. C* (2015). doi:10.1039/c5tc01718a

120. Jain, A. *et al.* Commentary: The materials project: A materials genome approach to accelerating materials innovation. *APL Materials* (2013). doi:10.1063/1.4812323
121. Dong, Y. *et al.* Bipolar-shell resurfacing for blue LEDs based on strongly confined perovskite quantum dots. *Nat. Nanotechnol.* (2020). doi:10.1038/s41565-020-0714-5
122. Chen, F., Lin, Q., Shen, H. & Tang, A. Blue quantum dot-based electroluminescent light-emitting diodes. *Materials Chemistry Frontiers* (2020). doi:10.1039/d0qm00029a
123. Shang, Y. *et al.* Highly stable hybrid perovskite light-emitting diodes based on Dion-Jacobson structure. *Sci. Adv.* (2019). doi:10.1126/sciadv.aaw8072
124. He, T. *et al.* Reduced-dimensional perovskite photovoltaics with homogeneous energy landscape. *Nat. Commun.* (2020). doi:10.1038/s41467-020-15451-1
125. Deng, W. *et al.* 2D Ruddlesden–Popper Perovskite Nanoplate Based Deep-Blue Light-Emitting Diodes for Light Communication. *Adv. Funct. Mater.* (2019). doi:10.1002/adfm.201903861
126. De Mello, J. C., Wittmann, H. F. & Friend, R. H. An improved experimental determination of external photoluminescence quantum efficiency. *Adv. Mater.* (1997). doi:10.1002/adma.19970090308
127. Kirklin, S. *et al.* The Open Quantum Materials Database (OQMD): Assessing the accuracy of DFT formation energies. *npj Comput. Mater.* (2015). doi:10.1038/npjcompumats.2015.10
128. Schmidt, J. *et al.* Predicting the Thermodynamic Stability of Solids Combining Density Functional Theory and Machine Learning. *Chem. Mater.* (2017). doi:10.1021/acs.chemmater.7b00156

# Appendices

## A. Methods

### A.1 Chapter 4 – Enabling Deep-Blue Emission in Perovskite Quantum Dots

#### Experimental Methods

**Materials**: All chemicals used are commercially available and were used as received without any additional purification steps: lead (II) bromide ($PbBr_2$, Alfa-Aesar Puratronic, 99.998%), cesium carbonate ($Cs_2CO_3$, Sigma-Aldrich, 99%), rubidium carbonate ($Rb_2CO_3$, Sigma-Aldrich, 99%), oleic acid (OA, Sigma-Aldrich, 98%), oleylamine (OLA, Caledon), octadecene (ODE, Caledon), ethyl acetate (EtAc, anhydrous, Sigma-Aldrich, 99.8%), methyl acetate (MeAc, anhydrous, Sigma-Aldrich, 99.8%), hexane (anhydrous, Alfa-Aesar), octane (Alfa-Aesar) and chlorobenzene (anhydrous, Sigma-Aldrich). PEDOT: PSS (Clevios$^{TM}$ PVP Al 4083) was purchased from Heraeus. Poly-TPD was purchased from American Dye Source. 1,3,5-tris(N-phenylbenzimiazole-2-yl)benzene (TPBi) was purchased from Lumtec.

**Synthesis of Rb-oleate**: $Rb_2CO_3$ (0.430 g, 1.86 mmol, Sigma-Aldrich 99%) was added to ODE (20 mL) and OA (1.5 mL) in a 100 mL round-bottom flask. The mixture was heated to 120 °C under vacuum and dried for 1 hour. Then, the flask was put under nitrogen and heated to 150 °C for complete dissolution and formation of Rb-oleate.

**Synthesis of Cs-oleate**: $Cs_2CO_3$ (0.433 g, 1.33 mmol, Sigma-Aldrich 99%) was added to ODE (20 mL) and OA (1.25 mL) in a 100 mL round-bottom flask. The mixture was heated to 120 °C under vacuum and dried for 1 h. Then, the flask was put under nitrogen and heated to 150 °C for complete dissolution and formation of Cs-oleate.

**Synthesis of $Rb_xCs_{1-x}PbBr_3$ Nanocrystals**: $PbBr_2$ (0.068 g, 0.187 mmol, Alfa-Aesar, 99.99%) was dissolved in ODE (5 mL) along with oleic acid and oleyl amine (1:1 volumetric ratio, 1 mL each). The solution was degassed for a total of 1 h at 120 °C, then switched over to a pure nitrogen environment and heated to 150 °C to fully dissolve any remaining $PbBr_2$. Upon heating, a 0.4 mL mixture of Rb-oleate (0.23 mL) / (0.17 mL) Cs-oleate solution was injected into this $PbBr_2$ solution at various temperatures (120 – 150 °C). Nanoplates were synthesized by modifying the ratio of

OA:OLA from 1:1 to 2:1, yielding anisotropic growth. After 15 s of injection, the crude solution was cooled in an ice-water bath. In addition, the nanocrystals can be synthesized in a one-step precursor injection by simultaneously dissolving both $Cs_2CO_3$ (0.215 g) and $Rb_2CO_3$ (0.215 g) in ODE (20 mL) and OA (1.5 mL) in a 100 mL reaction flask and heated to same reaction conditions as for the individual oleate precursors. Then 0.4 mL of this mixed oleate solution is injected into the Pb-oleate solution.

**Purification of $Rb_xCs_{1-x}PbBr_3$ Nanocrystals**: Upon cooling down to room temperature, the crude solution was collected, and centrifuged at 7830 rpm for 10 min. The resulting supernatant was discarded, and the precipitate containing the perovskite quantum dots was collected by redispersion in hexane (2 mL). A mixture of methyl acetate and ethyl acetate (1:1 volumetric, 6 mL total) was added to precipitate the solubilized nanocrystals. The resulting mixture was then centrifuged once again at 7830 RPM for 5 min. The supernatant was discarded and the precipitate was redispersed into hexane or octane for further measurements.

**Photoluminescence (PL) and Absorption Measurements**: Photoluminescence measurements were done using a Horiba Fluorolog Time-Correlated Single Photon Counting system equipped with UV/Vis/NIR photomultiplier tube detectors, dual grating spectrometers, and a monochromatized xenon lamp excitation source. A pulsed UV laser diode ($\lambda$ = 374 nm) was used to acquire the transient PL signal. Absolute PLQY values were measured by coupling a Quantum-Phi integrating sphere to the Fluorolog system through optical fibres. All PLQY measurements followed published methods.[126] Optical absorption measurements were carried out in a Lambda 950 UV-Vis-IR spectrophotometer.

**X-ray Diffraction (XRD) Measurements**: XRD measurements were conducted using a Rigaku MiniFlex 600 diffractometer (Bragg-Brentano geometry) equipped with a NaI scintillation counter detector and a monochromatized Cu Kα radiation source ($\lambda$ = 1.5406 Å) operating at a voltage of 40 kV and current of 15 mA.

**X-ray Photoelectron Spectroscopy (XPS) measurement**: XPS measurements were carried out with the Thermo Scientific K-Alpha XPS system. An Al Kα source with a 400 µm spot size was used for measurements to detect photo-electrons at specific energy ranges to determine the presence of specific elements.

**Electron Microscopy**: Bright field and high angle annular dark field (HAADF) images were collected at an acceleration voltage of 300 kV using a Hitachi HF-3300 electron microscope. Elemental mapping was acquired by a Bruker energy dispersive x-ray spectroscopic detector.

**UPS Measurement**: UPS spectra were measured on ITO substrates with high conductivity. Photoelectron spectroscopy was performed in a PHI5500 Multi-Technique system using non-monochromatized He-I$\alpha$ radiation ($h\nu$ = 21.22 eV). All the work function and valence band measurements were performed at a take-off angle of 88 º, with the base chamber pressure of $10^{-7}$ Pa. A bias of -5 V was applied to measure the work function.

**LED fabrication**: First 100 Ω/sq ITO-coated glass substrates were sequentially cleaned by detergent, deionized water, acetone and isopropanol in an ultrasonic washer, then treated by ultraviolet ozone plasma for 5 min and employed as the anode. Then a solution of PEDOT: PSS was spin-coated at 500 rpm for 10 s then 4500 rpm for 90 s, followed by annealing on a hot plate at 150 °C for 20 min in the air ambient. The substrates were cooled down and transferred into a nitrogen-filled glovebox. Poly-TPD (3.5 mg $mL^{-1}$ in chlorobenzene) was spin-coated at 2000 rpm for 60 s (1000 rpm $s^{-1}$ ramp) and annealed at 100 °C for 10 min in a nitrogen-filled glovebox, leading to a thickness of roughly 10 nm. On top of this layer, perovskite QDs dispersed in octane (10 mg $mL^{-1}$) were spin-coated at 2000 rpm for 60 s (1000 rpm $s^{-1}$ ramp). Finally, the substrates were transferred into a high vacuum thermal evaporator, where TPBi (60 nm), LiF (1 nm) and Al (150 nm) were deposited thereon layer by layer through a shadow mask under a high vacuum of less than $10^{-4}$ Pa. The device active area was 6.14 $mm^2$ as defined by the overlapping area of the ITO and Al electrodes. The devices were encapsulated before the measurements, using an ultraviolet curable resin (exposure under ultraviolet light for 20 s) and covered on the edges between the device and a transparent glass chip.

**LED evaluation**: All devices were tested under ambient condition. The luminance versus voltages and the current density versus voltage characteristics were collected using a HP4140B picoammeter. The absolute EL power spectra were collected using an integrating sphere and an Ocean Optics USB4000 spectrometer by mounting of the devices on the wall of the integrating sphere. The EQEs were then calculated through the measured absolute EL power spectra and the current density.

## A.2 Chapter 5 – Improving Spectral Stability in Perovskite LEDs

**Perovskite Fabrication.** The precursor solution for the perovskite with a stoichiometry of $PEA_2Cs_{1.6}MA_{0.4}Pb_3Br_{10}$ was prepared by dissolving $PbBr_2$ (0.6 mol/L), CsBr (0.32 mol/L), MABr (0.08 mol/L) and PEABr (0.4 mol/L) in DMSO under continuous stirring for 40 min in a nitrogen-filled glovebox at room temperature. The resulting clear and colourless solution was dripped onto the substrates after filtration, pre-spun at 1000 rpm for 10 s, then spin-coated at 5000 rpm for 60 s. To fabricate the initial green-emitting perovskite, 0.5 mL of chloroform was dripped to promote crystallization after 30 s during the second step. The control $PEA_2Cs_{1.6}MA_{0.4}Pb_3Br_{10-x}Cl_x$ ($x$ = 1, 2, or 3) were fabricated through similar steps, while the precursor solutions were prepared by using a mixture of $PbCl_2$ partially replacing $PbBr_2$ (the total concentration of $Pb^{2+}$ is 0.6 mol/L), CsBr (0.32 mol/L), MABr (0.08 mol/L) and PEABr (0.4 mol/L). To fabricate the perovskites using a dynamic treatment, 0.5 mL of chloroform containing the organic chloride (DPPOCl, $PPOCl_2$, $PSO_2Cl$ or PCOCl) was dripped onto the film and spin-coated after 30 s during the second step. Finally all the films were annealed on a hot plate at 90 $^oC$ for 5 min to remove the residual solvents.

**LED Fabrication.** First the patterned low-conductivity ITO-coated glass substrates were sequentially cleaned by detergent, deionized water, acetone and isopropanol in an ultrasonic washer, then treated by ultraviolet ozone plasma for 5 min and employed as the anode. To prepare the PEDOT: PSS: PFI layer, a mixed solution of PEDOT: PSS and PFI (at the mass ratio of 1:1) was pre-spun at 500 rpm for 10 s then spin-coated 4500 rpm for 90 s, followed by annealing on a hot plate at 150 $^oC$ for 20 min in ambient condition. To prepare the PEDOT: PSS/ poly-TPD layer, the PEDOT: PSS solution was spin-coated at 4000 rpm for 60 s, annealed on a hot plate at 150 $^oC$ for 20 min in ambient condition. Later the poly-TPD solution (6 mg/mL in anisole) was spin-coated at 5000 rpm for 60 s. Then the substrates were transferred into a nitrogen-filled glovebox, and the perovskite films were fabricated thereon as described above. Finally the substrates were transferred into a high vacuum thermal evaporator, where TPBi (30 nm), LiF (1 nm) and Al (150 nm) were deposited thereon layer by layer through a shadow mask at a pressure below $10^{-4}$ Pa.

**PL Characterization.** A Horiba Fluorolog system was used for PL characterization. Steady-state PL was measured with a monochromatized Xe lamp as the excitation source. A Time Correlated Single Photon Counting (TCSPC) detector and a pulsed UV S5 laser diode (Delta Diode 375, peak

wavelength 374 nm, 2 MHz) were used to acquire transient PL. An instrument response function of $\Delta t = 0.13$ ns provides a limit to the overall time resolution. Time-resolved emission spectra were recorded by measuring individual transient PL traces at increasing emission wavelengths. PL stability was measured in air using the laser diode (Delta Diode 375, peak wavelength 374 nm, 100 MHz) with a peak power of 300 mW and average power of 1.8 mW. The spot size was ~0.01 cm2, so the calculated excitation density was 180 mW/cm2. Absolute PLQY values were obtained by coupling a Quanta-Phi integrating sphere to the Fluorolog system through optical fiber bundles. All the PLQY measurements followed published methods.S7 Both excitation and emission spectra were measured for three cases: the sample directly illuminated by the excitation beam path in the integrating sphere, the sample offset within the integrating sphere from the beam path, and the empty sphere itself. For PLQY measurements, the Fluorolog was set to an excitation wavelength of 380 nm and a 2 nm bandpass for both the excitation and emission slits. Using these settings, the resulting spectra had high signal to noise ratios and provided an excitation intensity in a range of 1~30 mW/cm2. The detector was calibrated for spectral variance with a Newport white light source. The excitation intensity was varied for intensity dependent PL spectra by changing the slit width on the Fluorolog monochromator. Excitation intensity was obtained by recording the power with an Ophir LaserStar Dual Channel Power and energy meter and by calculating the beam area through the known dispersion relations for the monochromator.

**XRD Measurement**. XRD measurements were conducted using a Rigaku MiniFlex 600 diffractometer (Bragg-Brentano geometry) equipped with a NaI scintillation counter detector and a monochromatized Cu Kα radiation source ($\lambda = 1.5406$ Å) operating at a voltage of 40 kV and current of 15 mA. The crystallite size was calculated using Scherrer Equation,

$$\tau = K\lambda/\beta cos\theta$$

where $\tau$ is the mean size of the crystalline domains, which may be smaller or equal to the grain size; K is a dimensionless shape factor, with a value close to unity; $\lambda$ is the Xray wavelength; $\beta$ is the line broadening at half the maximum intensity, after subtracting the instrumental line broadening, in radians; and $\theta$ is the Bragg angle.

**TA measurement**. A regeneratively amplified Yb: KGW laser (PHAROS, Light Conversion) was used to generate femtosecond laser pulses at a wavelength of 1030 nm as the fundamental beam

with a repetition rate of 5 kHz. The fundamental beam was passed through a beam splitter, where the majority of the beam was used to pump an optical parametric amplifier (ORPHEUS, Light Conversion) to serve as a narrow-band pump (pulse duration ~200 fs, bandwidth ~10 nm). The remaining part of the beam was focused into a translating sapphire crystal in order to generate a white light probe ranging between 400 and 800 nm. The pump and probe pulses were directed into a commercial transient absorption spectrometer (Helios, Ultrafast). The probe pulse was sent to a retroreflector mounted on a delay stage where multiple reflections off the retroreflector allowed for a delay relative to the pump pulse of up to 8 ns. Sample measurements were obtained with pump powers between 50 and 100 μW, and a spot size of 0.3 $\square m^2$ (assumption-Gaussian beam profile).

**XPS Measurement**. XPS measurements were carried out with the Thermo Scientific K-Alpha XPS system. An Al Kα source with a 400 μm spot size was used to detect photo-electrons at specific energy ranges to determine the presence of specific elements. XPS compositions were measured at two separate depth levels: the surface and ~30 nm depth. The samples were etched with a beam of 1 keV $Ar^+$ ions at two intervals of 60 s at roughly a rate of 0.23 nm/s. After the etching was completed, measurements were performed. The chemical compositions were obtained by integration of the XPS spectra using the Thermo Advantage software.

**AFM Measurement**. AFM measurements were performed with an Asylum Research Cypher AFM operated in AC mode in air. Imaging was done using ASYELEC-02 silicon probes with titanium-iridium coatings from Asylum Research. The probes had a typical spring constant of 42 N/m.

**SEM Measurement**. Top-view and cross-sectional SEM images were collected in secondary electron mode by a Hitachi SU5000. The measurements were operated at a voltage of 3 kV with a spot size of 3 and an intensity of 10.

**LED Evaluation**. The device active area was 6.14 $mm^2$ as defined by the overlapping area of the ITO and Al electrodes. The devices were encapsulated before the current density and luminance measurements, using an ultraviolet curable resin (exposure under ultraviolet light for 20 s) and

covered on the edges between the device and a transparent glass chip. All the devices were tested in ambient conditions. We used the LED measurement approach of Forrest et al. We took the angular dependence of the intensity and of the EL spectrum, into consideration by using an integrating sphere, which collects light emitted across angles. The current-voltage (I-V) characteristic was measured using a Keithley 6430 source meter. The absolute radiation flux for calculating the EQE, power efficiency and luminance was collected using an integrating sphere and an Ocean Optics USB4000 spectrometer, the system calibrated with the aid of a standard halogen lamp (Ocean Optics HL-2000). The device was mounted on the open aperture of the integrating sphere to allow the light emitted from the glass surface to be collected, while the emission from the substrate edges was not collected. When calculating the luminance, a Lambertian emission profile was assumed. We have reproduced the measurements multiple times and also for several repetitions of the same experiment. The operating lifetime was measured using fresh pixels in a nitrogen-filled glovebox without encapsulation. The device was driven by a Keithley 2400 source meter at a constant current, and the luminance intensity was measured with a commercial photodiode (Vishay Semiconductors BPW34). The current used to drive the device was first determined using the current density and luminance measurements. The photodiode was biased at 0 V and the photocurrent that proportional to the luminance was recorded at a 2 s interval.

## A.3 Chapter 6 – Semiconductor Discovery Guided via Machine Learning

### Computational Methods

### Data Generation for ML

For predicting stability and optoelectronic properties of the materials, we use DFT calculations to get energy above hull and bandgaps coupled with the direct/indirect nature of the band structure. We trained our modified Graph Neural Networks on total energy data obtained from the Materials Project on over 100,000 compounds and about 10,000 datapoints of direct/indirect bandgaps. The total energy values obtained from the Materials Project are based on Perdew-Burke-Ernzerhof exchange-correlation functional which has been shown to perform satisfactorily for predicting the stability of the compounds[104,127,128]. To train the bandgap regressor, we generated a small HSE06 exchange-correlation functional-based bandgap dataset. Here we performed DFT calculations using a Γ-point sampling of the Brillouin zone on ~1,800 structurally relaxed geometries obtained from the Materials Project. We invoked the flat-band approximation for the bandgap dataset. Datasets are available online as Supplementary Information.

### General Crystal Graph Network Structure.

We used the PyTorch framework and PyTorch-Geometric module to build the crystal graphs and implement the graph convolutional neural network models. The method to encode the crystal structures as graphs is a standard process previously reported in the literature[100–102]. Crystal structures are formatted as undirected graphs $G:= \{V, E\}$ which represent nodes ($n$) as atoms and edges connecting the corresponding atoms as bonds, respectively. Each node and edge can have a corresponding feature vector, which fully describes the 2D planar representation of the crystal structure.

In our network, we encode atomic features denoted $u_i$ (a particular set of physical and chemical features native to the atom at node $i$, refer to Supplementary Information for an exhaustive list) and a new edge feature vector labelled $e_{i,j}$ as the reciprocal distance between the connecting nearest neighbouring atoms $i$ and $j$. Nearest neighbours at each node are selected by implementing a cut-off radius of 8Å, ensuring that only the local environment is considered.

The resulting crystal graph allows for a convolutional neural network to be built on top. The general idea of a graph convolutional neural network is to take a graph as input; perform a particular convolution operation (consisting of a message and update step) based on the nodal and edge-based feature vectors, and output a new scalar or vector for each corresponding node and

edge. This convolution operation is repeated *T* iterations, at which point the newly updated features are then pooled together to obtain an aggregated prediction value by a read-out function. At each successive iteration, the nodal features are updated to incorporate long-range order from atoms outside of the initial cut-off radii; learning a feature vector that includes information from the surrounding environment and enabling accurate predictions of material properties inherent to the crystal structure. The convolution operator for an atom feature vector $u_i$, in this case,

$$u_i^{t+1} = Conv\left(u_i^t, u_j^t, e_{ij}\right), \forall\, i,j \in G\,,$$

where the indices *i* and *j* correspond to two atoms connected in graph *G*. The pooling operation to aggregate all of the newly learnt hidden nodal features to predict a value for a given crystal is shown below and is typically defined by a function such as the mean, maximum or sum:

$$\hat{y} = Pool(u^T)\,, \forall\, u \in G$$

All code and models are available online as Supplementary Information.

**Predictive Graph-based Convolutional Neural Network Models.**

***Bandgap Models***

Many studies have implemented various convolutional operators with success[100,101,103,104], but here we use a complimentary set of convolutional graph neural networks as the basis for our predictive ML models. We design a specific convolution operation for the bandgap regressor shown below. Each crystal graph is fed into the network as an input; wherein the convolutional layer is defined by the following order of operations: the maximum vector after concatenation ($\oplus$) of the current atoms feature vector ($u_i^t$), the product of each neighbouring ($\mathcal{N}(i)$) atomic feature vectors ($u_j^t$) with the corresponding edge features ($e_{ij}$) at each iteration $t$. The $\gamma^t$ represents the update function (typically defined by a multilayer perceptron (MLP) consisting of a non-linear activation function $g$) and weight tensors $W_s^t$ and $b^t$ which are learnt during the training steps for each convolutional layer.

$$u_i^{t+1} = \gamma^t\left[\max_{j\in\mathcal{N}(i)}\left(u_i^t \oplus \left(u_j^t \cdot e_{ij}\right)\right)\right], \qquad \begin{matrix}\forall\, i,j \in G \\ \forall\, t \in \{1,\dots,T\}\end{matrix}$$

$$u_i^{t+1} = g\left[\max_{j\in\mathcal{N}(i)}\left(u_i^t \oplus \left(u_j^t \cdot e_{ij}\right)\right) W_s^t + b^t\right], \begin{matrix}\forall\, i,j \in G \\ \forall\, t \in \{1,\dots,T\}\end{matrix}$$

An output value is obtained by pooling all of the hidden nodal features using the mean pooling function which results in the prediction of a bandgap value $\hat{y}_{bandgap}$.

$$\hat{y}_{bandgap} = \frac{1}{n}\sum_{i=1}^{n} u_i^T, \qquad \forall\, u \in G$$

To measure the accuracy of the ML models, we use the mean squared error as a cost/loss function. We seek to minimize the MSE during training which evaluates how well our predicted bandgap is with respect to the target values. We achieve this minimization by finding the optimal values for the weight and bias matrices in the corresponding convolutional layers.

$$MSE = \frac{1}{n}\sum_{i=1}^{n} (y_i - \hat{y_i})^2, \qquad \forall\, i \in G$$

We observed that a total of 4 convolutional layers and 2 fully connected dense layers were the most optimal choice of the network that led to accurate predictions of the bandgaps. The list of atomic features (Appendix B.3 Tables 1 and 2) and the best performing set are reported in the Supplementary Information. All features were normalized via standard ML procedures prior to the crystal graph generation to ensure comparable scalar magnitudes. Graphs were generated using the aforementioned process, enabling efficient and rapid batch training. Hyperparameters of the model were optimized which include: the size of each convolutional layer, choice of activation function, pooling layer, learning rate and weight decay. After hyperparameter optimization, we found the following parameters: Adam optimizer, a rectifying linear unit activation function, learning rate of 0.01, weight-decay of 0.0005, 4 convolutional layers (consisting of 64, 64, 32, 16 output channels) resulted in a mean-absolute-error of 0.46 eV on validation data after 3000 epochs of training on a set of roughly 1,800 crystals. The best model was chosen and used as one of the surrogate models for the evolutionary algorithmic approach.

***Energy Models***

Using the same convolution expressions as the bandgap model, 4 convolutional layers with batch normalization and 2 fully connected dense layers were the best network that led to accurate predictions of the energy above hull. After hyperparameter optimization that the following parameters: Adam optimizer, a rectifying linear unit activation function, learning rate of 0.0001, 4 convolutional layers (consisting of 64, 64, 64, 64 output channels) resulted in a mean-absolute-error of 0.06 eV/atom on validation data after 2000 epochs of training on a set of roughly 100,000 crystals (refer to SI for loss curves).

***Direct-Indirect classification***

For the direct-indirect bandgap classification, we use a random forest classifier trained on global features generated using elemental compositions and Spacegroup information.

Using statistical properties of elemental properties such as electronegativity and atomic mass, we generate a global representation using Matminer. TPOT was then employed to find the best hyper-parameters. The resulting ML pipeline achieved an $F_1$-score of 0.8 on direct-indirect classification. (refer to SI table 3 for the list of the properties used, and SI note 4 for ML model parameters)

**Evolutionary Algorithm.**

The EA operates on a surrogate model composed of the three predictive ML models built for the various prediction and classification tasks. A selection criterion is designed for target material properties such as the bandgap value and stability. In general, the multi-step iterative process by which the evolutionary search is implemented is as follows: (1) initialization of primary candidates denoted as the initial generation; (2) prediction of material properties using the ML models; (3) evaluation of the current generation; (4) selection of the fittest candidates; and (5) mutations in the selected individuals, and developing a new generation of candidates. Over successive iterations, the evolutionary algorithm converges and outputs a set of candidates that are optimal given the current set of selection parameters. *Initialization*: In the initialization step, we select a set of elements and generate an initial set of candidates based on the 200 crystal structure types and 7 families. We select the bandgap and energy above hull which we would like to optimize for and set these search criteria. *Prediction*: Crystal graphs are generated via the aforementioned process and fed as inputs into the three pre-trained ML models to obtain prediction values for the bandgap, energy above hull, and direct-indirect classification. *Evaluation:* We evaluate each individual in the current generation given the loss metric as shown in the equation below which is a weighted sum of the squared loss for each individually predicted property and the target selection values, where $\lambda_i$ are normalizing factors for each loss component. For the selection procedures, we set all the weights to be equal. We initialize with a population of 20 arbitrarily formed prototype structures, set the generations limit threshold at 200. *Selection*: Upon evaluating the loss, we rank all individuals by their loss in the current generation and discard the bottom-half and retain the remaining population. *Mutation*: We then proceed to make a mutation on each top-ranked individual in the population which we define as a single elemental substitution in the crystal

structure with the equivalent oxidation state to retain structural charge-neutrality. The new set of candidates is then added to the current top-ranked generating a new population and the process is repeated but now starting at evaluation. After multiple iterations the loss has plateaued, the EA proposes a set of candidate solutions that ideally match the initial selection criteria. The proposed crystal structures are then aggregated and collected to comprise of the candidate solutions for the given target conditions. This process is repeated (100 times in our experiments) for various selection criteria to span the varied bandgap range and design a set of candidate solutions for further analysis and experimental realization.

$$\mathcal{L} = \lambda_1\left(\hat{E}_{gap} - E_{gap}^{target}\right)^2 + \lambda_2\left(\hat{E}_{hull} - E_{hull}^{target}\right)^2 + \lambda_3\left(\hat{E}_{direct} - 1\right)^2$$

**Experimental Synthesis – Film Fabrication.**

Potassium halide (KX, X = I, Br, Cl), copper halide (CuX, X = I, Br, Cl), dimethylsulfoxide (DMSO) and dimethylformamide (DMF) were purchased from Sigma-Aldrich. Chloroform was purchased from DriSolv. All chemicals were used as received. The precursor solution was prepared by dissolving stoichiometric quantities of KX and CuX in a DMSO/DMF (25/75 % v/v) solution (0.5 M) under continuous stirring for 1 h at room temperature. The concentration of the chloride-based precursor solution (in DMSO/DMF 75/25 % v/v) was limited to 0.2 M due to the low-solubility of the precursors. Glass substrates were $O_2$ plasma-treated to improve adhesion. The precursor solution was spin-coated onto the substrates via a two-step process: 1000 rpm for 10 s and 3000 rpm. for 60 s. During the second spin step, 0.5 mL of chloroform was poured onto the substrate. The films were then annealed at 110 °C for 10 min. All the samples were prepared in a glove box with $N_2$ atmosphere in order to control the atmospheric conditions.

**Material characterization.**

X-ray diffractograms were recorded using a Rigaku MiniFlex 600 powder X-ray diffractometer equipped with a NaI scintillation counter and using monochromatized Cu Kα radiation (l=1.5406A˚). UV−Vis absorption was measured using a Perkin Elmer LAMBDA 950 UV/Vis/NIR spectrometer. PL measurements were collected using a UV-Vis USB 2000+ spectrometer (Ocean Optics). The samples were optically excited using a 355 nm frequency-tripled Nd:YAG laser with a pulse width of 2 ns and a repetition rate of 100 Hz

## B. Figures

### B.1 Chapter 4 – Enabling Deep-Blue Emission in Perovskite Quantum Dots

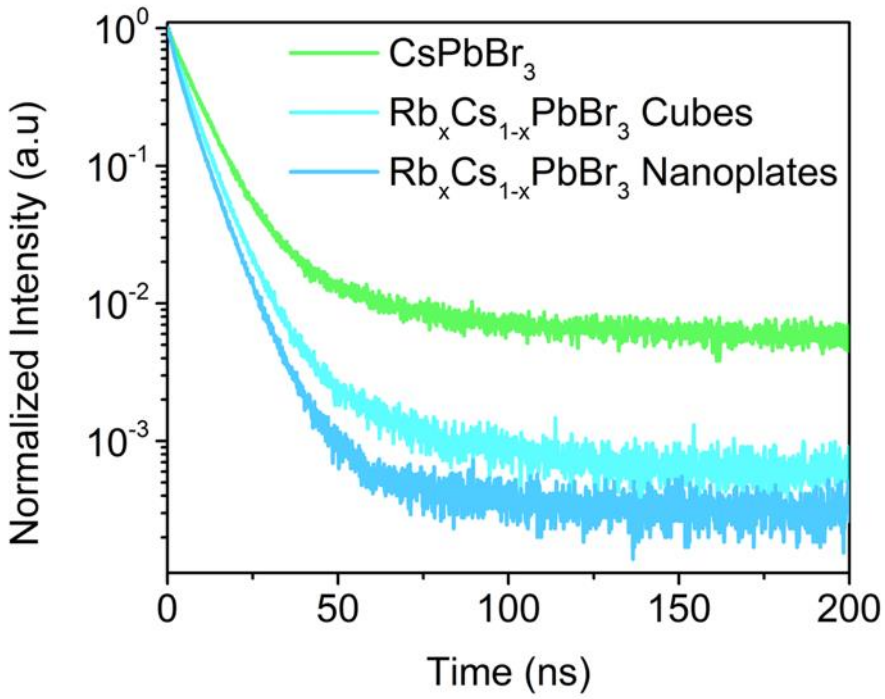


**Figure 1.** Time-resolved photoluminescence decay data of the synthesized PQDs dispersed in hexane. Control $CsPbBr_3$ was used as a reference to compare our doping strategy.

**Table 1.** Transient photoluminescence fits of radiative lifetime components of the synthesized solutions ($Rb_xCs_{1-x}PbBr_3$ cubes (150 °C) and nanoplates (120 °C)). A biexponential decay function was used to fit the photoluminescence decay.

| Solution | Temperature [°C] | $A_1$ | $\tau_1$ [ns] | $A_2$ | $\tau_2$ [ns] | $\tau_{average}$ [ns] |
|---|---|---|---|---|---|---|
| $CsPbBr_3$ | 150 | 0.865 | 7.031 | 0.0813 | 19.209 | 9.517 |
| $Rb_xCs_{1-x}PbBr_3$ | 135 | 0.863 | 5.472 | 0.0802 | 12.628 | 6.735 |
| $Rb_xCs_{1-x}PbBr_3$ | 120 | 0.371 | 2.351 | 0.6577 | 6.2971 | 5.610 |

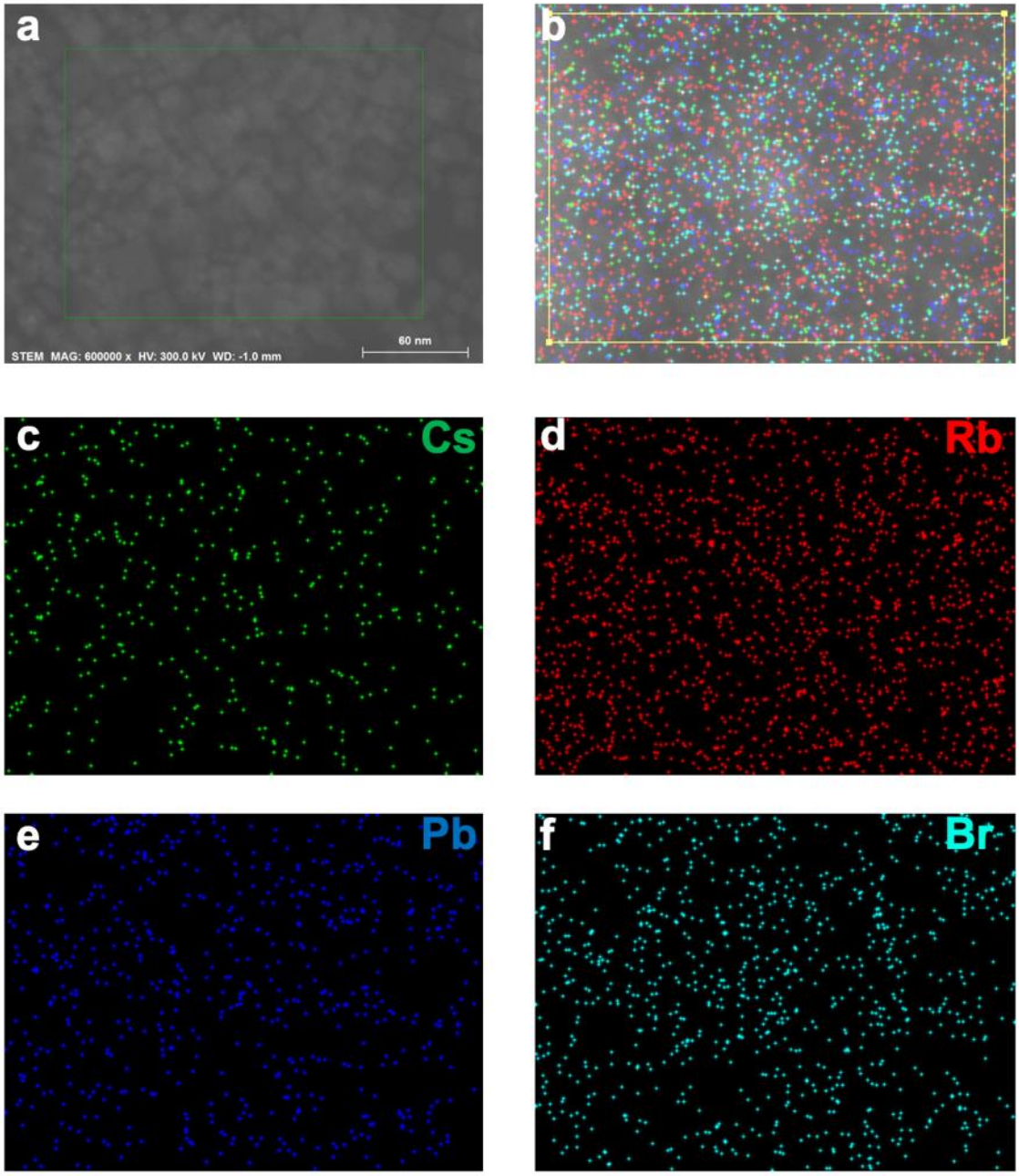


**Figure 2.** STEM micrograph images (a) of sky-blue emitting perovskite quantum dots. EDX overlay spectra (b) and individual atomic mapping of PQDs indicating the presence of Cs, Rb, Pb and Br (c-f).

## B.2 Chapter 5 – Improving Spectral Stability in Perovskite LEDs

**Table 1.** Transition barriers for hydrolysis reaction involving organic chlorides calculated using NEB DFT.

| Organic Chloride | Hydrolysis Reaction | Reaction Energy (eV) | Kinetic Barrier (eV) |
|---|---|---|---|
| DPPOCl | $DPPOCl + H_2O \rightarrow DPPOOH + HCl$ | -0.56 | 1.52 |
| $PPOCl_2$ | $PPOCl_2 + 2H_2O \rightarrow PPO(OH)_2 + 2HCl$ | -0.35 | 1.43 |
| $PSO_2Cl$ | $PSO_2Cl + H_2O \rightarrow PSO_2OH + HCl$ | -0.04 | 5.41 |
| PCOCl | $PCOCl + H_2O \rightarrow PCOOH + HCl$ | -0.34 | 3.95 |

Note: The negative value of the reaction energy shows that the final hydroxide state is more stable and the hydrolysis reaction is favorable, however, the reaction may be still limited by the high kinetic barrier. For each hydrolysis reaction, two possible pathways were evaluated, the proton ($H^+$) in $H_2O$ first attacking the chlorine or oxygen, and only the lowest barrier is reported here. These results show that DPPOCl and $PPOCl_2$ react with $H_2O$ to release $Cl^-$.

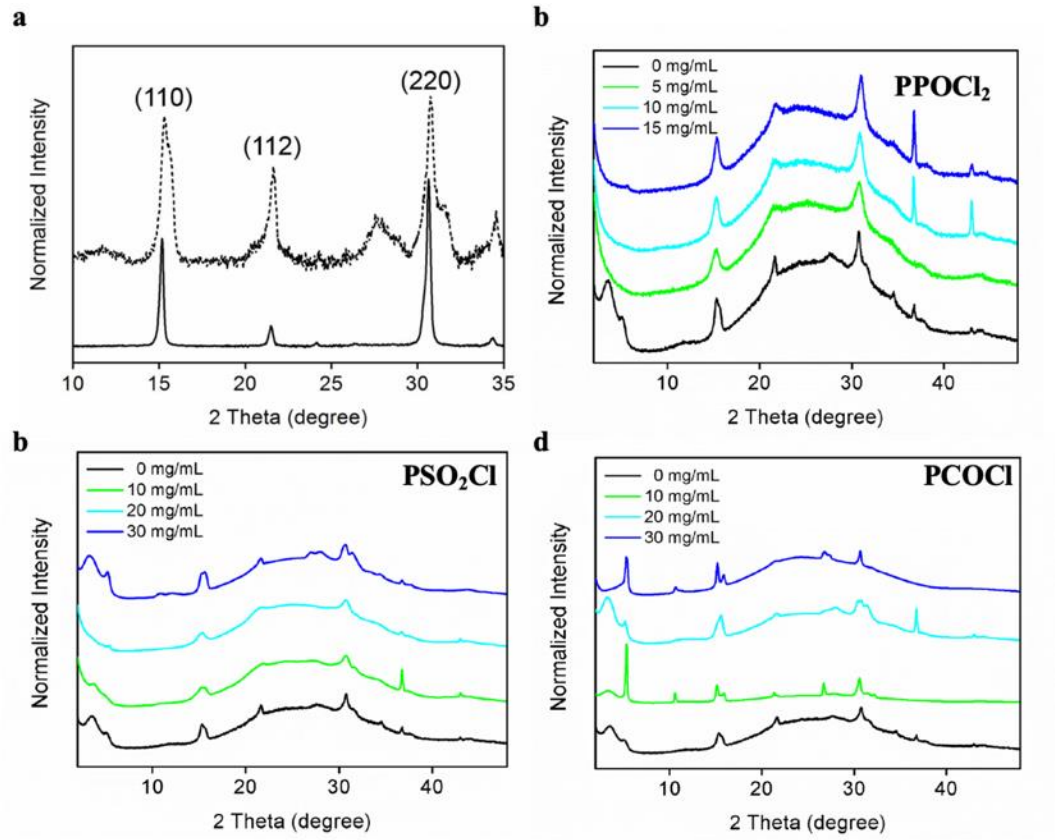


**Figure 1**. XRD Profiles of the various organophosphoryl chlorides in the reduced dimensional perovskite film.

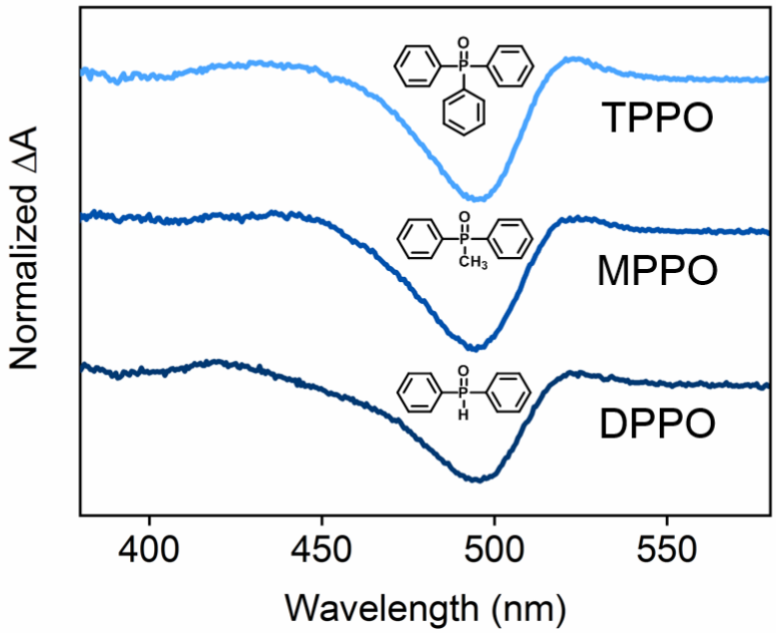


**Figure 2.** TA spectra of perovskites $PEA_2Cs_{1.6}MA_{0.4}Pb_3Br_{10}$ treated with 10 mg/mL DPPO, MPPO, or TPPO (measured at 10 ps).

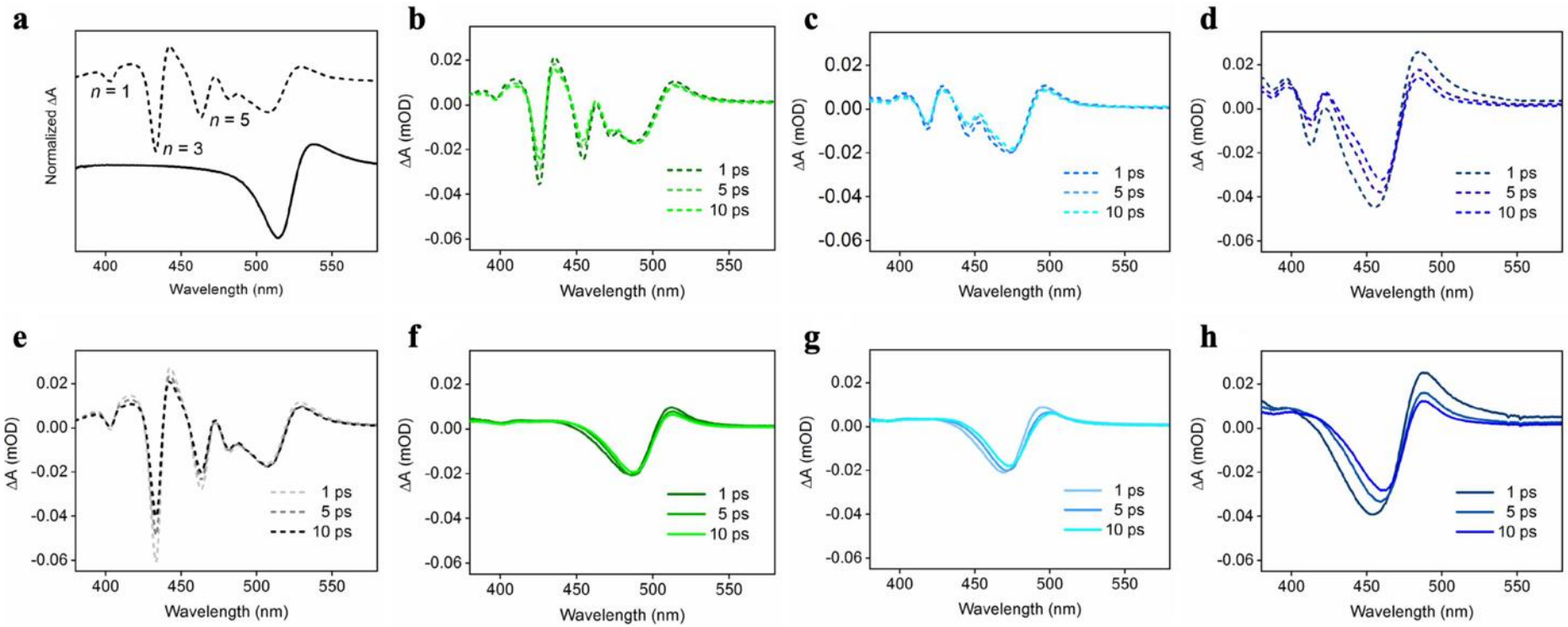


**Figure 3.** TA spectra of control $PEA_2Cs_{1.6}MA_{0.4}Pb_3Br_7Cl_3$ (x = 3, dash line in a) and perovskites $PEA_2Cs_{1.6}MA_{0.4}Pb_3Br_{10}$ treated with 30 mg/mL DPPOCl (solid line in b) reported at 1, 5, and 10 ps delay following photoexcitation pulse.

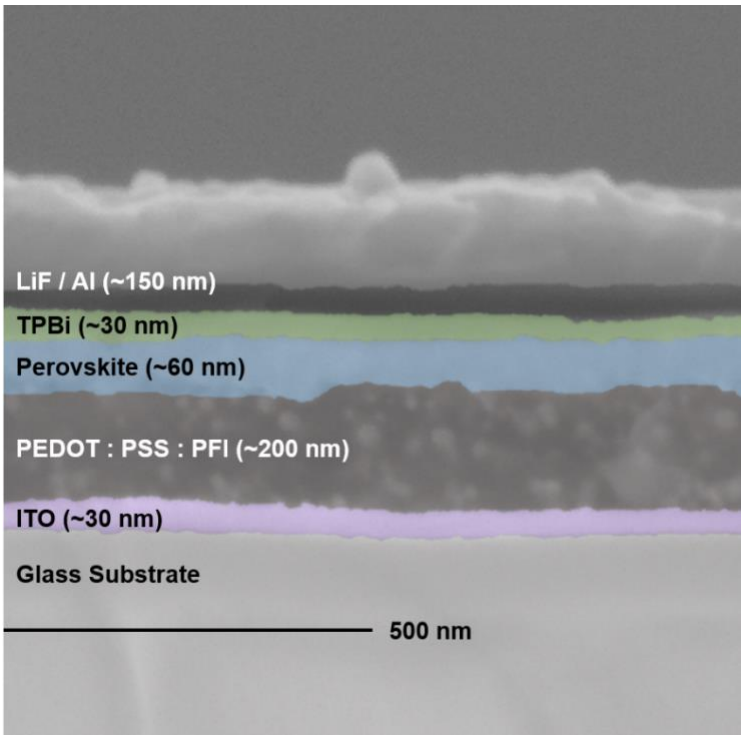


**Figure 4.** Cross-sectional SEM image of LEDs with a structure of ITO/ PEDOT: PSS: PFI (~200 nm)/ Perovskite (~60 nm)/ TPBi (~30 nm)/ LiF/ Al (~150 nm).

## B.3 Chapter 6 – Semiconductor Discovery Guided via Machine Learning

Table 1: List of 63 atomic features used in the bandgap regression models.

| List of 63 Atomic Features | | |
|---|---|---|
| AllenElectronegativity | AtomicRadius | AtomicWeight |
| BoilingT | BulkModulus | Column |
| CovalentRadius | Density | DipolePolarizability |
| ElectronAffinity | Electronegativity | FirstIonizationEnergy |
| FusionEnthalpy | GSbandgap | GSenergy_pa |
| GSestBCClatcnt | GSestFCClatcnt | GSmagmom |
| GSvolume_pa | HHIp | HHIr |
| HeatCapacityMass | HeatCapacityMolar | HeatFusion |
| HeatVaporization | ICSDVolume | IonizationEnergies |
| IsAlkali | IsDBlock | IsFBlock |
| IsMetal | IsMetalloid | IsNonmetal |
| LogThermalConductivity | MeltingT | MendeleevNumber |
| MiracleRadius | MolarVolume | NUnfilled |
| NValence | NdUnfilled | NdValence |
| NfUnfilled | NfValence | NpUnfilled |
| NpValence | NsUnfilled | NsValence |
| Number | Polarizability | Row |
| SecondIonizationEnergy | ShearModulus | SpaceGroupNumber |
| ThermalConductivity | VdWRadius | ZungerPP-r_d |
| ZungerPP-r_p | ZungerPP-r_pi | ZungerPP-r_s |
| ZungerPP-r_sigma | n_wsˆthird | phi |

Table 2: List of 33 atomic features used in the bandgap regression models.

| List of 33 Atomic Features | | |
|---|---|---|
| AllenElectronegativity | AtomicRadius | AtomicWeight |
| BoilingT | BulkModulus | CovalentRadius |
| Density | DipolePolarizability | ElectronAffinity |
| Electronegativity | FirstIonizationEnergy | FusionEnthalpy |
| HeatCapacityMass | HeatCapacityMolar | HeatFusion |
| HeatVaporization | LogThermalConductivity | MeltingT |
| NValence | NdUnfilled | NdValence |
| NfUnfilled | NfValence | NpUnfilled |
| NpValence | NsUnfilled | NsValence |
| Polarizability | SecondIonizationEnergy | ShearModulus |
| ThermalConductivity | VdWRadius | phi |

**Tables 1 & 2 | Data: Atomic features lists.**

Lists of the atomic features used in the regression models. Prior to regression all of the features were scaled in the particular graphs dataset to a [0,1] scale by the minimum-maximum method ($x_{scaled} = (x_{old} - x_{min})/(x_{max} - x_{min})$).

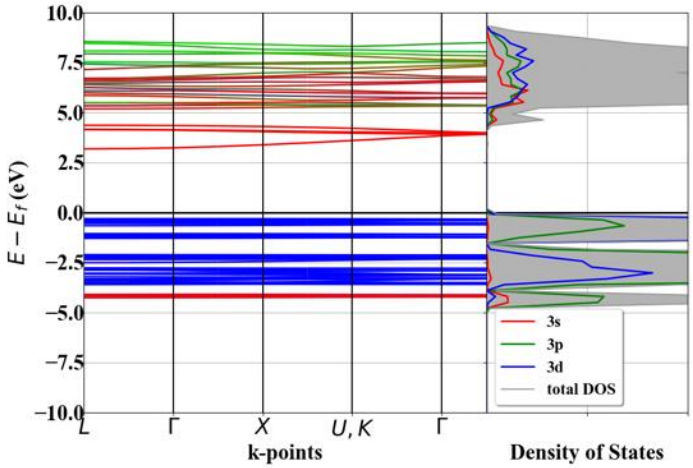


**Figure 1:** Band structure and Density of States (DOS) for $K_2CuBr_3$.

Using HSE06 exchange-correlation functional, we perform DFT calculations for calculation of band structure and density of states for $K_2CuBr_3$.

## C. Copyright and Permissions

Print

JOHN WILEY AND SONS LICENSE
TERMS AND CONDITIONS

Feb 09, 2021

This Agreement between Mr. Petar Todorovic ("You") and John Wiley and Sons ("John Wiley and Sons") consists of your license details and the terms and conditions provided by John Wiley and Sons and Copyright Clearance Center.

| | |
|---|---|
| License Number | 5004930912624 |
| License date | Feb 09, 2021 |
| Licensed Content Publisher | John Wiley and Sons |
| Licensed Content Publication | Advanced Optical Materials |
| Licensed Content Title | Spectrally Tunable and Stable Electroluminescence Enabled by Rubidium Doping of CsPbBr3 Nanocrystals |
| Licensed Content Author | Edward H. Sargent, Zheng-Hong Lu, Yitong Dong, et al |
| Licensed Content Date | Sep 20, 2019 |
| Licensed Content Volume | 7 |
| Licensed Content Issue | 24 |
| Licensed Content Pages | 7 |
| Type of Use | Dissertation/Thesis |
| Requestor type | Author of this Wiley article |
| Format | Print and electronic |
| Portion | Full article |
| Will you be translating? | No |
| Title | Spectrally Tunable and Stable Electroluminescence Enabled by Rubidium Doping of CsPbBr3 Nanocrystals |
| Institution name | University of Toronto |
| Expected presentation date | Apr 2021 |

1/18/2021 Rightslink® by Copyright Clearance Center

Copyright Clearance Center RightsLink® Home Help Email Support Petar Todorovic

ACS Publications
Most Trusted. Most Cited. Most Read.

**Chloride Insertion–Immobilization Enables Bright, Narrowband, and Stable Blue-Emitting Perovskite Diodes**

**Author:** Dongxin Ma, Petar Todorović, Shadi Meshkat, et al
**Publication:** Journal of the American Chemical Society
**Publisher:** American Chemical Society
**Date:** Mar 1, 2020

*Copyright © 2020, American Chemical Society*

PERMISSION/LICENSE IS GRANTED FOR YOUR ORDER AT NO CHARGE

This type of permission/license, instead of the standard Terms & Conditions, is sent to you because no fee is being charged for your order. Please note the following:

- Permission is granted for your request in both print and electronic formats, and translations.
- If figures and/or tables were requested, they may be adapted or used in part.
- Please print this page for your records and send a copy of it to your publisher/graduate school.
- Appropriate credit for the requested material should be given as follows: "Reprinted (adapted) with permission from (COMPLETE REFERENCE CITATION). Copyright (YEAR) American Chemical Society." Insert appropriate information in place of the capitalized words.
- One-time permission is granted only for the use specified in your request. No additional uses are granted (such as derivative works or other editions). For any other uses, please submit a new request.

BACK CLOSE WINDOW

Copyright Clearance Center | RightsLink®

Home | Help | Email Support | Petar Todorovic

ACS Publications
Most Trusted. Most Cited. Most Read.

**Searching for "Defect-Tolerant" Photovoltaic Materials: Combined Theoretical and Experimental Screening**

**Author:** Riley E. Brandt, Jeremy R. Poindexter, Prashun Gorai, et al
**Publication:** Chemistry of Materials
**Publisher:** American Chemical Society
**Date:** Jun 1, 2017

*Copyright © 2017, American Chemical Society*

**PERMISSION/LICENSE IS GRANTED FOR YOUR ORDER AT NO CHARGE**

This type of permission/license, instead of the standard Terms & Conditions, is sent to you because no fee is being charged for your order. Please note the following:

- Permission is granted for your request in both print and electronic formats, and translations.
- If figures and/or tables were requested, they may be adapted or used in part.
- Please print this page for your records and send a copy of it to your publisher/graduate school.
- Appropriate credit for the requested material should be given as follows: "Reprinted (adapted) with permission from (COMPLETE REFERENCE CITATION). Copyright (YEAR) American Chemical Society." Insert appropriate information in place of the capitalized words.
- One-time permission is granted only for the use specified in your request. No additional uses are granted (such as derivative works or other editions). For any other uses, please submit a new request.

If credit is given to another source for the material you requested, permission must be obtained from that source.

BACK | CLOSE WINDOW

Copyright Clearance Center | RightsLink®

Home | Help | Email Support | Petar Todorovic

ACS Publications
Most Trusted. Most Cited. Most Read.

**Two-Dimensional Hybrid Halide Perovskites: Principles and Promises**

**Author:** Lingling Mao, Constantinos C. Stoumpos, Mercouri G. Kanatzidis
**Publication:** Journal of the American Chemical Society
**Publisher:** American Chemical Society
**Date:** Jan 1, 2019

*Copyright © 2019, American Chemical Society*

**PERMISSION/LICENSE IS GRANTED FOR YOUR ORDER AT NO CHARGE**

This type of permission/license, instead of the standard Terms & Conditions, is sent to you because no fee is being charged for your order. Please note the following:

- Permission is granted for your request in both print and electronic formats, and translations.
- If figures and/or tables were requested, they may be adapted or used in part.
- Please print this page for your records and send a copy of it to your publisher/graduate school.
- Appropriate credit for the requested material should be given as follows: "Reprinted (adapted) with permission from (COMPLETE REFERENCE CITATION). Copyright (YEAR) American Chemical Society." Insert appropriate information in place of the capitalized words.
- One-time permission is granted only for the use specified in your request. No additional uses are granted (such as derivative works or other editions). For any other uses, please submit a new request.

If credit is given to another source for the material you requested, permission must be obtained from that source.

BACK | CLOSE WINDOW

Copyright Clearance Center | Marketplace™

## Royal Society of Chemistry - License Terms and Conditions

This is a License Agreement between Petar Todorovic ("You") and Royal Society of Chemistry ("Publisher") provided by Copyright Clearance Center ("CCC"). The license consists of your order details, the terms and conditions provided by Royal Society of Chemistry, and the CCC terms and conditions.

All payments must be made in full to CCC.

| | | | |
|---|---|---|---|
| **Order Date** | 03-Feb-2021 | **Type of Use** | Republish in a thesis/dissertation |
| **Order license ID** | 1095303-1 | **Publisher** | RSC Pub |
| **ISSN** | 2040-3372 | **Portion** | Chart/graph/table/figure |

### LICENSED CONTENT

| | | | |
|---|---|---|---|
| **Publication Title** | Nanoscale | **Country** | United Kingdom of Great Britain and Northern Ireland |
| **Author/Editor** | National Center for Nanoscience and Technology., Royal Society of Chemistry (Great Britain) | **Rightsholder** | Royal Society of Chemistry |
| | | **Publication Type** | e-Journal |
| **Date** | 01/01/2009 | **URL** | http://www.rsc.org/Publishing/Journals/N... |
| **Language** | English | | |

### REQUEST DETAILS

| | | | |
|---|---|---|---|
| **Portion Type** | Chart/graph/table/figure | **Distribution** | Canada |
| **Number of charts / graphs / tables / figures requested** | 2 | **Translation** | Original language of publication |
| | | **Copies for the disabled?** | No |
| **Format (select all that apply)** | Print, Electronic | **Minor editing privileges?** | No |
| **Who will republish the content?** | Not-for-profit entity | **Incidental promotional use?** | No |
| **Duration of Use** | Life of current edition | **Currency** | CAD |
| **Lifetime Unit Quantity** | Up to 499 | | |
| **Rights Requested** | Main product | | |

### NEW WORK DETAILS

| | | | |
|---|---|---|---|
| **Title** | The Design of Perovskites for Light-Emitting Applications | **Institution name** | University of Toronto |
| | | **Expected presentation date** | 2021-04-30 |
| **Instructor name** | Petar Todorovic | | |

### ADDITIONAL DETAILS